UNIVERSITY OF CALIFORNIA, SAN DIEGO

Particle transport as a result of Resonant Magnetic Perturbations

A dissertation submitted in partial satisfaction of the
requirements for the degree
Doctor of Philosophy

in

Engineering Sciences (Engineering Physics)

by

Saskia Mordijck

Committee in charge:

Richard A. Moyer, Chair
Farhat Beg
Patrick H. Diamond
Farrokh Najmabadi
George Tynan

2011

The dissertation of Saskia Mordijck is approved, and it is acceptable in quality and form for publication on microfilm and electronically:

Chair

University of California, San Diego

2011

DEDICATION

To Pieter

EPIGRAPH

A person who never made a mistake never tried anything new.
—Alber Einstein

TABLE OF CONTENTS

LIST OF FIGURES

LIST OF TABLES

ACKNOWLEDGEMENTS

Most probably if you are reading this, you either know me, or you are just an extremely curious person. If you know me, you probably want to know if I was smart enough to remember you. So if your name does not appear in this little section, please remember this is the most difficult part in writing the whole dissertation. There is always going to be this one person that really deserves to be mentioned, but because one is under such stress in just getting everything done and finished, unfortunately, this person is forgotten. So this is for you too.

But let's get back to thanking all those people, who's names I did not forget. First of all, I really need to thank Rick Moyer, my adviser. Rick, you probably had no clue what you were getting into when I first showed up at your office. I hope that your experience was as pleasant as mine; you were a really good mentor and I did learn a lot. Thanks to you, I have broadened my research horizon, have learned to be a little more wordy (but only a little :)) and you showed me to appreciate the complexity of experiments. Thank you for the nice journey and I hope that our paths will continue crossing in the future.

I would also like to thank my committee members. Thank you for your patience and input to this work. More in particular I would like to thank Pat Diamond. I would like to thank him for seeing the potential in me and trying very hard to nurture it. Although you know I am not much of a pen and paper plasma physics theorist, you kept pushing for me to first understand the basics before I jumped head over heels into writing a little script to do the calculation for me. I hope you never give up on me, because your vast knowledge and willingness to tutor young people is something I will always cherish (just as your sharp wit). Then I also need to says thanks to Andrew Kirk. You have been instrumental in the work I did on MAST. Whenever I had a question or problem you created time in your schedule that was overloaded to begin with. I hope I will be able to return the favor sometime in the future. I would also like to thank Todd Evans for helping set my first steps into the chaotic world of RMPs. Also a special thanks to Tine Baelmans and Detlev Reiter for introducing me to the fascinating world of fusion.

Then there is the typical group of people you quite often find as a last author to some of the experimental papers: The DIII-D Team. It is never quite clear who we mean by that. I think every person in the DIII-D Team was essential to make this work possible. But again, like always a few come to mind to whom I am deeply indebted. Chuck, you make DIII-D one of the best places to be as a student. Ed, Nicholas, not only do I consider you good friends, you were there to help with my experiment, while you should have been home with your friends and family by that time. Francesca, thank you for laughing at my bad jokes. There are so many people I was fortunate to meet at DIII-D, Tom (more than one), Zeke, Mathias, Sean, Ted, Ruth, David, Anne, Tim, Larry, Novi, Matt, Morgan, and the lunch crew. Then there is Michelle, who started out as my roommate, but became my best friend. I can not count all the evenings we spend sitting on the floor outside our rooms (I have no clue why we did not pick the more comfortable sofa), while we commiserated about our lives as graduate students and all the work we still needed to do and how it looks like it will never end. Well, Michelle, at one point it does, so hang in there, you are nearly there and you will do great.

I am grateful for the permanent faith my parents had in me. Although, they have often wished it was different, it was their persistence in making me finish what I started that made me the stubborn person I am today. Without that stubbornness, I would have never made it this far.

Finally, I would like to tell Pieter how grateful I am for him being who he is. Not only are you the best husband any wife could wish for, but you are a role model to me. I look up to you every day for everything you have accomplished. Thank you for putting up with my grumpiness, especially while I was trying to write this dissertation.

VITA

2006	MS. in Mechanical Engineering, Katholieke Universiteit Leuven, Leuven, Belgium
2007-2010	Graduate Student Researcher, Center of Energy Research, University of California, San Diego
2007	Graduate Teaching Assistant, University of California, San Diego
2010	MS. in Mechanical Engineering, University of California, San Diego
2011	Ph. D. in Mechanical Engineering, University of California, San Diego

PUBLICATIONS

S. Mordijck, R.A. Moyer, A. Kirk, P. Tamain, D. Temple, G.R. McKee, E. Nardon “Comparison of resonant magnetic perturbation induced particle transport changes on DIII-D and MAST” *Journal of Nuclear Materials (Plasma Surface Interactions 2010)*, **submitted**.

A. Kirk, E. Nardon, P. Tamain, P. Denner, H. Meyer, **S. Mordijck**, D. Temple and the MAST team “The effect of resonant magnetic perturbations on L and H-mode plasmas on MAST” *Journal of Nuclear Materials (Plasma Surface Interactions 2010)*, **submitted**.

T.W. Petrie, T.E. Evans, M.E. Fenstermacher, **S. Mordijck**, N.H. Brooks, J.R. Ferron, B. Hudson, A.W. Hyatt, C.J. Lasnier, A.W. Leonard, T.C. Luce, R.A. Moyer, P.A. Politzer, M.J. Schaffer, P.B. Snyder, J.G. Watkins “First results examining the compatiblity of RMP ELM suppression with the radiating divertor in DIII-D” *Journal of Nuclear Materials (Plasma Surface Interactions 2010)*, **submitted**.

T.W. Petrie, T.E. Evans, N.H. Brooks, M.E. Fenstermacher, J.R. Ferron, B. Hudson, A.W. Hyatt, T.C. Luce, C.J. Lasnier, **S. Mordijck**, P.A. Politzer, M.E. Rensink, M.J. Schaffer, P.B. Snyder, J.G. Watkins “Results from Radiating Divertor Experiments with RMP ELM Suppression” *Conference proceeding of 23nd IAEA Fusion Energy Conference 2010.*

O. Schmitz, T.E. Evans, M.E. Fenstermacher, H. Stoschus, E.A. Unterberg, J.W. Coenen, H. Frerichs, M.W. Jakubowski, R. Laengner, C.J. Lasnier, **S. Mordijck**, R.A. Moyer, T.H. Osborne, H. Reimerdes, D. Reiter, U. Samm, B. Unterberg and the DIII-D and TEXTOR teams “Key results from the DIII-D/TEXTOR Collaboration on the Physics of STochastic Boundaries projected to ELM Control at ITER” *Conference proceeding of 23nd IAEA Fusion Energy Conference 2010.*

A. Kirk, E. Nardon, P. Tamain, P. Denner, Y. Liu, H. Meyer, **S. Mordijck**, D. Temple and the MAST team “Magnetic perturbation experiments on MAST using internal coils” *Conference proceeding of 23nd IAEA Fusion Energy Conference 2010.*

S. Mordijck, L.W. Owen, R.A. Moyer “Increased particle transport due to resonant magnetic perturbations modeled with a vacuum field line tracing code and a 2D fluid code”*Nuclear Fusion*, Volume 50, Article 034006, February 2010.

E.A. Unterberg, O. Schmitz, T.E. Evans, R. Maingi, N.H. Brooks, M.E. Fenstermacher, **S. Mordijck**, R.A. Moyer, D.M. Orlov “The effects of an open and closed divertor on particle exhaust during edge-localized mode suppression by resonant magnetic perturbations in DIII-D” *Nuclear Fusion*, Volume 50, Article 034011, February 2010.

D.M. Orlov, R.A. Moyer, T.E. Evans, **S. Mordijck**, T.H. Osborne, M.E. Fenstermacher, P. Snyder, E.A. Unterberg “ Numerical analysis of effects of normalized plasma pressure on RMP ELM suppression in DIII-D”*Nuclear Fusion*, Volume 50, Article 034010, February 2010.

O. Schmitz, T.E. Evans, M.E. Fenstermacher, E.A. Unterberg, M.E. Austin, B.D. Bray, N.H. Brooks, H. Frerichs, M. Groth, M.W. Jakubowski, C.J. Lasnier, M. Lehnen, A.W. Leonard, **S. Mordijck**, R.A. Moyer, T.H. Osborne, D. Reiter, U. Samm, M.J. Schaffer, B. Unterberg, W.P. West and the DIII-D and TEXTOR Research Team ”Resonant pedestal pressure reduction induced by a thermal transport enhancement due to stochastic magnetic boundary layers in high temperature plasmas” *Physical Review Letters*, Volume 103, Article 165005, October 2009.

M.W. Jakubowski, T.E. Evans, M.E. Fenstermacher, M. Groth, C.J. Lasnier, A.W. Leonard, O. Schmitz, J.G. Watkins, T. Eich, W. Fundamenski, R.A. Moyer, R.C. Wolf, L.B. Baylor, J.A. Boedo, K.H. Burrell, H. Frerichs, J.S. deGrassie, P. Gohil, I. Joseph, **S. Mordijck**, M. Lehnen, C.C. Petty, R.I. Pinsker, D. Reiter, T.L. Rhodes, U. Samm, M.J. Schaffer, P.B. Snyder, H. Stoschus, T. Osborne, B. Unterberg, E. Unterberg and W.P. West ”Overview of the results on divertor heat loads in RMP controlled H-mode plasmas on DIII-D” *Nuclear Fusion*, Volume 49, Article 095013, September 2009.

E.A. Unterberg, T.E. Evans, R. Maingi, N.H. Brooks, M.E. Fenstermacher, **S. Mordijck**, R.A. Moyer “ Demonstration of Particle Exhaust Control During ELM suppresion by Resonant Magnetic Perturabtions in DIII-D" *Nuclear Fusion*, Volume 49, Article 092001, September 2009

S. Mordijck, R.A. Moyer, T.E. Evans, X. Bonnin, J. Canik, D. Coster, M. Groth, R. Maingi, T.H. Osborne, L.W. Owen, T.W. Petrie, D. Reiter, J.G. Watkins, and E.A. Unterberg "Fluid modeling of an ELMing H-mode and a RMP H-mode" *Journal of Nuclear materials 2009 (Plasma surface interactions 2008)*, Volumes 390-391, Pages 299-302, June 2009.

E.A. Unterberg, N.H. Brooks, T.E. Evans, M.E. Fenstermacher, D.L. Hillis, R. Maingi, **S. Mordijck**, R.A. Moyer, T.H. Osborne, T.W. Petrie, J.G. Watkins "Experimental comparison of recycling and pumping changes during resonant magnetic perturbation experiments at low and high triangularity" *Journal of Nuclear materials 2009 (Plasma surface interactions 2008)*, Volumes 390-391, Pages 486-489, June 2009.

T.E. Evans, M.E. Fenstermacher, M. Jakubowski, R.A. Moyer, T.H. Osborne, M.J. Schaffer, O. Schmitz, J.G. Watkins, L. Zeng, L.R. Baylor, J.A. Boedo, K.H. Burrell, J.S. deGrassie, P. Gohil, I. Joseph, C.J. Lasnier, A.W. Leonard, **S. Mordijck**, C.C. Petty, R.I. Pinsker, T.L. Rhodes, J.C. Rost, P.B. Snyder, E. Unterberg W.P. West "Operating Characteristics in DIII-D ELM-Suppressed RMP H-modes with ITER Similar Shapes" *Conference proceeding of 22nd IAEA Fusion Energy Conference 2008.*

O. Schmitz, T.E. Evans, M.E. Fenstermacher, H. Frerichs, M.W. Jakubowski, M.J. Schaffer, A. Wingen, W.P. West, N.H. Brooks, K.H. Burrell, J.S. deGrassie, Y. Feng, K.H. Finken, P. Gohil, M. Groth, I. Joseph, C.J. Lasnier, M. Lehnen, A.W. Leonard, **S. Mordijck**, R.A. Moyer, A. Nicolai, T.H. Osborne, D. Reiter, U. Samm, K.H. Spatschek, H. Stoschus, B. Unterberg, E.A. Unterberg, J.G. Watkins, R. Wolf and the DIII-D and TEXTOR Teams "Aspects of three dimensional transport for ELM control experiments in ITER-similar shape plasmas at low collisionality in DIII-D" *Plasma Physics and Controlled Fusion*, Volume 50, Article 124029, 2008.

ABSTRACT OF THE DISSERTATION

Particle transport as a result of Resonant Magnetic Perturbations

by

Saskia Mordijck

Doctor of Philosophy in Engineering Sciences (Engineering Physics)

University of California, San Diego, 2011

Richard A. Moyer, Chair

This thesis makes contributes to field of plasma physics with a particular focus on particle transport as a result of resonant magnetic perturbations (RPMs) in magnetic confinement devices (Tokamaks). RPMs have proven to be a useful technique to suppress edge localized modes (ELMs) that under certain conditions can damage the confinement device. In order to suppress ELMs, these magnetic perturbations are created to be be resonant at the edge of the plasma (i.e., by selecting an $n = 3$ spectrum and a $q_{95} = 3.6$). However, RMPs lead to a changes in the density profile, not only in the pedestal area, but also deeper in the plasma core, limiting plasma performance. As a first contribution in this thesis we carefully investigate density pump-out, and show that it is the result of a change in particle transport (as opposed to a change in neutral fueling). A second contribution of this work is the introduction of a weighted magnetic diffusion coefficient (D_{OFL}) that allows us to make quantitative comparisons between experimental datasets from different Tokamak devices. By comparing D_{OFL} for MAST L-modes and DIII-D H-modes, we find that both machines exhibit a very different density pump-out for similar D_{OFL} values. Since turbulent particle transport is very different for L and H-modes, we investigate, as a third contribution of this work, the influence of RMPs on turbulent particle transport in both MAST and DIII-D. We find that while an increase in turbulent transport on MAST correlates well with density pump-out, no meaningful correlation was found for pedestal density changes in DIII-D. Therefore, as a final contribution in this thesis, we investigate how convective particle transport parallel to the magnetic field alters the density profiles. We compare the increase in convective parallel particle transport and find good agreement with experimental density profiles.

Chapter 1

Introduction

1.1 Motivation

One of the main challenges for this and future generations is the development of sustainable and reliable energy systems. Currently, 77% of our energy production depends on carbon hydrates [3], and produce greenhouse gases. This has led to an increase of 80% in CO_2 concentration in the atmosphere since 1970, which is believed to be the main contributor to global climate change [66].

Another disadvantage of fossil fuel based energy production is that they are a limited resource. Predicting the remaining reserves of fossil fuel correctly is impossible, since it is impossible to predict how many new accessible sources are undiscovered. However, it is estimated that our oil reserves will be depleted within this century [61]. The estimations for natural gas reserves are even more difficult, but currently also point to depletion within this century [5]. This precludes both oil and natural gas as a long term resource for large electricity production plants.

Another well-known solution for large scale electricity production is Nuclear fission. While fissionable materials are also finite, breeding and re-processing can extend the lifetime for this energy source for several centuries [34]. However, the storage of the produced nuclear waste and the safety of power plants and nuclear fuel are under constant discussion [2, 26].

In order to continue meeting the growing demand for electricity consumption, alternative technologies need to be developed that can produce electricity on a large scale. One such alternative technique is nuclear fusion. It has the advantage that it does not result in the emission of greenhouse gases; Nuclear waste is limited and has a short half-life cycle [33]; Supply of the primary fuel is nearly unlimited [33, 60] and it is safe since a run-away reaction is physically impossible.

There are several promising techniques to harness the energy produced by melting atoms together (i.e., fusion) and extracting the produced heat. This thesis focuses on the Magnetic confinement technique utilizing a Tokamak [91].

The goal of a burning plasma, is to generate heat in the core of the plasma with fusion reactions and extract the heat at the wall. Due to the high temperatures needed for fusion, this posses technological as well as physics challenges on the control of plasma-wall interactions [73]. The heat fluxes to walls need to be controlled. Especially impulsive heat loads created by Magneto-Hydrodynamic (MHD) instabilities are a major concern, since they will damage the walls of future tokamak devices like ITER [23, 50].

Edge Localized Modes (ELMs) are such an MHD instability that occurs at the edge of the plasma and transports large short bursts of heat towards the divertor in H-mode plasmas [103]. There are several observed types of ELMs that occur in tokamak plasmas, depending on the equilibrium plasma conditions. Type-I ELMs carry the largest amount of heat and are the result of the plasma edge being peeling-ballooning unstable [35, 10]. The peeling instability is driven by the large bootstrap current at the plasma edge and the ballooning instability is the result of the large pressure gradient in an H-mode. The peeling-ballooning stability limit can be calculated by ideal MHD codes (ex. ELITE [76, 94]) and has been shown to strongly depend on the plasma shape and the bootstrap current [75].

The extrapolated heat loads associated with type-I ELMs will damage the divertor wall and limit operations of ITER as a long pulse device [50]. It is therefore crucial to reduce (by at least factor 20) or eliminated the heat loads associated with type-I ELMs [23, 50]. Several techniques are currently being evaluated: Small ELM regimes [62], pellet pacing [47, 46] and Resonant Magnetic Perturbations (RMP) [20]. RMP is the only technique that has achieved the necessary impulsive heat reduction for ITER [18].

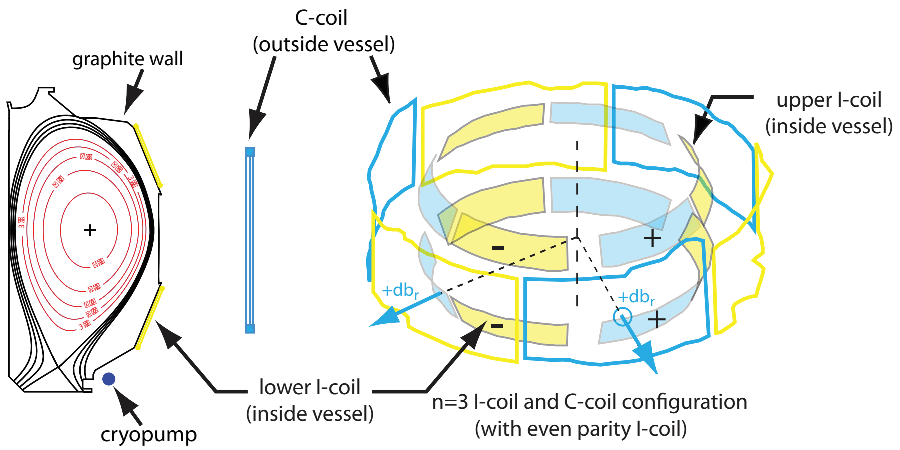

Figure 1.1: Setup of magnetic coil sets on DIII-D

Resonant Magnetic Perturbations (RMPs) for ELM suppression on DIII-D are created by a set of 12 internal coils (see Figure 1.1). There are 2 off-axis rows with each 6 coils that produce radial magnetic perturbations, the so-called I-coils. A 2nd set of external coils, the so-called C-coils are used for error-field control during RMP experiments. For ELM suppression the I-coils generate RMPs with $n = 3$ as main toroidal mode number. There 4 possible configurations:

- Even parity, 0 degree phasing : Upper and lower coil at same toroidal location have the same polarity. The coils located at the toroidal angle of 30 degrees create a magnetic field that is positive radially outward.

- Even parity, 60 degree phasing : Upper and lower coil at same toroidal location have the same polarity. The coils located at the toroidal angle of 30 degrees create a magnetic field that is positive radially inward.

- Odd parity, 0 degree phasing : Upper and lower coil at same toroidal location have the opposite polarity. The upper coil located at the toroidal angle of 30 degrees create a magnetic field that is positive radially outward.

- Even parity, 60 degree phasing : Upper and lower coil at same toroidal location have the opposite polarity. The upper coil located at the toroidal angle of 30 degrees create a magnetic field that is positive radially inward.

Early RMP experiments on DIII-D were performed in the odd parity configuration. These experiments were at high collisionality and had no or little density pump-out. The large type-I ELMs were suppressed, but small grassy burst are still observed in the divertor [20, 58, 8, 21]. ITER, however, is projected to operate at low pedestal collisionality ($\nu^* < 0.1$). We will therefore mostly focus on low collisionality RMP H-mode experiments in DIII-D.

Experiments at low collisionality always show a density pump-out, as shown in Figure 1.2. This density pump-out can be as small as 5% of the pedestal density to 30%. The drop in pedestal density is a contributor in the drop in pedestal pressure [18, 14], see Figure 1.3a. As a result the pressure gradient in the pedestal also drops. This change in the pressure gradient makes the discharge peeling-ballooning stable (Figure 1.3b) and eliminates type-I ELMs [74]. Since the density pump-out is the largest contribution to this drop in pressure gradient, we identify the responsible particle transport channels for this density pump-out. If we understand how RMPs affect particle transport, we can better control and minimize the density pump-out to achieve the plasma performance targets for ITER.

1.2 Overview

To determine whether the changes in the pedestal density are indeed the result of changes in transport, we first examine the influence of changes in neutral fueling on the pedestal structure. In chapter 2, it is shown that changes in recycling and cryo-pumping affect the pedestal density. However, not only is the density at the top of the pedestal altered, the density across the whole pedestal region and the Scrape-Off Layer (SOL) is also affected. As a result, the shape of the density H-mode pedestal is not altered by changes in neutral fueling and therefore only a change in particle transport can explain the changes observed in pedestal shape. This work is also summarized in S. Mordijck et al. [53].

Next, in chapter 3, we introduce the calculation of a weighed diffusion coefficient based on a vacuum field line tracing code, TRIP3D [17]. This weighed

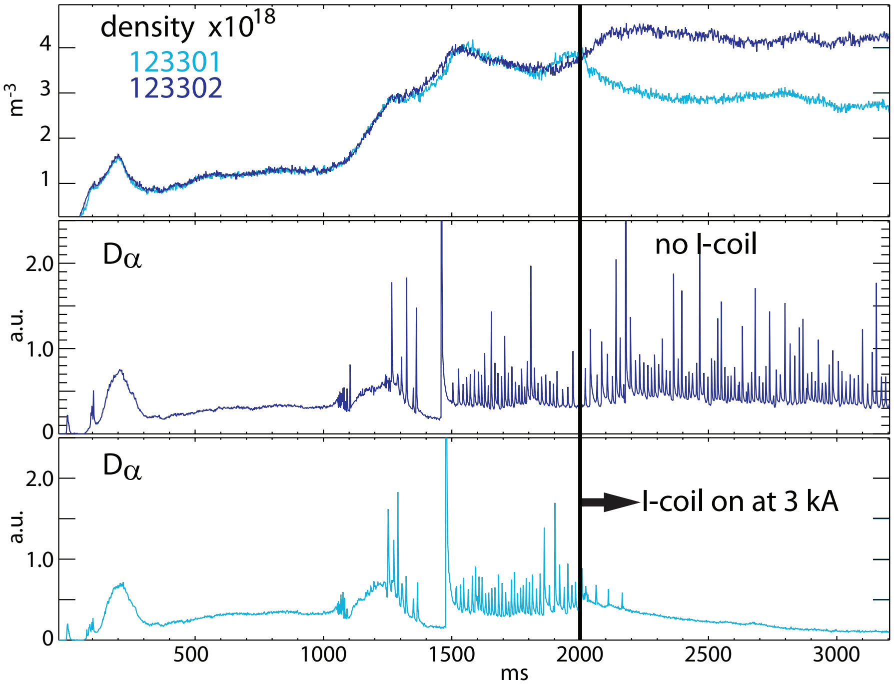

Figure 1.2: Time trace, that shows the suppression of ELMs and the resulting density pump-out after applying $n = 3$ RMPs with the I-coils.

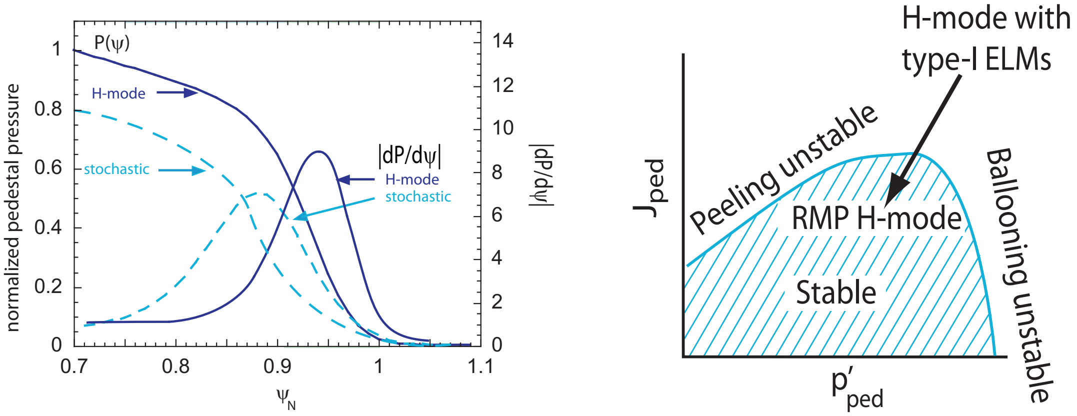

(a) Illustration of changes in pedestal pressure and pressure gradient as a result of the application of RMPs.

(b) Illustration of the peeling-ballooning stability diagram.

Figure 1.3: RMPs reduce the pedestal gradient making the discharge peeling-ballooning stable.

diffusion coefficient allows us to compare different experimental devices to assess if the resulting changes in transport (chapter 2) have a similar cause. A linear correlation between the weighed diffusion coefficient and the change in pedestal density is found for DIII-D H-mode. A similar calculation is performed for MAST L-mode discharges and again a linear correlation was found, but the offset and slope of the curve are significantly different from DIII-D H-mode data. We use this database to quantify which observed transport changes in the pedestal can explain the density pump-out and its correlation to the applied RMPs.

In chapter 4, the changes in turbulent drive terms, ion scale turbulence and $E \times B$ shear as a result of RMPs are presented for DIII-D H-modes and MAST L-modes. As a result of the different density pump-out behavior for similar weighed diffusion coefficients for DIII-D and MAST (chapter 3) indicates that the by RMP increased particle transport has a different origin. Since one of the main difference between the two experimental devices is the confinement regime (i.e. L-mode versus H-mode) an investigation of changes in turbulent transport is a sine qua non. We conclude that the changes in turbulent transport is a probable explanation for the density pump-out observed in MAST L-modes. However, the changes in $E \times B$ shear on DIII-D do not correlate with the changes in applied RMP, moreover the ion-scale turbulence in the pedestal area is reduced. This work is summarized in S. Mordijck et al. [54].

Due to the reduction in turbulence characteristics in the pedestal in RMP H-modes in DIII-D (chapter 4), we investigate in chapter 5 the increase of convective transport parallel to the magnetic field using a 2D fluid code as a possible particle transport mechanism for RMPs. These open field lines create a partial extended Scrape-Off Layer that penetrates in the pedestal area. With TRIP3D, the vacuum field line tracing code, we calculate the convective particle parallel transport coefficient, which is then added to the base transport of an ELMing H-mode, to investigate the changes in pedestal shape. We find very good agreement for different H-mode discharges. This work is summarized in S. Mordijck et al. [55].

Chapter 2

Effects of neutral fueling on pedestal density shape

2.1 Introduction

One of the challenges tackled in this thesis is to identify the cause of the observed density pump-out generated by resonant magnetic perturbations observed in DIII-D experiments. Before we can conclude that the changes in the pedestal density are the result of changes in transport, we need to investigate how altered neutral fueling influences the pedestal density's shape and whether it plays a role in the observed changes in pedestal shape.

2.1.1 Splitting of the seperatrix

Mathematically, the seperatrix, which is the boundary between closed flux surfaces in the core and open field lines in the Scrape-Off layer (SOL), consists of stable and unstable invariant manifolds and hyperbolic fixed points (X-points) [13]. In a perfect axisymmetric poloidally diverted tokamak, the stable and unstable manifolds associated with a hyperbolic fixed point overlap with each other and the traditional seperatrix. However, internal MHD modes, field-errors and applied external perturbations disturb the manifolds and cause the formation of homoclinic tangles. If the magnetic perturbation is strong enough, these homoclinic tangles intersect with the tokamak vessel structure [95, 96, 16, 100] and these structures, called lobes, become visible in the divertor area by means of: infrared cameras [22, 70, 38], visible cameras that observe D_α light or carbon impurities [22, 70], and Langmuir probes [90]. The creation of these lobes changes the interaction of the plasma with the divertor walls and the cryo pump. Wall surfaces that are not yet saturated with deuterium are wetted and pump particles from the plasma, reducing neutral fueling. Another facet is the interaction with the entrance to the cryo-pump and the created lobes, since the location and geometry of the traditional seperatrix in relation to the pump entrance determines the effectiveness of the pump [49].

2.1.2 Changes in particle balance

A density pump-out has been experimentally observed when applying RMPs [18, 14]. To understand where the particles in this density pump-out wind up, a careful particle balance is performed. Recently, E. Unterberg et al. [87] showed with a particle balance analysis that depending on the shape of the plasma in the divertor region, the particles can end up in the cryo-pump or in the wall and SOL. More specifically, E. Unterberg et al. [86] found that during the application of RMPs, the pumping efficiency changes. On one hand, in low triangularity ($< \delta >$) H-mode discharges in DIII-D, pumping decreases, whereas on the other hand in the ITER Similar Shape (ISS) H-mode discharges in DIII-D, pumping increases and remains elevated throughout the RMP application. Correlated with the pumping increase in these ISS discharges, the neutral density also increases. The changes in pumping were attributed to the distance of the traditional strike-point to the pump plenum entrance. However, a subsequent publication by E. Unterberg et al. [87] shows that location of the axisymmetric strike-point is not sufficient to explain the difference in pumping behavior between the low $< \delta >$ and ISS discharges.

Both plasma shapes also exhibit different behavior in recycling properties [87]. In low $< \delta >$ discharges, the amount of D_α light measured by the filterscopes decreases. This suggests that the particles exhausted by the plasma are pumped by the walls, or become part of the SOL. However, for the ISS shape, the measured

D_α light increases everywhere. Moreover, E. Unterberg et al. [88] show that at the midplane D_α increases by a factor 2 when compared to the RMP-off phase of the experiment, which results in higher neutral fueling rate of the core plasma.

All these changes in particle balance suggest a change in plasma interaction with the walls. To better understand how this interaction influences the density pedestal, we propose to perform numerical experiments with SOLPS5 [72], where we change recycling coefficients and pumping efficiencies. Next we compare the new density midplane profiles with the experimentally observed RMP density midplane profiles.

2.1.3 Effects of 3D strike point on pumping

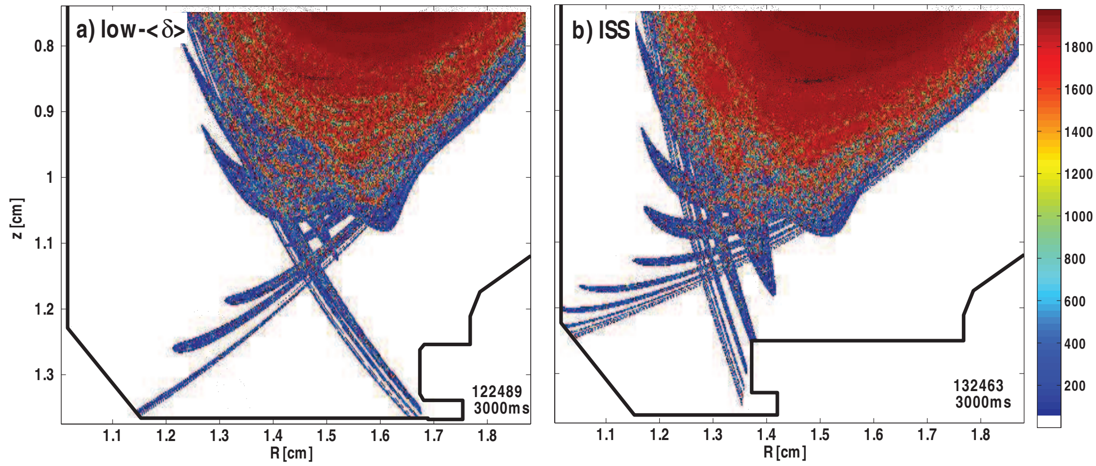

Figure 2.1: Comparison of toroidal cross section of magnetic vacuum calculation of 3D strike-point for a) low triangularity and b) ISS shape as a result of RMPs [88].

One potential problem with using a 2D fluid code like SOLPS5 is that it cannot handle the effects of the by RMP created 3D geometry of the strikepoint. The effects of 3D strike point on the pumping efficiency are investigated in [88]. They show that although the axisymmetric strike point can be in a similar location for two different plasma shapes (low $< \delta >$ and ISS), the way the homoclinic tangles interact with the divertor and entrance to the pump plenum determines

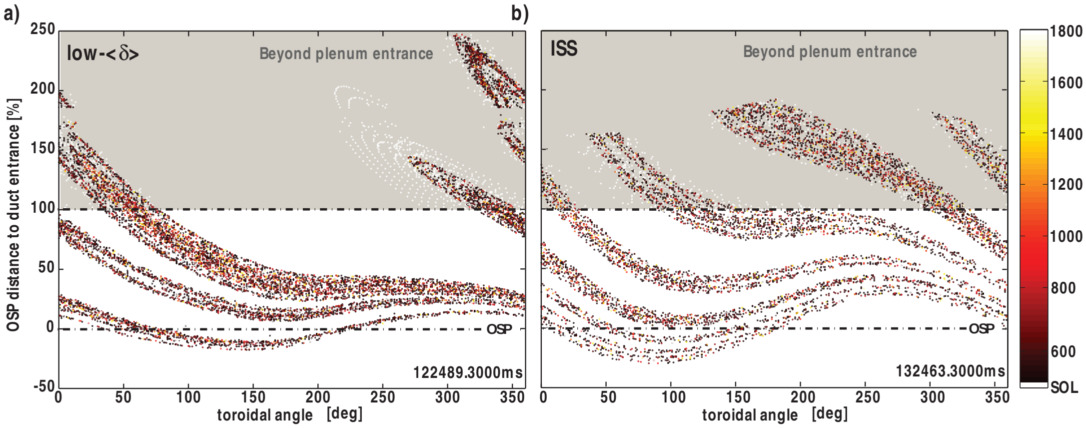

Figure 2.2: Comparison of 3D strike-point geometry on the divertor flow for a) low triangularity and b) ISS shape as a result of RMPs [88].

the changes in pumping efficiency.

For the low $< \delta >$ discharges, vacuum field line tracing calculations show that the homoclinic tangles intersect with the surface above the pump plenum (Figures 2.1 (a) and 2.2 (a). As a result, the pump is less effective in pumping particles and the filterscopes (monitoring the divertor area in front of the pump) also observe a reduction in amount of neutrals [88]. In the ISS shape plasmas the vacuum field line tracing calculations show an improved coupling to the pump plenum (see Figure 2.1 (b) and the footprint of the homoclinic tangle is nearly parallel to the pump entrance (see Figure 2.2 (b). Thus changes in 3D strikepoint result in changes in pumping capabilities. However as noted before, a 2D fluid code is not capable of handling the complex 3D geometry of the strikepoint, but we can artificially increase the pumping efficiency to simulate a similar effect. This allows us to compare the changes in upstream density versus experimental changes observed during RMPs.

2.2 Experimental data

To investigate changes in neutral fueling, we start modeling from a reference low $< \delta >$ ELMing H-mode. We compare the numerical results with data from a RMP H-mode, where the only difference with the ELMing H-mode is the use of an $n = 3$ perturbative field applied by means of the I-coils.

2.2.1 Time evolution

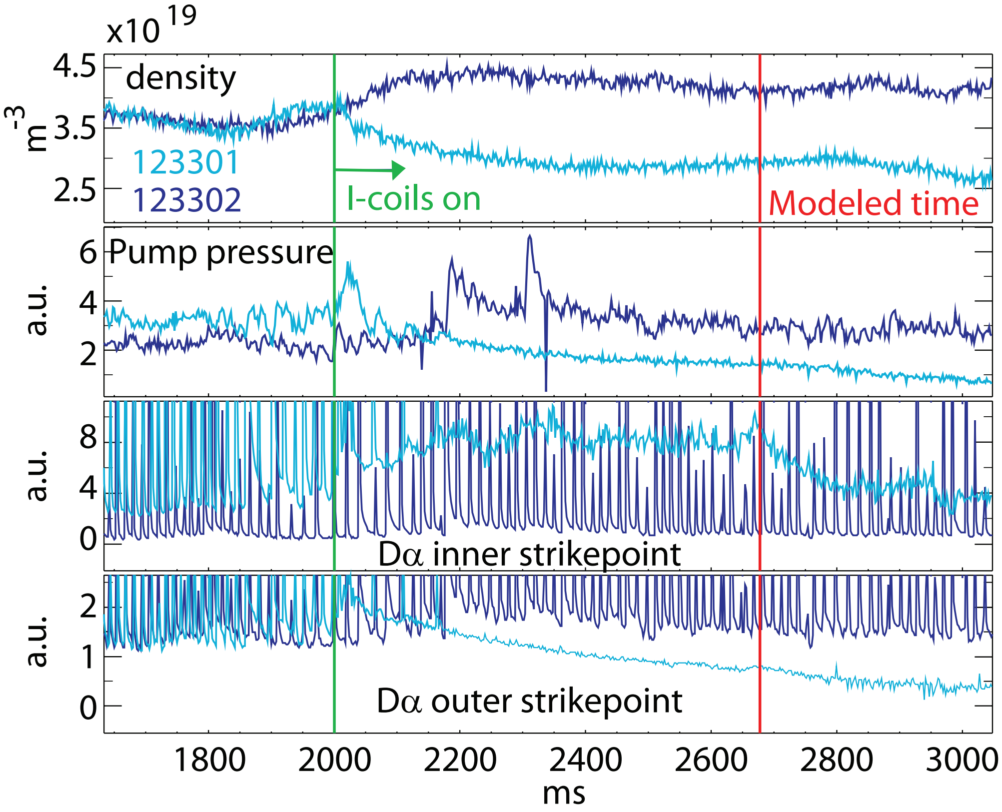

Figure 2.3: Evolution of two selected low $< \delta >$ discharges, respectively with (123301) and without RMP (123302) application.

In figure 2.3, two selected discharges (123301 and 123302) have an identically experimental setup, with the exception of the application of the 3.2 kA I-coil current in $n = 3$ even parity formation. The discharge without RMP application has type-I ELMs which can be observed by the spikes in D_α light at both strike-points. After energizing the I-coils, a few ELMs are still visible, but they are less frequent than before the application of RMPs and it takes 150 ms for the remaining ELMs to completely disappear. After the energizing the I-coils at 2000 ms, a density pump-out is observed in the line averaged density. Initially there is an increase in pumping that lasts 50 ms, but afterwards the pressure in the pump continues to decrease, which means that less particles are being removed from the plasma through the pump. Similarly measurements of D_α with the filterscopes near the outer strike-point also show a decrease, which can be correlated with a decrease in neutrals. However, D_α light at the inner strike-point increases. The decrease in D_α after 2700 ms at the inner divertor for the RMP discharge is correlated with the unset of MARFEs, an impurity instability [48].

To ensure steady state conditions, the modeling time is selected at a sufficiently distant time from when the I-coil was energized (at 2675 ms). This allows the plasma to come to a new equilibrium and avoid transient plasma changes as a result of RMPs.

2.2.2 Pedestal changes

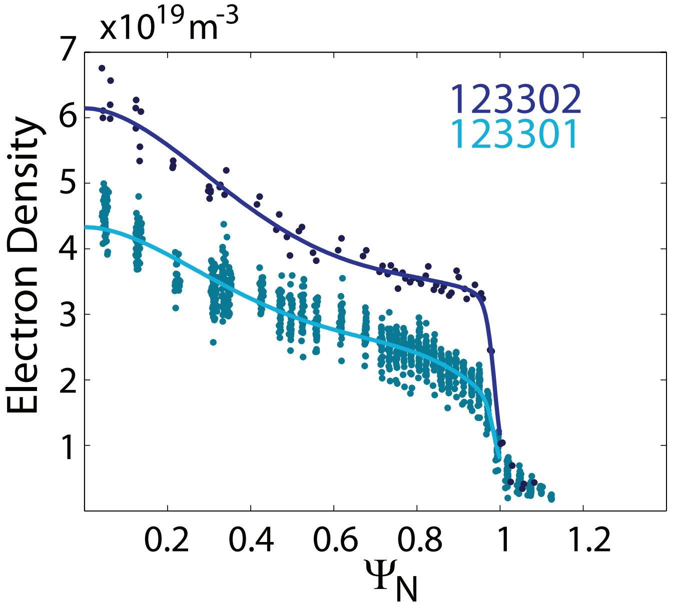

Figure 2.4: Experimental and *tanh* density pedestal profiles for two low $< \delta >$ discharges, one with (123301) and the other without RMP (123302) application.

Figure 2.4 shows the changes in pedestal density as the result of RMPs in a low $< \delta >$ discharge. The density is not only lower in the pedestal area ($\Psi_N \sim 0.9 - 1$), but the drop in density also propagates into the core of the plasma. From $\Psi_N = 0.7$ outward, the shape of the pedestal of the RMP H-mode is different from the ELMing H-mode. A more gradual drop in density is observed, resulting in a wider pedestal. Thus not only is the pedestal height lower, the pedestal is also wider. In the remainder of the chapter we show that these changes to the pedestal density are due to a change in particle transport and not only due to a change in neutral fueling.

2.3 Modeling approach

Ideally we would conduct an experiment to determine the effect of neutral fueling on the density pedestal change, however it is impossible to perform such an experiment, where we can change the neutral fueling rate from the walls in a controlled and knowing fashion. Experimentally there are two ways to alter neutral fueling; moving the outer strikepoint's location in relation to the pump plenum entrance, and/or adding a gas puff. With a gas puff a known source is added, which is toroidally localized and cools the plasma edge, which in turn influences the neutral fueling process in itself. The other option of moving the outer strikepoint, which results in an altered pumping efficiency is an indirect change in neutral fueling. However this also changes wall conditions and the plasma shape, all of which can influence both neutral fueling and the particle transport. Therefore, it would be difficult to interprete the results.

In this thesis we employ a different approach. Instead of trying to experimentally determine the main source of the pedestal density change, we employ a 2D modeling code of the plasma boundary, SOLPS5 [72], that consists of two codes, B2 and EIRENE [67]. B2, is a 2D fluid code, which uses Braginskii fluid equations [6] and Bohm-Chodura boundary conditions for the target plates [79]. The Monte-Carlo neutral modeling part, EIRENE, calculates self-consistently the changes in neutral density and ionization of neutrals depending on the plasma conditions (computed by B2) and given boundary conditions. SOLPS5 allows us to simulate both a change in wall recycling in specific areas as well as the pumping efficiency without altering any other parameters.

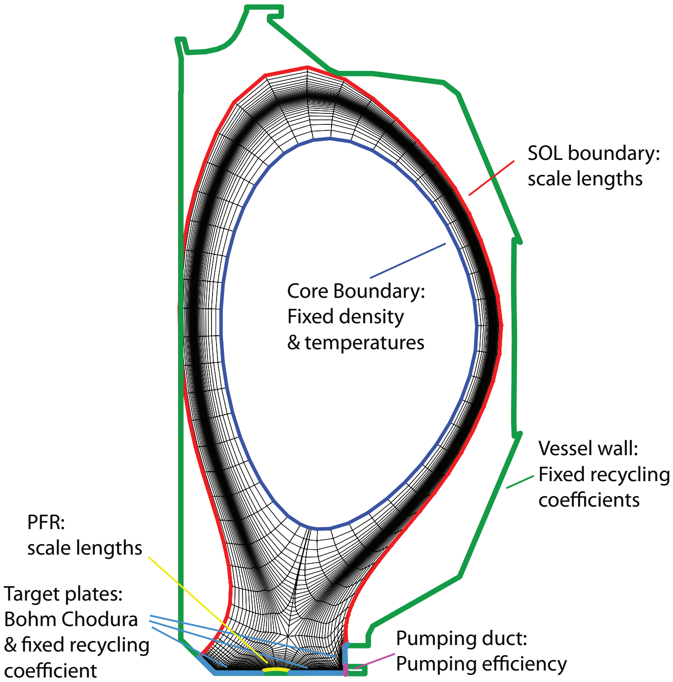

Figure 2.5: SOLPS5 grid with applied boundary conditions and indicated areas that are varied in the numerical experiments.

To obtain the correct plasma conditions, we calculate the radial transport coefficients by matching the experimental profiles for an ELMing H-mode (see section 2.4). Figure 2.5 shows an illustration of the 96x48 B2 grid in the DIII-D vessel with the different boundary employed conditions. At the core boundary we impose the measured experimental density and temperatures. At the SOL boundary and the private flux region(PFR), we impose an e-folding length that corresponds with experimental measurements. At the target plates, where the plasma interacts with the vessel wall, we employ a Bohm-Chodura sheath boundary condition and add flux limitations to better simulate the kinetic effects close to the target plates.

For the EIRENE boundary conditions, we impose a recycling coefficient of 1 at all the walls that are not in contact with the B2 grid, see Figure 2.5. At the target plates we employ a recycling coefficient of 0.97, to compensate for the fact that the walls are not fully saturated. At the entrance to the pump plenum we apply a recycling of 0.70. This translates into a pumping efficiency of 30%. In the numerical experiments discussed in section 2.5, we will change both the recycling at the target plates and the pumping efficiency and illustrate how these changes affect the density pedestal.

In the following sections (2.4 to 2.6), we discuss the results for the numerical simulations in more detail.

2.4 Transport model for ELMing H-mode

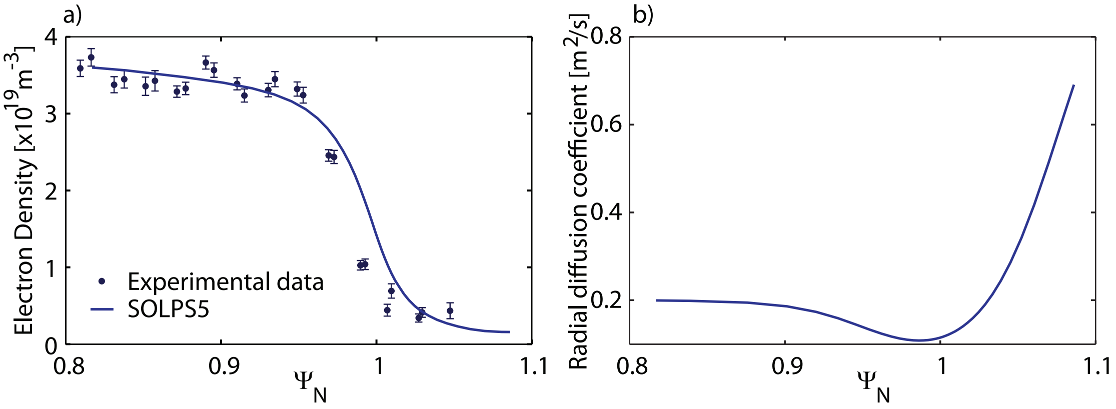

Figure 2.6: SOLPS5 calculations for a) density pedestal profiles for a low $< \delta >$ ELMing H-mode discharge b) the radial diffusion coefficient needed to match the SOLPS5 modeling to the experimental data.

The transport model is derived by matching the experimental midplane profiles. Figure 2.6 (a) shows the measured electron density with experimental error bars. The solid blue curve is the fitted SOLPS5 data. The values for the particle diffusivity (see Figure 2.6) (b), are the same magnitude as [32] and comparable to commonly used estimates, i.e. 0.2 in the core, a transport barrier and 0.7 at the outer edge of the SOL. Note that only one probe measurement is available near the outer strike-point. The peak values given by our simulation are within a factor of 2–3 of the probe measurements.

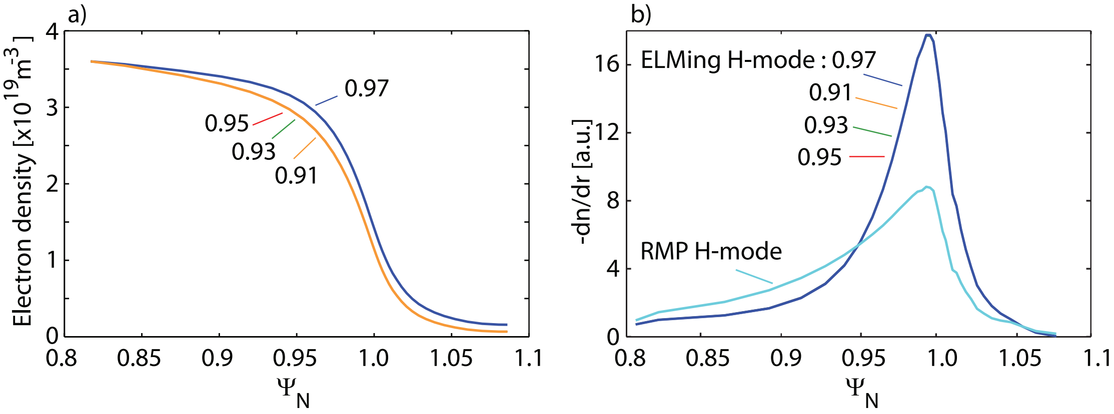

Figure 2.7: Changing the recycling coefficient in the divertor from 0.97 to 0.91 has little effect on the a) density profile or b) density shape.

2.5 Numerical experiments of neutral fueling

We fix the radial transport coefficient from the previous section. In this section, we change the recycling coefficient at the target plates from 0.97 to 0.95, 0.93 and 0.91, and observe a reduction in the pedestal density profile, see Figure 2.7 (a). The density profile drops over the outer extend of the radial simulation (with exception at the inner core boundary where a fixed density is set), as a result of the reduced recycling in the divertor. This can be explained by an increased number of plasma particles that are now captured by the walls at the target plates, instead of being recycled as neutrals, that can re-ionize and fuel the core. The changes to the pedestal shape as a result of the reduction in recycling are compared to the shape of the RMP pedestal, see Figure 2.7 (b). Nearly no change in shape is observed for numerical experiments with lower recycling. The density gradient of numerical simulations with lower recycling needs to be lower in the steepest region of the pedestal and to increase at the top of the pedestal to match the experimental results for the RMP H-mode. Moreover, the peak density in the divertor is reduced by a factor 1.5 from a recycling coefficient of 0.97 to 0.91. In experiments however, the change is more dramatic and the density peak is reduced by a factor 3. This leads us to conclude that changes in recycling in the divertor area cannot explain the observed experimental changes in pedestal shape of a RMP H-mode.

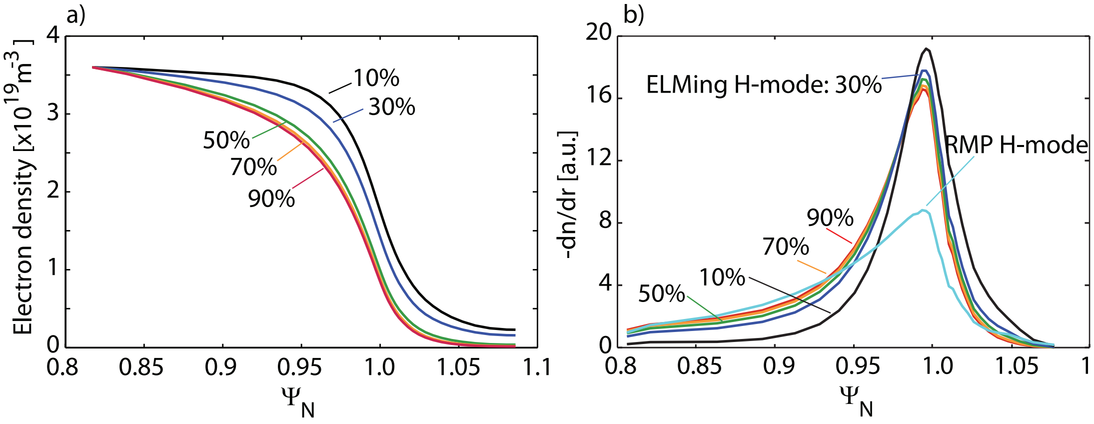

Figure 2.8: Altering the pumping efficiency from 10 % to 90 % has a strong influence on the density profile (a). This also strongly affects the shape (b).

Changing the pumping efficiency from 10–90% shows again the importance of neutral fueling (see Figure 2.8 (a). We were unable to obtain results with 0% pumping, due to the fixed density boundary condition in the core. The amount of neutral fueling increased dramatically, resulting in an unstable numerical simulation. The largest changes are observed from 10% upto 50% pumping efficiency. From 50% to 90% the changes are more subtle. At a first glance this can be attributed to chosen core boundary condition. However, due to the fact that the radial transport is the same for all the simulations, the density gradient for all the simulations is very similar at the core boundary condition (see Figure 2.8 (b). This results in a similar fueling particle flux from the core and therefore a different boundary condition would have resulted in similar limited changes for increased pumping efficiency from 50% upto 90%. In Figure 2.8 (b), we can also observe that the gradient in the steepest part of the density pedestal is reduced by increased pumping, however the necessary reduction to achieve an RMP H-mode is still not achieved.

From these simulations we can observe a drop of a factor 4 in peak density from 30% to 90% pumping efficiency. Reducing pumping efficiency from 30% to 10% increases the density peak by a factor 2. The changes in density peak in the divertor are of a similar magnitude as those observed for RMP H-mode. However, as seen in figure 2.8 (b), the changes in density pedestal shape are insufficient to obtain an RMP H-mode density pedestal.

2.6 Transport changes for RMP H-mode

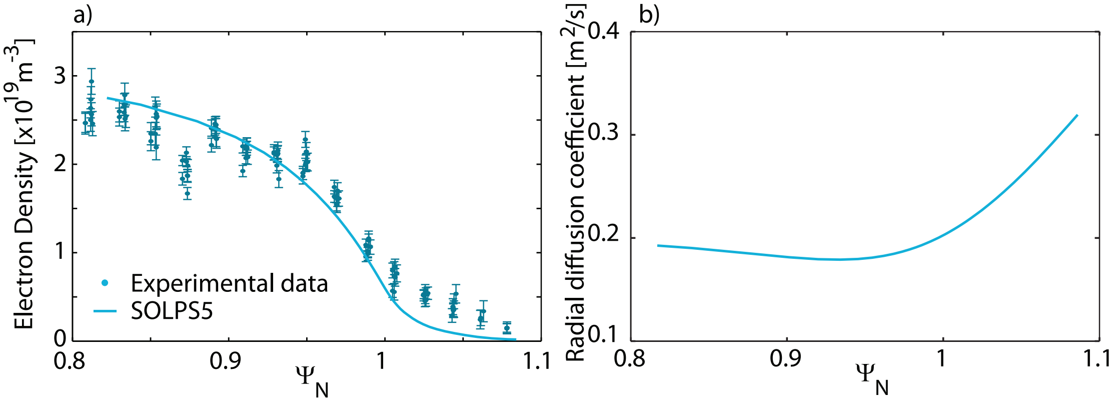

Figure 2.9: SOLPS5 calculations for a) density pedestal profiles for a low $< \delta >$ RMP discharge b) the radial diffusion coefficient needed to match the SOLPS5 modeling to the experimental data.

In the previous section we showed that neither wall-pumping nor improved pumping efficiency can explain the changes in the density pedestal profile. We therefore impose similar recycling and pumping efficiencies as for the ELMing H-mode. Similarly as for the ELMing H-mode, we match upstream profiles by altering the radial transport coefficients until we find the best fit to the data. Figure 2.9 (a) shows the experimental data points with error bars and the SOLPS5 fit to the data. The resulting radial transport coefficients are shown in figure 2.9 (b). The transport coefficients are nearly identical to the transport coefficients of the ELMing H-mode up to $\Psi_N = 0.9$. From $\Psi_N = 0.9$ upto the seperatrix region, the transport is slightly larger. We also observe that in the SOL the radial transport coefficients are smaller than for the ELMing H-mode.

2.7 Discussion

The density pump-out that is observed in RMP H-modes cannot solely be the result of changes in neutral fueling. While changes in pumping efficiency can reduce the density in the core, it also reduces the density in the SOL. From this we can conclude that creating an extra sink for neutrals is not enough to explain the pedestal shape changes observed in an RMP H-mode. Consequently, we derive radial transport coefficients by matching the experimental profiles. These transport coefficients are slightly different from the ones in the ELMing H-mode. However, the changes are small and might fall within experimental error margins.

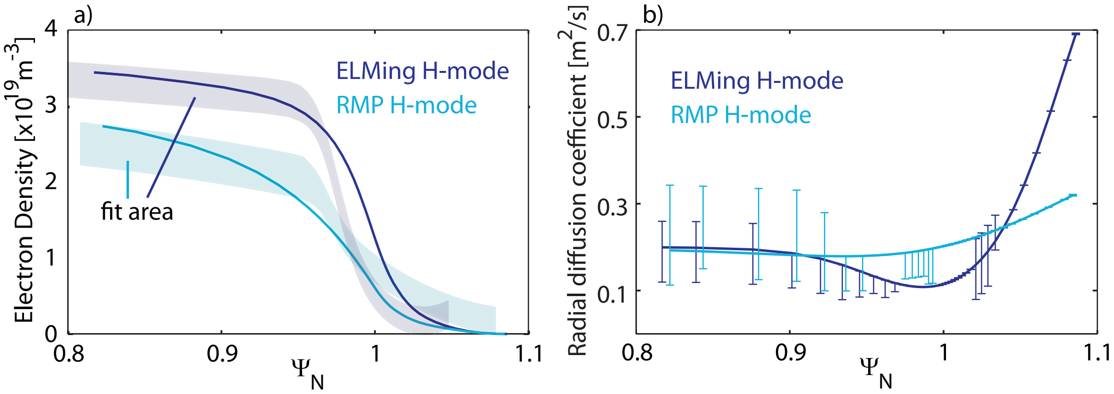

Figure 2.10: (a) Error bar region for experimental density profile based on data spread and tanh fit to the pedestal. (b) Radial diffusion coefficient with error bars according to the experimental fitting area.

In figure 2.10 (a) a density region is determined based on the experimental data points, their error bars and the tanh fit for the ELMing H-mode and the RMP H-mode. The best SOLPS5 fit to the data are shown as solid curves in Figure 2.10 for both experiments. The corresponding transport coefficients are shown on the right. We then vary the transport coefficients and recalculate the density profiles with SOLPS5. For each radial point, the SOLPS5 calculation is compared to the density region. Once the simulated density falls outside the error bar region, this determines the extreme of the error bars on the transport coefficients.

Figure 2.10 shows that, although the change in particle transport from the

ELMing H-mode to the RMP H-mode is small, it falls outside error bars. This is therefore a meaningful change from Ψ_N 0.9 to 1. However, SOLPS5 can only indicate that there is a change in transport, it cannot identify which transport channel is altered. There are multiple options for changes in transport. Some are the direct consequence of a 3D magnetic topology while others are the result of an altered background plasma. In this thesis, we will first investigate if there is a direct correlation between the applied perturbation and the density pump-out. Next, we investigate changes in turbulent behavior in RMP plasmas, by comparing DIII-D H-mode results to MAST L-mode results. Finally, we consider the possibility that the RMPs open field lines inside the seperatrix, leading to an increased parallel particle transport, similar to the parallel transport in the SOL.

2.8 Conclusion

Experimental evidence shows that the particle balance is altered when RMPs are applied in DIII-D H-mode plasmas. Changes in D_α light in the divertor and at the midplane suggest changes in neutral fueling rates. However, the changes are dependent on the plasma shape of the experiments. Vacuum calculations of the 3D strike point show a good correlation with the observed changes in pumping efficiencies: Strike point alignment with the entrance to the pump results in higher pumping rates.

Numerical experiments to change the neutral fueling rates with SOLPS5 confirm a density pump-out. However when comparing the changes in pedestal shape with the shape of an RMP H-mode, the changes in neutral fueling are not sufficient. An increase in particle transport is needed to fit the RMP H-mode profiles. When investigating the sensitivity of the change in particle transport, we found it to be small but significant. This work was summarized in [53].

Chapter 3

Correlating density pump-out with applied RMPs

3.1 Introduction

In the previous chapter we showed that the observed changes in pedestal density shape can only be the result of changes in particle transport. Several theories on particle transport and RMPs have been proposed to explain the density pump-out. The different theories, which will be discussed in the subsequent sections, are based on experimental data from different experimental devices, plasma equilibria and magnetic perturbations spectra. This raises the question whether the density pump-out created by RMPs is always the result of the same changes in transport, or if plasma shape (i.e. no X-point versus 1 or 2 X-points), type of magnetic perturbations (i.e. resonant versus non-resonant), plasma equilibrium conditions (i.e. L-mode versus H-mode),or collisionality play a role.

In this chapter, we develop a technique that allows us to compare experiments performed on different experimental devices, in order to investigate if the RMP induced changes in density are the result of one or more transport channel changes. This technique, based on an integrated weighted stochastic diffusion coefficient, D_{OFL}, enables us not only to compare different experimental devices, but also different plasma equilibria conditions (ex. L- versus H-mode) and different magnetic perturbation spectra (ex. resonant versus non-resonant). Comparing databases of experimental discharges allows us to investigate if the observed density changes can be linked to a particular theory for the increase in particle transport as a result of RMPs or if the changes dependent on the plasma background conditions to which the RMP is applied.

First, we give an overview of the different theories on enhanced particle transport as a result of RMPs. Next, we introduce the large database of low collisionality H-mode discharges on DIII-D. This database contains experiments with different plasma shapes, q-profiles and RMP spectra. We show that there is no visible correlation between the density pump-out and the applied I-coil current. Subsequently, we introduce the computation of an integrated weighted magnetic diffusion coefficient, D_{OFL}, that behaves non-linearly with respect to the I-coil current magnitude and the resonant radial component of the RMP on the 11/3 surface, $b_r^{11/3}$. Finally, we show that when using this more complete representation of the magnetic field perturbation, the density pump-out correlates with the applied RMP. We illustrate that this technique can be employed to compare different experimental plasma conditions: ex. we compare DIII-D low collisionality H-mode data with MAST L-mode data by using D_{OFL}.

3.1.1 Stochastic particle transport

Stochastic particle transport is among the most popular theories to explain the density pump-out observed in RMP experiments. The seminal paper by Rechester and Rosenbluth [64] discusses particle and heat transport in a collisional and collisionless plasma regime where magnetic surfaces are completely destroyed and become stochastic. They link stochastic transport directly to the width of magnetic islands, that can be described by the resonant radial magnetic field component, $\delta b_r^{m/n}$ on a resonant magnetic surface:

$$D_{st} = \pi R \sum_{m,n} \frac{b_{mnr}(r)}{B_z^2} \delta \left(\frac{m}{g(r)} - n \right). \tag{3.1}$$

Here D_{st} is the magnetic stochastic diffusion coefficient and has units of m. R is the major radius, m is the poloidal mode number, n the toroidal mode number, b_{mnr} is the radial component of the resonant magnetic field, B_z is the toroidal magnetic field and $g(r) = m/n$ which is also called the safety factor q. In a collisionless regime, multiplying D_{st} with the sound speed, c_s, results in a stochastic particle diffusion coefficient, D_M, whereas multiplying with the electron thermal speed, v_{T_e}, gives the electron heat conductivity, χ_e.

Joseph et al. [41] extensively compare the theoretical quasi-linear approach of stochastic transport with the observed experimental profile changes and resulting estimates for particle and heat transport. They find that $D_M = 0.3 - 0.4\,m^2/s$ is of the correct order of magnitude, and only slightly larger than one found with the CORSICA code, a 1D transport code [11]. However, the electron thermal diffusivity, $\chi_e = 20\,m^2/s$ is two orders of magnitude too large, when compared to experimental values. Joseph et al.'s conclusion is that the magnetic field must be screened, due to high toroidal rotation, to explain the discrepancy between the theoretical electron heat transport and the experimental values.

Evans et al. [14] also performed a quasi-linear estimate of stochastic transport and obtain much larger values than Joseph et al. [41], see table 3.1. Their results are based on a different experimental discharge. Nevertheless, this experiment has a similar setup as the one described by Joseph et al. [41]. Consequently, it is not clear what the source of the disagreement between [14] and [41] is.

Yan and Evans [100] also calculate D_{st}. However, they employ a field line tracing code, TRIP3D [19], in order to calculate the radial displacement in Ψ_N space:

$$\langle D_{st}^{\Psi} \rangle = \frac{1}{M} \sum_{i=1}^{M} \delta\Psi_i^2 / 2L_i. \tag{3.2}$$

Here M is the amount of field lines started on a flux surface, $\delta\Psi_i^2$ is the radial displacement of the field line in Ψ space and L is the length of the field line. Both equations 3.1 and 3.2 come from the same idea that $D_{st} = \langle \Delta r^2 \rangle / L$. While, D_{st} in Rechester and Rosenbluth is a quasi-linear approximation, Yan and Evans use a field line tracing code, which makes it possible to calculate the exact length and radial displacement of the field line. As a result the calculation of D_{st} is not restricted to rational surfaces, but can be performed on any surface in the plasma. Yan and Evans' [100] results are an order of magnitude smaller than those presented in Evans et al. [14].

Stacey and Evans [78] employed a weighted stochastic magnetic diffusion coefficient. They use the same D_{st} as Yan and Evans, but multiply this coefficient with the field line loss fraction. This is the fraction of field lines that hit the vessel wall versus all field lines started on that same flux surface with the field line tracing code. They only published the results for the electron thermal heat coefficient, which is slightly smaller than the calculation by Yan and Evans [100]. This suggests that D_{st} and D_M will also be smaller than those by Yan and Evans [100].

Table 3.1: Different results in the literature for stochastic magnetic diffusion.

	Joseph et al. [41] Quasi-linear	Evans et al. [14] Quasi-linear	Yan and Evans [100] Field line tracing	Stacey and Evans [78] Field line tracing
D_{st}		$3.5 \times 10^{-6}\,m$	$4.6 \times 10^{-7}\,m$	
D_M	$0.3 - 0.4\,m^2/s$	$2\,m^2/s$	$0.29\,m^2/s$	
χ_e	$20\,m^2/s$	$49\,m^2/s$	$6.7\,m^2/s$	$3\,m^2/s$

We have summarized the results found in the different articles on stochastic magnetic diffusivity in table 3.1. All articles, with exception of Joseph et al. [41] are calculations based upon the same experimental discharge, but using different techniques. This illustrates the extreme non-linear behavior of the field lines, because the quasi-linear approach results overestimate the stochastic transport for RMP experiments when compared to the field line tracing calculations.

3.1.2 MHD transport

Applying perturbative magnetic fields always leads to a plasma response. There are several theories on plasma response, ranging from ideal MHD to resistive

MHD, or rotational screening models. This section will give a brief overview of how different models of plasma response can affect particle transport.

Generally the application of small radial magnetic fields are associated with a drag on the plasma rotation. Recently researchers have made a distinction between resonant magnetic fields and non-resonant magnetic fields. Resonant magnetic fields induce an electro-magnetic braking torque on the plasma [30]. Non-resonant magnetic perturbations on the other hand can damp the flow as explained by neoclassical toroidal viscosity (NTV) [9]. Recently, it has been shown that NTV does not only damp flow, but can also lead to a spin up of the plasma rotation, leading to a higher energy confinement [77]. In these cases it was shown that the $E \times B$ shearing rate increased and modeling showed a reduction in the ion temperature gradient modes [77]. Therefore, both resonant and non-resonant magnetic perturbations can indirectly lead to changes in particle confinement, by influencing the momentum balance and growth rates for turbulent transport.

Resistive MHD modeling results [59, 36] indicate that RMPs can have a direct influence on particle transport by creating $E \times B$ convection cells close to the seperatrix. However, the resistivities employed in these simulations are much higher than those encountered in DIII-D H-mode experiments. Nardon et al. [59] show that lowering the resistivity in the simulations also decreases the influence of the convection cells. Depending on the scaling of convection cells with resistivity, convection cells are a possible source of the observed density pump-out.

3.1.3 Transport along open magnetic field lines

A popular recent explanation for the density pump-out is based on the creation of open field lines inside the traditional seperatrix, thus partially extending the Scrape-Off layer. Jakubowski et al. [40] are the first to connect the calculated vacuum magnetic topology with 2D experimental imaging on TEXTOR. In their paper they show that the structures observed with a visible camera of the C_{III} light match the magnetic topology determined using a vacuum approximation. The magnetic topology is separated in two distinctive zones: the ergodic zone and the laminar zone. The laminar zone is defined as the region where field lines have a connection length which is shorter than the Kolomogorov length. The ergodic zone is the region where field lines have a connection length which is longer than the Kolomogorov length [31]. The Kolomogorov length is a measure of the e-folding length of the exponentially growing separation of neighboring trajectories and is defined as [31]:

$$L_K = \pi q R_0 \left(\frac{\pi \sigma_{Chir}}{2}\right)^{-4/3}. \tag{3.3}$$

Here q is the safety factor, R_0 is the ratio of the B-field with the current and σ_{Chir} is the Chirikov parameter. The Chirikov parameter is a measure of island overlap: it is the ratio of the size of two neighboring islands divided by the radial distance between those islands.

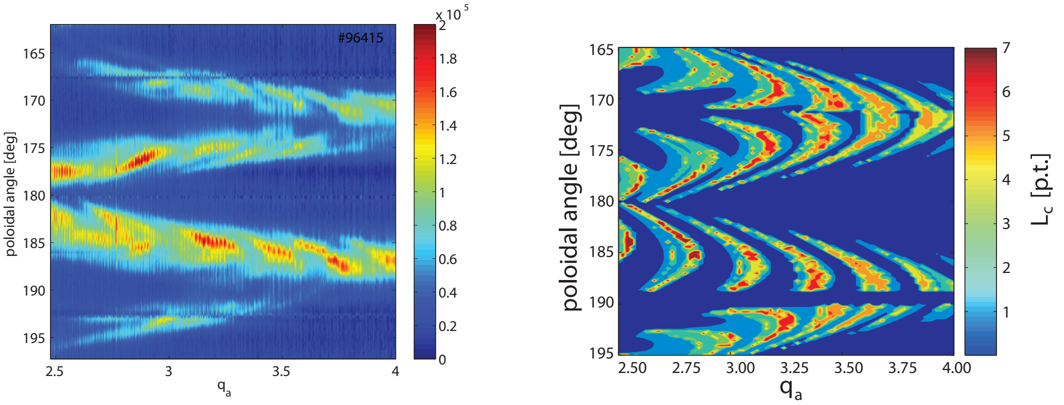

(a) Experimental heat measurement of 3D structures during a q-scan in TEXTOR.

(b) Vacuum field line tracing calculations of 3D structures during a q-scan in TEXTOR.

Figure 3.1: Comparison of simulated and experimentally determined 3D heat structures in TEXTOR with during a q-scan.

The laminar zone in a limiter device is similar to a SOL in a poloidally diverted tokamak: The parallel transport along open field lines dominates over the cross-field transport. In fact, Jakubowski et al. [37] show that the heat flux creates a strike point pattern on the wall which corresponds to the calculated strike point pattern from the magnetic perturbations. They also show that depending on the penetration depth of the laminar zone, the heat deposition is different.

Another aspect that alters the heat deposition pattern is collisionality. A density scan shows that at higher densities, the heat flux pattern is more smeared out as a result of higher cross-field transport. A closer examination of field line tracing footprint structures by Jakubowski et al. [39] shows that the strike point pattern has internal structures with short connection lengths (see Fig. 3.1b) that penetrate deeper than the surrounding field lines. This exact pattern is also observed in the heat flux to the vessel wall (see Figure 3.1a). All this indicates that perturbations at the plasma edge create an extended SOL layer (laminar zone) where parallel transport dominates over cross-field transport at low collisionality.

Schmitz et al. [71] continues the work of comparing experimental 2D imaging with calculated magnetic structures for TEXTOR experiments and makes the first comparison with 3D fluid modeling. The same analysis as for TEXTOR was also performed for DIII-D [70]. More extensive 3D fluid modeling for DIII-D illustrates that increased cross-field transport smears out the strike-point pattern [28]. 3D fluid modeling shows good agreement with experimental profiles for changes in particle transport, but vastly over estimates the heat loss. Similar results for the heat flux were reported by Ilon et al. [41].

3.1.4 Neoclassical transport changes

Where the creation of the laminar zone and the free-streaming of electrons, discussed in the previous section, agrees well with experiments, ions have a much shorter mean free path than electrons. Tokar et al. [85] discuss, based on ambipolarity, how the radial transport of ions increases. They argue that if the radial electric field is different from the ambipolar electric field, a poloidal viscous force leads to an outward drift of the ions. As a result, the radial electric field changes from its negative neoclassical values to a positive ambipolar electric field. This agrees quantitative with experimental results from Moyer et al. [57].

To explain the unexpected results for the electron temperature profile, which does not decrease as theoretically predicted by the stochastic transport theory and even increases slightly in certain cases [18]), Tokar et al. [84, 83] remind us that perpendicular neoclassical heat transport in a colisionless system is proportional to the density squared. Moreover, the increase in parallel heat transport is limited in a collisionless system by the non-locality of heat transport and kinetic flux limitation.

A recent publication by G. Park et al. [63] shows results that are similar to Tokar et al. [84, 83] calculated with an ion-electron-neutral guiding-center code. They find that the toroidal rotation is damped by a $\vec{j} \times \vec{B}$ ion torque and that the E_r profile goes from negative to positive, comparable to the ambipolar electric field. However, the simulated changes as a consequence of RMPs are too large (especially close to the seperatrix), so they introduce an ad-hoc screening factor to give results, that are in good agreement with experimental observations. However, the overestimation of changes close to the seperatrix (where the laminar zone is located) could be the result of the assumption in the code that the electro-static potential is fixed on a flux surface. This assumption is an accurate approximation for closed flux surfaces in an axisymmetric system, however for field lines that have a short connection length to the target plates, the electro-static potential is not constant along a field line.

3.1.5 Turbulent transport changes

A lesser explored transport mechanism to explain the density pump-out, is turbulent transport. Rozhansky et al. [68] also start from neoclassical principals (see previous section), and expand to include effects of anomalous transport. Using a version of SOLPS5, that has been adapted to include neoclassical transport effects, they show that for H-mode modeling on MAST a screening factor is necessary. Without a screening factor the stochastization is too large yielding in an overestimation of particle transport. However for L-mode modeling on MAST they find that the stochastization in itself is not enough to explain the density pump-out. An increase in anomalous transport is needed to explain the observed changes.

A recent publication by Tamain et al. [80] confirms that in MAST L-mode discharges the anomalous transport increases as a result of RMPs. They show that the changes in turbulent transport are not the result of a lower density, but a direct consequence of applying a magnetic perturbation. This is different from previous ion scale fluctuation measurements in limiter L-mode plasmas on TEXTOR [99] and TORE-SUPRA [12], where a decrease in fluctuation levels was observed.

Earlier work [98] on turbulence measurements in TEXTOR shows that the turbulent particle flux, $< T_{fl} >$, changes from locally outward, to locally inward as a result of the phase shift between $\tilde{E}$ and $\tilde{n}$ in the ergodic zone. However the total particle inventory does not increase and therefore created stochastic transport compensates the turbulent changes. These changes cannot be explained by a change in local $E \times B$ shear modifications. In Xu et al. [97], this analysis is extended to show that the reversal of the turbulent particle flux dependents on the applied magnetic spectrum. In the ergodic zone turbulence properties are modified by quenching of coherent modes. A reduction in the radial and poloidal correlation lengths occurs with suppression of large-scale turbulence eddies and wavenumber broadening is observed at all frequency components. In the laminar zone, the turbulence correlation length increases and Reynolds stress is generally suppressed independent of the applied magnetic perturbation spectrum. This implies a rearrangement of the poloidal momentum profile.

The only work on turbulent transport changes in RMP H-mode plasmas was performed on DIII-D [58, 57]. Moyer et al. [58] show that for high collisionality H-mode discharges there are no changes in the radial electric field although the magnetic fluctuations increase. Moyer et al. [57] compare two discharges, with and without RMP, for low collisionality plasmas. The results in low collisionality are completely different from those at high collisionality. Where at high collisionality no changes in the E_r profile are observed, at low collisionality the radial electric field becomes positive. As a result, the $E \times B$ shear increases outside $\Psi_N = 0.9$ and decreases inside $\Psi_N = 0.9$. At the same time, FIR coherent scattering (a non-localized measurement) shows that there is an increase in turbulence. Measurements of the pedestal with the homodyne reflectometry show changes in the character and amplitude of the fluctuations. Moyer et al. [57] conclude that particle transport increases as a result of an increase of ion scale drift wave turbulence or the creation of convective cells.

3.1.6 Discussion

The previous sections illustrate the wealth of theories on increased particle transport due to RMPs. Most of these theories are supported by experimental evidence. However, the experimental evidence is obtained in different experimental devices, with different plasma conditions and different magnetic perturbation spectra. This makes comparison and validation of the different theories difficult and illustrates the need to find a technique to compare the density pump-out between the different experimental devices.

In this chapter we will show that the density pump-out is correlated with the applied RMPs, but that the magnitude of the density pump-out can differ by an order of magnitude between two machines with completely different plasma conditions. The results suggest that the density pump-out is the result of different transport mechanisms.

3.2 Database with DIII-D H-mode discharges

As illustrated in the introduction, there are several possible explanations as to how resonant magnetic perturbations alter particle transport. The validity of these explanations depends on the equilibrium plasma conditions before RMP is applied. Therefore it is important to develop a database of experimental discharges and find commonalities and differences for different sets of plasma conditions. The most direct method of comparing the changes in particle transport with the applied perturbation is by comparing the density pump-out with the applied I-coil current, as shown in Figure 3.2.

In figure 3.2 the density pump-out is plotted versus the applied I-coil current. No clear trend can be observed. The database of experimental discharges in figure 3.2 consists of low collisionality H-mode discharges on DIII-D to which the even or odd parity I-coil configuration is applied. Figure 3.3 shows the two main different plasma shapes that are considered in this database. Different shapes determine the position of the plasma in relation to the coils. The distance to the coils is important, especially since these are lower single null discharges, the plasma is

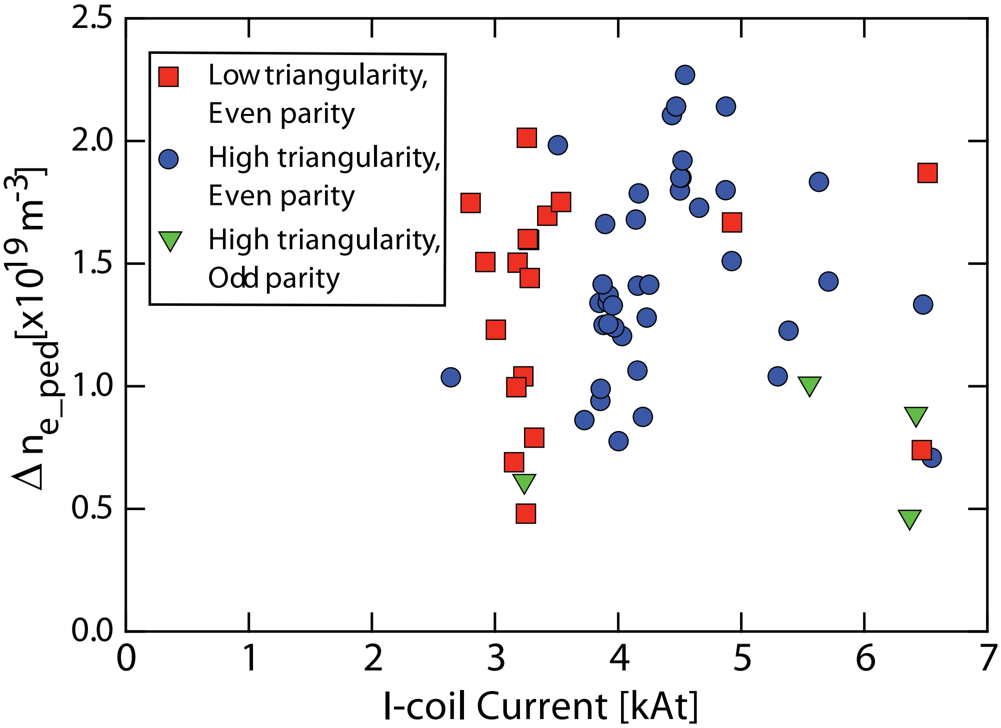

Figure 3.2: Correlation of I-coil current with density pump-out.

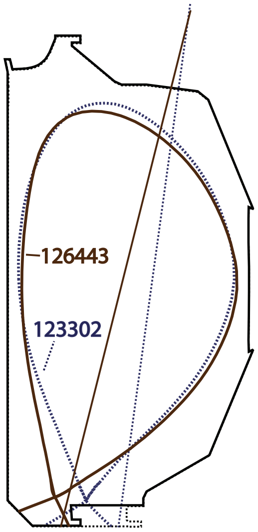

Figure 3.3: Two representative equilibrium plasma shapes from the RMP database. 123302 is a low $< \delta >$ discharge and 126443 is the ISS shape.

not up down symmetric. The shape changes are the largest in the lower half of the plasma and therefore the lower row of I-coils might have more or less influence on the spectrum and magnitude of the B-field.

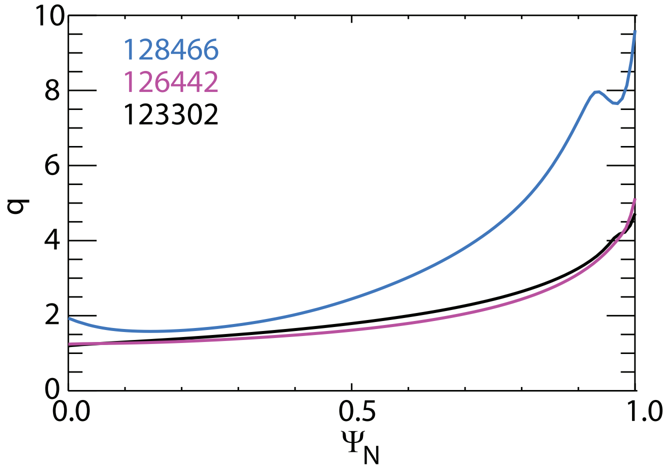

Figure 3.4: Different q-profiles in RMP database. 123302 is a low $< \delta >$ discharge, 126443 is an ISS and 128466 is an ISS discharge with $q_{95} = 7.2$.

In figure 3.2, we differentiate between the different plasma shapes and applied spectra. However, even when the discharges with similar shape and spectrum are compared, no clear trend can be observed. Although, we already separate shape and applied I-coil spectrum, we do not incorporate the fact that the spectrum is very sensitive to the q-profile of the equilibrium plasma. This database contains discharges with different q-profiles, see figure 3.4. The q-profile determines the position and distance between the rational surfaces. The position of the rational surface partly determines the strength of applied RMP field on that surface and the distance between the rational surfaces is important for island overlap. The q-profile is therefore very important to determine the vacuum prediction of the edge-stochasticity and resulting particle transport.

The above described topics are related to the limitations of the I-coil current as a complete description of the applied RMPs. A practical challenge in creating such a database of discharges is the definition of density pump-out. To obtain such a large database of discharges, the density pump-out is quantified as the difference in pedestal density from before the I-coil activation to afterwards. As

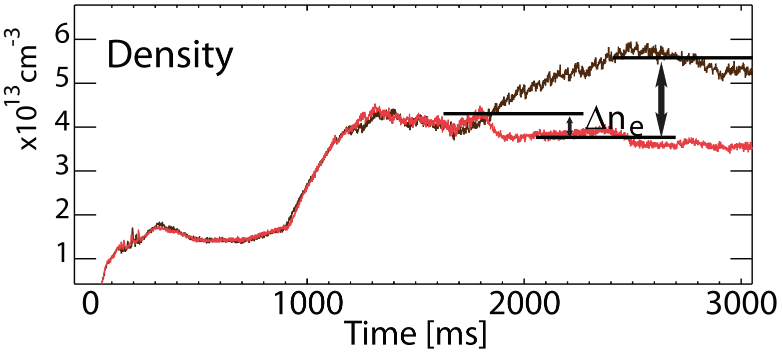

Figure 3.5: Definition of density pump-out.

illustrated in figure 3.5, some RMP discharges have not reached a steady-state density when the I-coil is activated, whereas some have. To eliminate transient effects of establishing a steady-state H-mode discharge, the density pump-out needs to be compared to a reference discharge, without I-coil application. This limits the amount discharges that are suitable for comparison. Often in past experiments, there are only a limited number of reference discharges that truely mimic the RMP H-mode discharges, without altering other input plasma parameters.

3.3 Calculation of a weighted magnetic diffusion coefficient

In section 3.2, we illustrated the limitations of using I-coil current as a parameter to define the amount of RMP applied to the plasma. In this section, we introduce the calculation of a weighted magnetic diffusion coefficient, D_{OFL}. D_{OFL}, allows us to compare different plasma shapes with different q-profiles and RMP spectra. This technique can help identify how RMP induced transport depends on plasma equilibrium conditions.

3.3.1 Benefits of using field line tracing

As illustrated in DIII-D H-mode discharges, the I-coil current alone fails to accurately quantify the applied magnetic perturbation. Using a field line tracing code allows us to make a direct computation of the impact of the applied magnetic perturbation. The most important limitation in using a field line tracing code is the lack of a plasma response model. We overcome this problem by limiting the comparison to plasmas with similar equilibrium conditions only, thus assuming that the plasma response will have the same impact in all experimental discharges.

The advantages of using a field line tracing code are numerous. First, it allows us to compare different plasma shapes in a single experimental device. Second, this allows us to investigate if the plasma shape changes the type of particle transport as result of RMPs. Third, it also accommodates changes in the spectrum, that result from a change in I-coil configuration or q-profile. Fourth, using a field line tracing code allows us to expand the database to include discharges from different experimental devices, which can have completely different shapes, plasma conditions and spectra. A fifth advantage is that by using a field line tracing code, all the resonant as well as non-resonant effects are included. In contrast, when comparing only the resonant phenomena, two practical questions arise:

1. Which resonant surface should be used for comparison,
2. how does the extreme non-linearity of the stochasticity affect the linear approach.

Finally, D_{OFL} is limited to the plasma edge by using the field line loss fraction as a weighting function. Only field lines close to the plasma edge change from closed to open in the vacuum picture. This avoids including vacuum calculations deeper in the core, where ideal MHD calculations have shown good agreement with experiments [65].

3.3.2 Calculation of D_{OFL}

To calculate D_{OFL}, we multiply the magnetic diffusion coefficient D_M with the field line loss fraction FLLF:

$$D_{OFL} = D_M FLLF \tag{3.4}$$

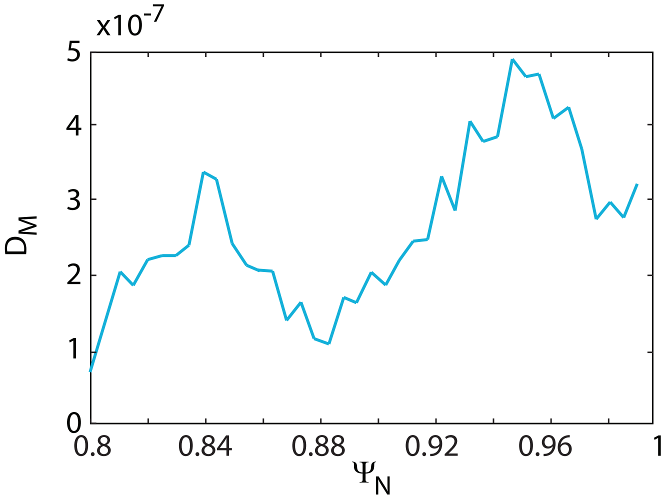

Figure 3.6: Stochastic diffusion coefficient for a low triangularity H-mode discharge on DIII-D.

First, we start from the magnetic diffusion coefficient, D_M:

$$D_M = \frac{1}{N}\sum_{i=1}^{N}\frac{(\Delta r_i)^2}{2L_i}. \tag{3.5}$$

Here N is the number of field lines started on a flux surface, r_i is the radial displacement of the field line and L_i is the total length of the field line. In this thesis, we limit the length of the field line to 200 toroidal turns. If a field line takes longer to leave the plasma, it is very unlikely that it will transport large quantities of particles towards the divertor. While this formula is similar to the one by Yan and Evans [100]. There are two important implementation differences. First, a mistake was found in the calculation of the length of a field line. Yan and Evans did not include the poloidal component of the length. This can lead to an increase of 30% for closed fields lines, because of proximity to the $q = 3$ rational surface. Second, to calculate Δr_i, Yan and Evans use a geometric factor which depends on shape, but is not defined in their paper. To avoid geometric factors which are shape and machine dependent, we map the displacement in Ψ_N to R space at the midplane. Figure 3.6 shows the calculation of D_M for a DIII-D H-mode discharge. When comparing this values of D_M with those from Yan and

Evans [100], we notice that in the region of $\Psi_N \geq 0.9$ the agreement is fairly good. Deeper inside, our values are about a factor 3 smaller. This is the result of the correction in the calculation of the field line length and of mapping the results directly at the midplane, versus using a geometric factor that is independent of radius (the distance between flux surfaces is not a linear function of the major radius).

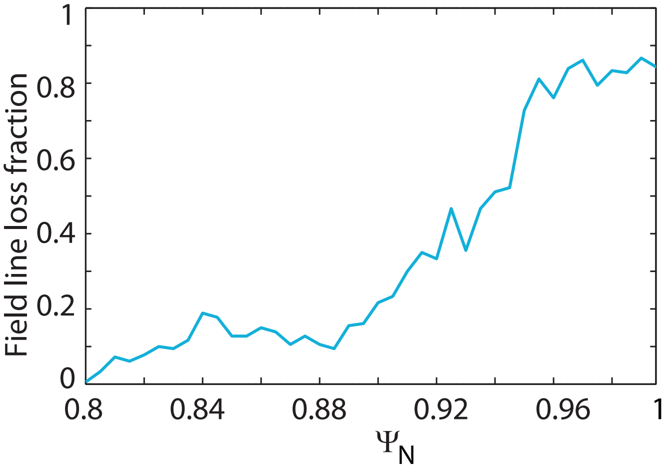

Figure 3.7: Field line loss fraction for a low triangularity H-mode discharge on DIII-D.

Next, we multiply D_M with the field line loss fraction, FLLF:

$$FLLF = \frac{N_{lost}}{N}. \tag{3.6}$$

N is again the number of field lines started on one flux surface and N_{lost} is the number of those field lines that hit a wall before reaching 200 toroidal rotations. Figure 3.7 shows that the amount of field lines that are lost in a vacuum picture due to RMPs is very high close to the seperatrix, but decreases towards zero at $\Psi_N = 0.8$. The field line loss fraction acts as a weighting function for D_M, eliminating large D_M values deeper inside the plasma core, see figure 3.8.

In order to be able to reduce this complicated curve for the weighted magnetic diffusion coefficient to a single number, we calculate the surface between the weighted magnetic diffusion coefficients which includes the $n = 3$ perturbation,

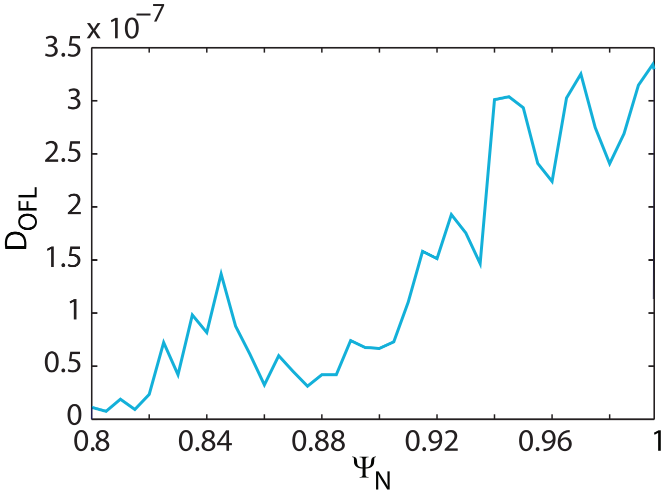

Figure 3.8: Weighted stochastic diffusion coefficient for a low triangularity H-mode discharge on DIII-D.

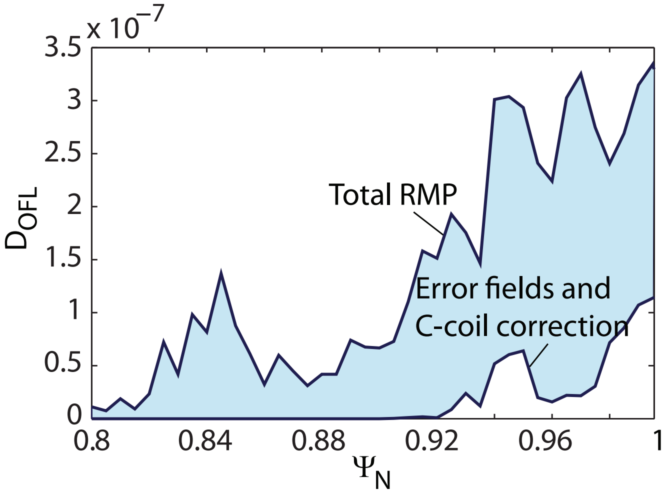

Figure 3.9: Calculation of $\int D_{OFL}$ for a low triangularity H-mode discharge on DIII-D.

error field correction, known error fields, and the weighted magnetic diffusion coefficient of the reference discharge, which only contains the error field correction and the known error fields, see figure 3.9.

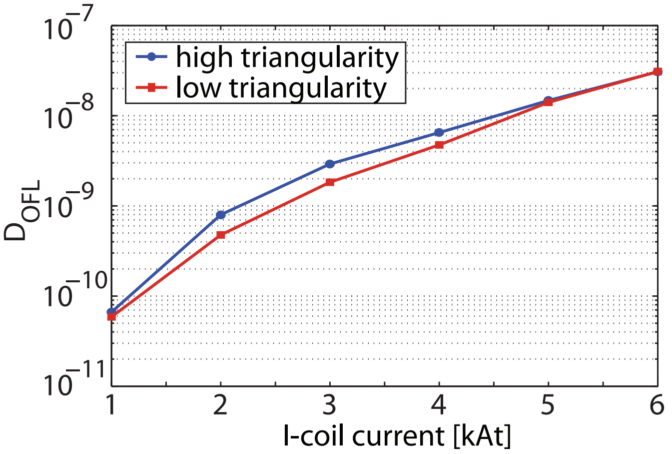

Figure 3.10: Calculation of $\int D_{OFL}$ for 6 different I-coil current values and two DIII-D plasma shapes: low $< \delta >$ and ISS.

3.3.3 Comparison with I-coil current and δb_r

In order to illustrate the strong non-linearity of stochasticity as a result of RMPs, we compare the changes in $\int D_{OFL}$ with the applied $n = 3$ even parity I-coil current (see figure 3.10). In this figure, we started from two low collisionality discharges with different shapes (see figure 3.3). We can observe that D_{OFL} has a strong non-linear dependence on I-coil current. Furthermore, the increase of $\int D_{OFL}$ has not saturated with the maximum possible I-coil current on DIII-D. There is also a small difference between the different shapes, especially at lower I-coil values. A recent publication by Kirk et al. [43] for the MAST spherical tokamak shows an exponential dependence of the density pump-out with I-coil current for a database of similar L-mode discharges.

Figure 3.11 shows that $\int D_{OFL}$ is very non-linear when compared to the radial resonant magnetic component of the perturbative field on the 11/3 surface, $b_r^{11/3}$. Although the calculation of $b_r^{11/3}$ includes the q-profile and shape of the plasma, the two comparisons do not line up. This is the result of the limitations of the linear approximation for b_r, or of the non-resonant components of the field. We conclude that $\int D_OFL$ is a more complete and exact representation of the stochasticity of the magnetic field than b_r. Figure 3.11 clearly shows the strong non-linear behavior perturbative field. This illustrates the limitations of using the

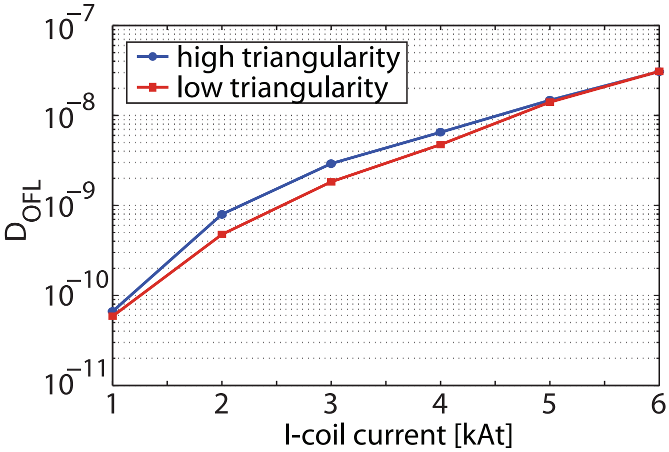

Figure 3.11: Variation of $\int D_{OFL}$ with δb_r for two DIII-D plasma shapes: low $< \delta >$ and ISS.

quasi-linear approach to estimate stochastic transport in the plasma edge.

3.4 Correlation of density pump-out with D_{OFL}

We have now gather the necessary tools to compare the experimental density pump-out due to RMPs with $\int D_{OFL}$. In Figure 3.12, we plot the density pump-out, Δn_e, versus the change in $\int D_{OFL}$ by comparing the density in each RMP discharge to a matching non-RMP reference discharge. For MAST Δn_e is based on the line averaged density; for DIII-D Δn_e is based on the change in electron density at the top of the pedestal. To visualize both datasets on a similar scale, we have multiplied the Δn_e by a factor 10 for MAST. In both cases, there is a linear correlation between the density pump-out, Δn_e and D_{OFL}:

$$y = (0.08 \times 10^8 x - 0.032) \times 10^{19} \tag{3.7}$$

$$y = (0.23 \times 10^8 x + 1) \times 10^{19} \tag{3.8}$$

Equation 3.8 is the linear fit for DIII-D and 3.7 is the linear fit for MAST. The norm of the residual is 0.37×10^{19} for MAST and 0.23×10^{19} for DIII-D.

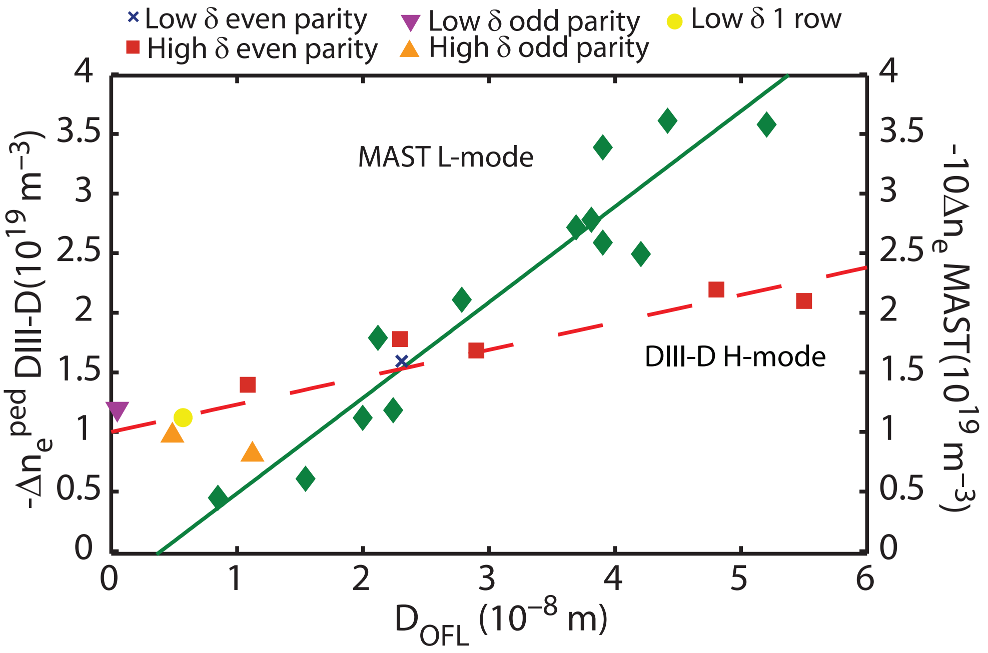

Figure 3.12: Correlation of density pump-out with $\int D_{OFL}$ for DIII-D and MAST plasmas.

3.5 Discussion

If Δn_e were solely due to the increase in stochasticity (without plasma response model), the data for each confinement regime should be a line from (0,0) with a slope of n/D. The slopes should differ by approximately an order of magnitude between L-mode and H-mode due to differences in edge density ($n_e^{ped}/n_e^L \sim 2$) and diffusivity ($D_L/D_H \sim 5$). This is qualitatively consistent with Figure 3.12 if we enforce that the linear regression curve has to go through (0,0). However, neither linear regression curve goes through (0,0) and consequently the difference in slope between both curves is only a factor 3. This is a strong indication that the increase in particle transport might be different for MAST L-modes versus DIII-D H-modes.

The DIII-D H-mode data also show a very large Δn_e at extremely small ΔD_{OFL}; in contrast, a threshold ΔD_{OFL} is needed to achieve density pump-out in the MAST L-modes. We believe that the DIII-D data has a large off-set, which can be explained by:

- transport processes other than stochasticity that are more important (this would alter the y-axis), and
- the plasma response is important (this would alter the x-axis).

The threshold for MAST L-modes might be the result of the high rate of anomalous transport ($D \sim 1m/s^2$) in L-mode that masks transport changes at small $\int D_{OFL}$ until they become significant relative to the background anomalous transport.

3.6 Conclusion

In this chapter we show that there are several theories to explain the density pump-out in RMP discharges. These theories are often based on experimental observations made in one single experimental device with very specific set of plasma conditions.

To be able to compare different experimental conditions and devices, we introduce the calculation of D_{OFL}, a weighed magnetic diffusion coefficient. The calculation of D_{OFL} is performed with a vacuum field line tracing code. We show that in discharges with comparable plasma conditions, the density pump-out is correlated with $\int D_{OFL}$. However, there is a clear difference in pump-out between MAST and DIII-D for similar values of $\int D_{OFL}$. We have to conclude that the density pump-out depends strongly on plasma and machine conditions and that we need to be careful when making theoretical predictions based on only 1 discharge in 1 experimental device.

Chapter 4

Turbulent transport changes in DIII-D and MAST

4.1 Introduction

In the previous chapter we compared the density pump-out in MAST L-mode and DIII-D H-mode discharges. We found that for similar RMP levels, the magnitude in density pump-out differed by nearly an order of magnitude. In this chapter we investigate the changes in turbulence, since they play an important role in understanding particle and heat transport in plasma physics.

Recent work on turbulent heat transport highlights the good agreement and the limitations of theoretical predictions when compared to density and temperature fluctuation measurements in the core of L-mode plasmas in DIII-D [93, 92]. Turbulent particle transport in the core of a Tokamak is driven by micro-instabilities at the ion Larmor radius scale. Typical drive terms for these micro-instabilities are the temperature gradients and the density gradient. This is of direct relevance for the application of RMPs, since one of the main characteristics of RMPs is that they alter the pressure gradient in the pedestal. Therefore, even without apprehending the impact of the complex 3D magnetic field structure on particle transport, the final new plasma equilibrium has altered density and temperature gradients. Consequently, in order to obtain an accurate characterization we need to investigate how the drive and damping terms for turbulence change as a result of RMPs.

Although turbulent transport at the plasma edge is not as well understood as in the core, it plays a critical role in the formation of the H-mode transport barrier [82, 7], also called the pedestal. The formation of a transport barrier is accompanied by an increase in the $E \times B$ shear flow. The $E \times B$ shear flow stretches and distorts the turbulence eddies until they lose their coherence [4]. As a result, the sustainable size of eddies in a strong sheared flow area of the plasma is reduced, strongly diminishing turbulent transport. In chapter 3, we showed that neoclassical modeling of RMPs indicates that the radial electric field, E_r at the edge changes from neoclassical to ambipolar values. This can change the $E \times B$ shear in the pedestal area, which can lead to a change in turbulent transport. Hence, we will investigate the changes in $E \times B$ shear in this chapter.

Additionally, a direct analysis of the changes in fluctuation measurements completes our review of RMP altered turbulent transport. We focus on changes in long-wavelength density ($k_\theta \sim 1\ cm^{-1}$) fluctuations as measured by the beam emission spectroscopy (BES) system in DIII-D [51]. In MAST L-mode discharges we investigate the changes in I_{sat} measured by the reciprocating probe [102].

This analysis of turbulent transport is done for MAST L-mode discharges (section 4.2) as well as DIII-D H-mode discharges (section 4.3). Even without the application of RMP, turbulent transport is significantly different in both confinement regimes. It is therefore not unreasonable that changes in turbulence characteristics by RMPs are distinct to each mode.

4.2 Turbulent transport changes in MAST L-mode plasmas

Systematic turbulent transport measurements in MAST RMP plasmas were performed in connected double-null (CDN) ohmic L-mode discharges [80] (see figure 4.1). These discharges have the following general experimental parameters: $I_p = 400\ kA$, $B_T = 0.52\ T$, $\beta_N \sim 0.7$ and $q_{95} = 6$. Although this q_{95} (see figure

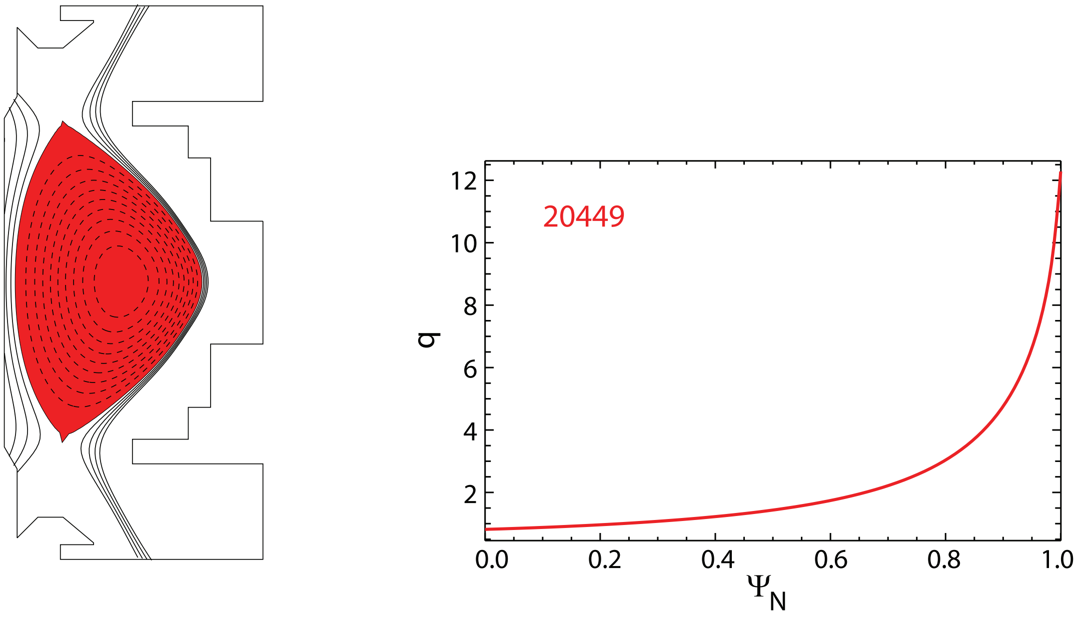

(a) Plasma shape for MAST CDN L-mode discharges.

(b) q profile for MAST CDN L-mode discharges.

Figure 4.1: Shape and q-profile of CDN L-mode RMP discharges in MAST.

4.1b) is far outside what would be considered the resonant window on DIII-D, vacuum modeling with the ERGOS code shows nice alignment of the applied RMP perturbation with the even parity $n = 3$ fazing of the I-coils [43]. The Chirikov island overlap width, $\Delta\Psi_N = 0.1$ is smaller than the DIII-D ELM suppression criterium of $\Delta\Psi_N = 0.165$ [24].

We compare 3 discharges with $0\ kA, 1\ kA$ and $1.4\ kA$ $n = 3$ even parity I-coil current (see the bottom of figure 4.2). In this configuration a clear and repeatable reduction in the line-averaged density is observed, see the top of figure 4.2. While the D_α changes for DIII-D H-mode discharges, investigated in chapter 2, are very distinct, there is no such measurable change in the D_α light in the lower divertor for MAST L-mode discharges. This indicates that divertor conditions remain similar and changes in neutral fueling are minor.

Figure 4.3a shows how the how the drop in line averaged electron density translates to changes in the electron density profile. The electron density measured at 0.4 seconds drops not only at the edge where the perturbation is applied but

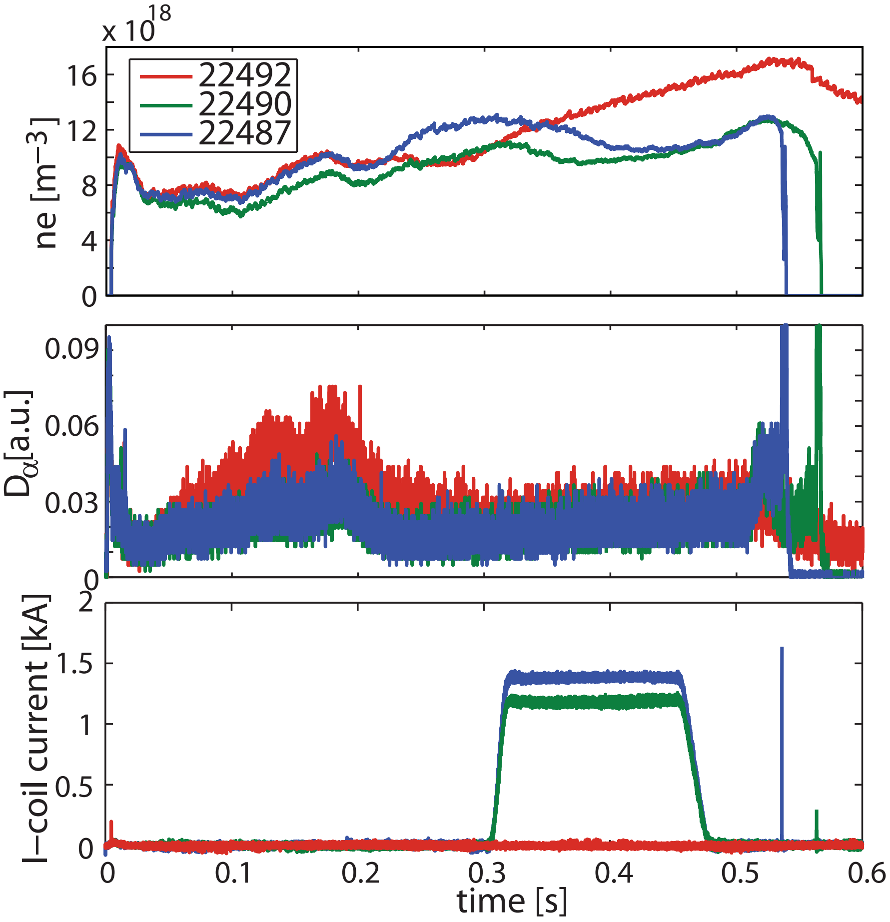

Figure 4.2: Time evolution of the CDN RMP L-mode discharges on MAST.

over the whole profile. The electron temperature profile at the same time shows little change at the edge (see Figure 4.3b). In the core the changes are larger (however, this change is minimal in comparison to changes in density). Changes to the electron temperature profile in the core, should not be over interpreted, especially the hollow profile of discharge 22490 is the result of sawtooth activity, which is unrelated to the application of RMPs in these experiments.

4.2.1 Changes in drive terms

In order to understand turbulent transport changes due to RMPs, we start by investigating the drive terms of turbulent transport. Figure 4.4a show the changes in a/L_n, here a is the minor radius and $L_n = \frac{1}{n}\frac{dn}{dr}$, with n, the electron

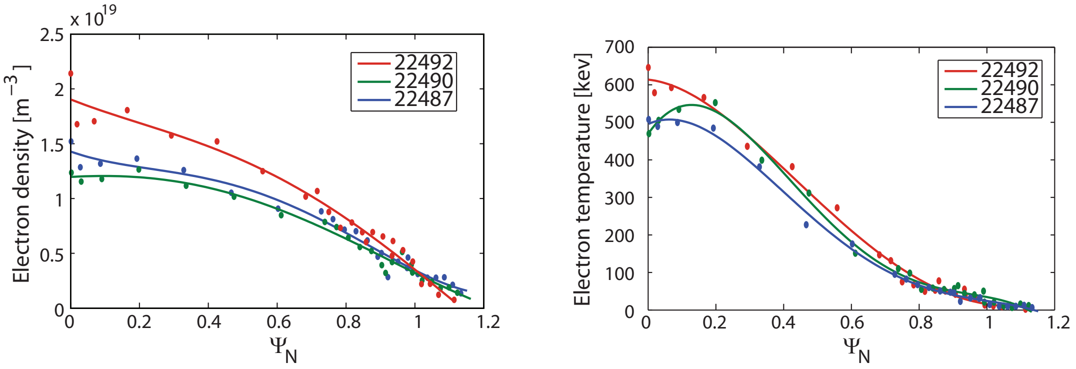

(a) Experimental electron density profile, with 4th order polynomial fit.

(b) Experimental electron temperature profile, with 4th order polynomial fit.

Figure 4.3: Changes in midplane density and temperature profiles as a result of $n = 3$ RMPs in CDN L-mode discharges on MAST.

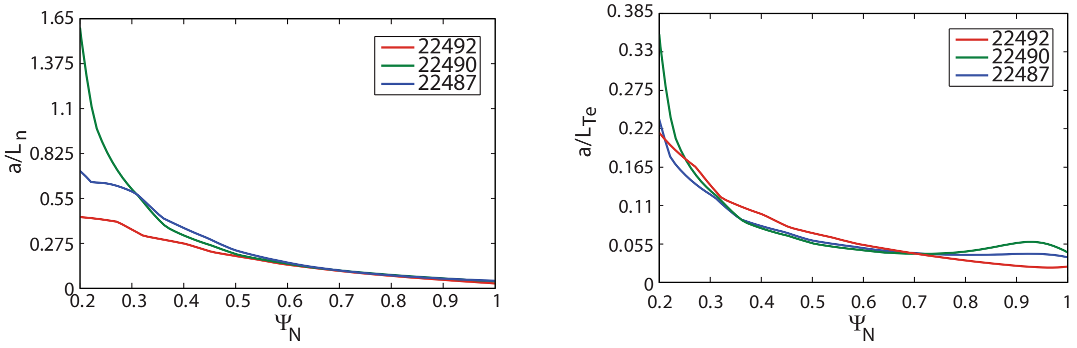

(a) Changes in inverse density scale length, L_n, as a result of RMPs in CDN L-mode discharges in MAST.

(b) Changes in inverse electron temperature scale length, L_{Te}, as a result of RMPs in CDN L-mode discharge in MAST.

Figure 4.4: Changes in inverse scale lengths as a result of RMPs in CDN L-mode discharges in MAST.

density and dn/dr the electron density gradient. While there is no observable change at the plasma edge for the inverse scale length, there are changes in a/L_n in the core as a result of RMPs. However, these changes are not systematic with increasing I-coil current.

a/L_{Te}, with a being the minor radius and $L_{Te} = \frac{1}{T_e}\frac{dT_e}{dr}$, the inverse scale length for the electron temperature, changes at the plasma edge when RMPs are applied. However, again this change is not consistent with increasing coil current (see Figure 4.4b). So it is unclear whether these changes are correlated with the applied RMP and whether they affect turbulent transport in a systematic way.

From this we can conclude that, there is no clear systematic change in inverse scale lengths for these L-mode RMP discharges on MAST.

4.2.2 Changes in fluctuations

Another source that alters turbulent transport is the change in fluctuation levels. Tamain et al. [80] extensively investigate changes in fluctuations in RMP L-mode discharges in MAST with a reciprocating probe, measuring the Ion Saturation current I_{SAT}. Although the discharges in Tamain et al.'s [80] are not the same as the ones discussed in this thesis, their setup is identical and the observations are similar.

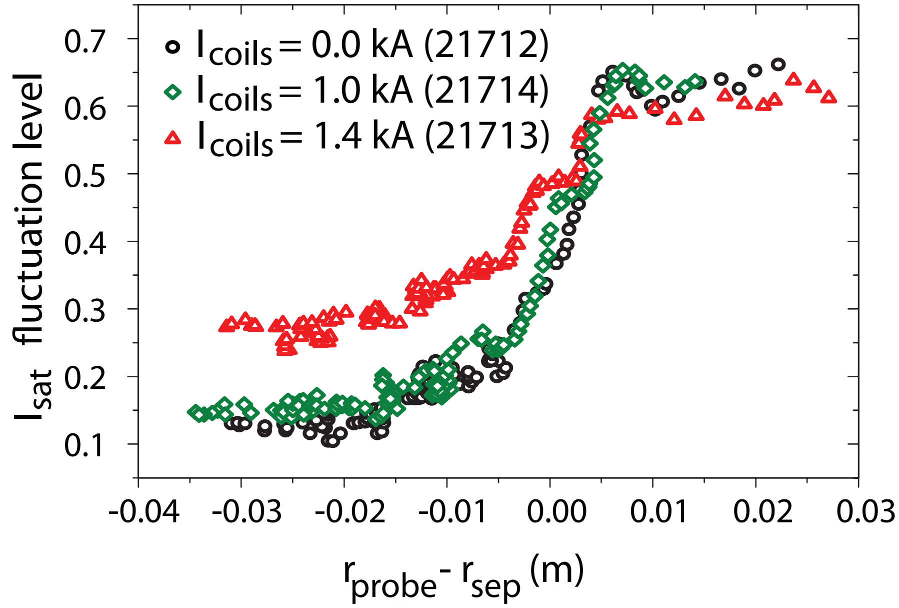

Figure 4.5: Changes in $< I_{SAT} >$ as a result of RMPs in CDN L-mode discharges in MAST [80].

The radial profiles of the $\delta I_{SAT}/ < I_{SAT} >$ (see figure 4.5) from Tamain et al. [80] show that when RMP is applied at the maximum possible current, a 50% increase in the RMS fluctuation level inside the seperatrix is observed, whereas there is no measurable change at 1 kA. Tamain et al. [80] show that the RMS fluctuation levels measured at $r - r_{sep} = -3\ cm$, the innermost measurement point, correlate exponentially with increasing I-coil current. Moreover, the PDFs of the I_{SAT} fluctuations 3 cm inside the separatrix change from a symmetric 'Gaussian-like' distribution to a broader distribution with dominant tails. The probe measures negative skewness on half the pins and positive skewness on the other half inside the seperatrix. This indicates that RMPs are responsible in MAST L-mode discharges for the appearance of intermittency inside the separatrix. The existence of tails in the PDFs of the I_{SAT} fluctuations is generally observed in the SOL in L-mode plasmas. Consequently, Tamain et al. [80] concludes that the turbulent characteristics inside the seperatrix are more intermittent with RMPs and therefore more comparable to the fluctuations generally observed in the SOL. In contrast, measurements taken in the SOL are barely altered by RMPs and exhibit the typical asymmetric shape with a dominant positive tail, indicating strong intermittent behavior.

The changes in I_{SAT} fluctuations presented by Tamain et al. [80] are however not correlated with changes of the inverse scale lengths. Therefore, the increase in fluctuation levels and characteristics can not be explained by a change in drive terms. As a result, the changes in $E \times B$ shear are investigated next.

4.2.3 Changes in $E \times B$ shear

Tamain et al. [80] also discuss the changes in E_r at the plasma edge and observe a reduction of the E_r well inside the seperatrix. S. Mordijck et al. [54] compare the $E \times B$ shearing rate deeper inside the plasma. The radial electric field is measured by Doppler spectroscopy using an outboard Helium gas puff to give a mid-plane edge-localized source of the 468.57 nm He II emission line [52]. The intensity profile is converted to a density profile using the Thomson scattering diagnostic in conjunction with atomic modeling based on the ADAS atomic physics database [1]. Finally by solving the force balance equation, we get the radial electric field and then calculate the $E \times B$ shear, $\omega_{E\times B}$ with formula 3 from [7].

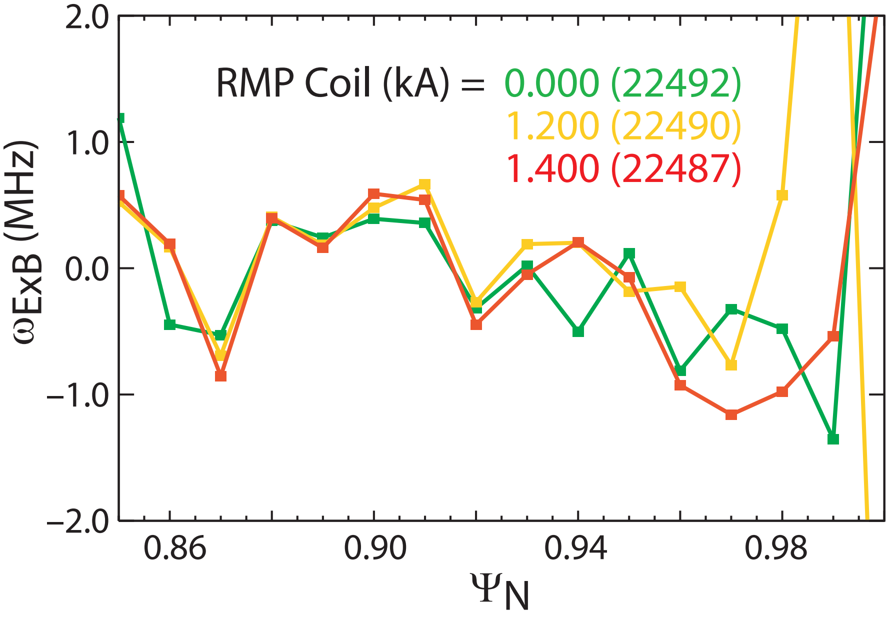

Figure 4.6: Changes in $E \times B$ shearing rate measured with a Helium gas puff in RMP CDN L-mode discharges in MAST.

Figure 4.6 show the $\omega_{E\times B}$ for three discharges: 22492 has no $n = 3$ I-coil current, 22490 has 1 kA and 22487 1.4 kA. The $E \times B$ shear does not change when the RMP-coil is energized for measurement with the Doppler spectroscopy. However, probe measurements of E_r show a clear change for $\Psi_N > 0.92$ [80]. For $\Psi_N < 0.92$ both diagnostics agree that $\omega_{E\times B}$ does not change when RMP is applied.

4.2.4 Summary of MAST turbulence results

To summarize, we find that the inverse scale lengths in MAST do change with the application of RMPs. However, we were unable to find a systematic correlation with increasing I-coil current. In contrast, the RMS value of the fluctuations increases inside the seperatrix and the increases is exponentially correlated with the applied I-coil current. Moreover, the fluctuations change character and show a more intermittent behavior. The E_r well becomes less deep inside the seperatrix, but measurements of the $E \times B$ shear deeper in the plasma remain constant.

4.3 Turbulent transport changes in DIII-D H-mode plasmas

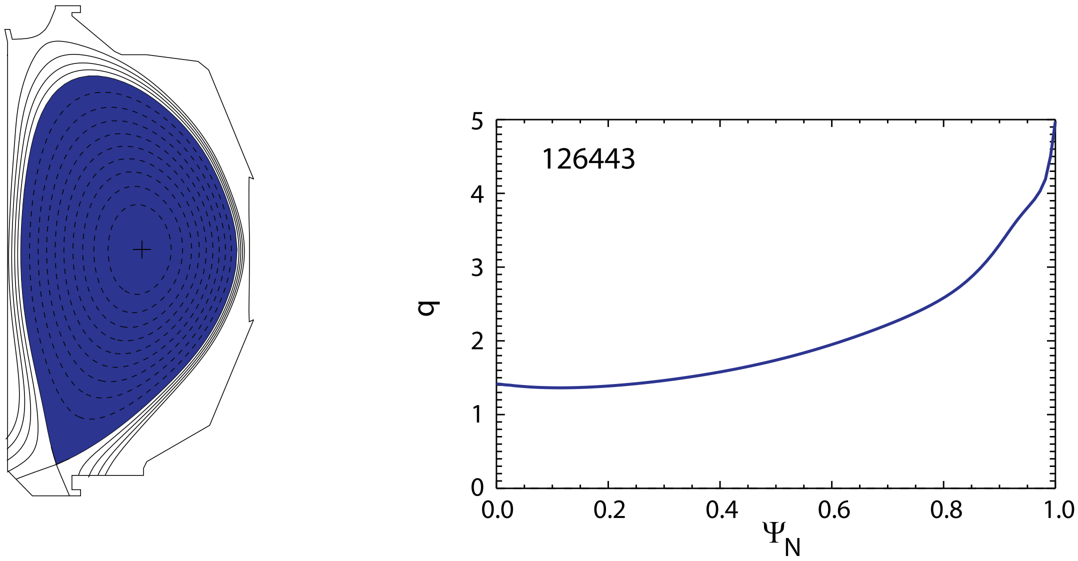

(a) ITER Similar Shape in DIII-D RMP H-mode discharges.

(b) Kinetic q-profile for ITER Similar Shape H-mode discharges in DIII-D.

Figure 4.7: Experimental equilibrium conditions for ISS discharges in DIII-D.

In this section we look at three important aspects that give an indication as to how turbulent particle transport changes in DIII-D RMP H-mode plasmas. We compare the changes in turbulence characteristics in a set of low collisionality H-mode discharges, $\nu^* \leq 0.2$ in the ITER similar shape (ISS) [18] (see figure 4.7). The discharges have an average triangularity of $< \delta >\sim 0.53$, $I_p = 1.68\ MA$, $B_T = 2.1\ T$, $\beta_N \sim 2.0$ and $q_{95} = 3.6$.

In a series of 5 discharges, the I-coil current is varied from 4 kA to 6.3 kA $n = 3$ even parity. The final discharge of the series is a reference discharge without the application of the I-coil. The I-coil is applied before a steady state condition in H-mode is achieved (see Figure 4.8). The first graph in figure 4.8 shows the line-averaged density. The I-coil is turned on at 1800ms (4th from the top in figure 4.8), nearly no change is observed in the temperatures (2nd and 3rd graphs). The

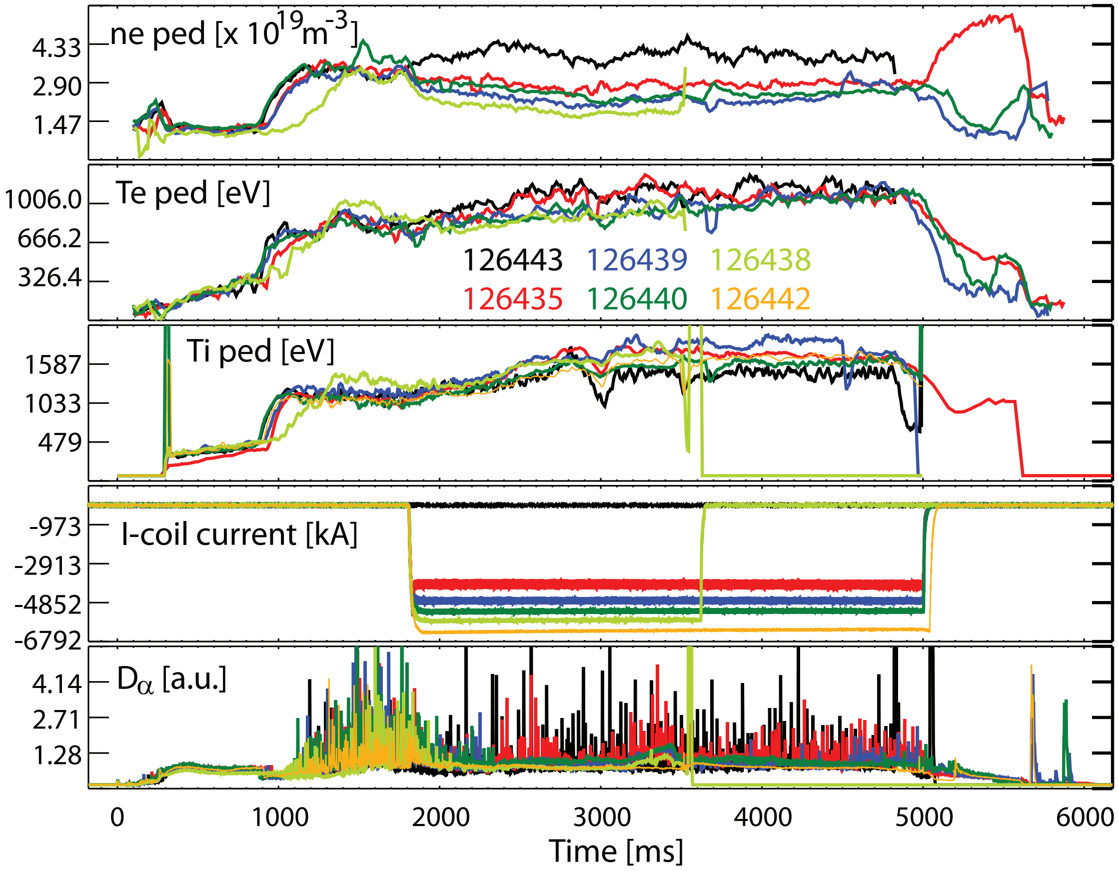

Figure 4.8: Time evolution of the ISS RMP H-mode discharges in DIII-D.

bottom plot of figure 4.8 is the D_α light close to the outer strike-point in the lower divertor. A density pump-out is observed and with exception at the lowest applied I-coil current, ELMs are suppressed.

The density profile is not only reduced in the pedestal area, but drops over the whole profile (see figure 4.9. The density at the top of the pedestal ($\Psi_N \sim 0.9$) is very similar for most of the RMP discharges, with exception of discharge 126435, which is not ELM suppressed, because the I-coil current was at its lowest for this set of discharges. The discharge with the highest I-coil current (126442 at 6.3 kA) peaks at the inner most radius. One more discharge is peaking in the core, however, since it does not have the second highest I-coil current, it is unclear if this peaking is related to the I-coil current magnitude, or to some other unrelated event in the plasma.

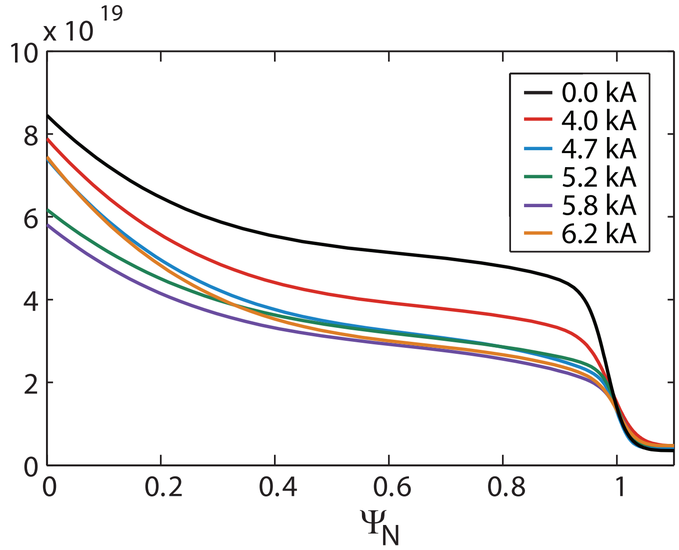

Figure 4.9: Changes in midplane density profiles as a result of $n = 3$ RMPs in ISS H-mode discharges in DIII-D.

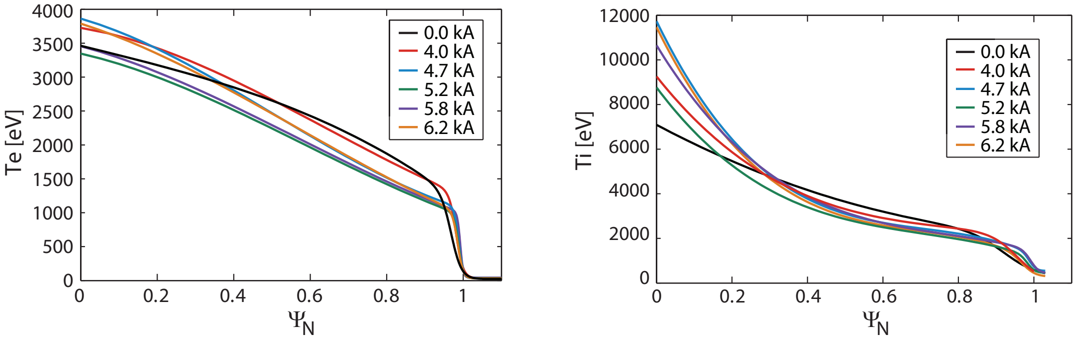

(a) Experimental *tanh* electron temperature profiles fits.

(b) Experimental *tanh* ion temperature profile fits.

Figure 4.10: Changes in midplane temperature profiles as a result of $n = 3$ RMPs in ISS H-mode discharges in DIII-D.

The electron temperature profile is reduced at the top of the pedestal for all ELM suppressed discharges (see figure 4.10a). However close to the magnetic axis all RMP discharges are at a similar or higher electron temperature as the reference ELMing H-mode discharge without RMP. Contrary, the ion temperature at the plasma edge remains fairly constant, with the slight difference that the pedestal becomes narrower (see figure 4.10b). In the core all RMP discharges show a peaked ion temperature profile.

4.3.1 Changes in drive terms

In the previous section we showed that RMPs do not only affect the plasma edge, but also change the density and temperature profiles deeper inside the plasma. This new equilibrium state changes the drive terms for turbulence. To understand how the drives for turbulence change we calculate the inverse scale lengths from the experimental *tanh* fits to the density and temperature profiles at 3000 ms. For the ELMing discharges, the data is chosen in the $80 - 99\%$ percent of the ELM cycle over a steady state period of $\sim 500\ ms$. For the ELM free discharges, a 100 ms time window is sufficient.

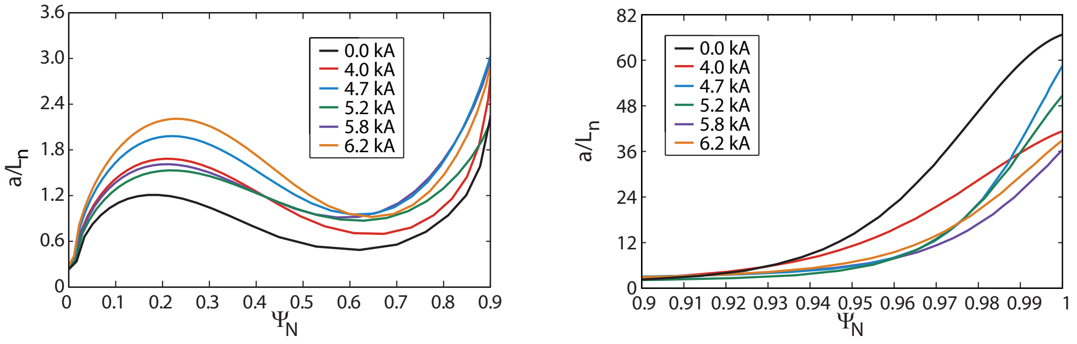

(a) Density gradient drive term in the core.

(b) Density gradient drive term at the plasma edge.

Figure 4.11: Changes in **electron density** gradient drive term profile as a result of different I-coil currents.

Figure 4.11a shows that a/L_n increases from $\Psi_N = 0 - 0.9$ when RMP is applied. Whereas from $\Psi_N = 0.9 - 1$ this inverse scale length is reduced when the I-coil is applied, see Figure 4.11b. We can observe a minor difference in how a/L_n is reduced depending on the applied I-coil current. At the lowest applied current, ELMs are not suppressed and from $\Psi_N = 0.92 - 0.98$, a/L_n is larger than for all the other ELM suppressed discharges. This change is minimal and more data is needed to verify this effect and its significance.

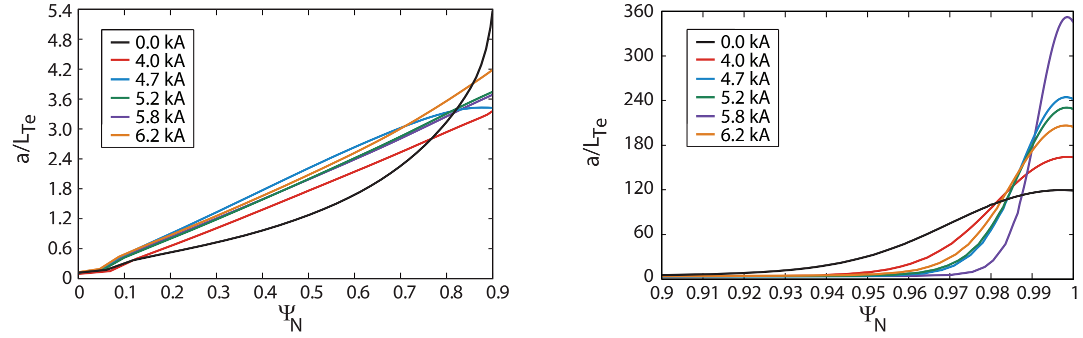

(a) Electron temperature gradient drive term in the core.

(b) Electron temperature gradient drive term at the plasma edge.

Figure 4.12: Changes in **electron temperature** gradient drive term profile as a result of different I-coil currents.

Figure 4.12a shows that a/L_{Te} increases slightly in the core, but the increase is independent of the magnitude of the applied RMP. More interestingly, the profile of a/L_{Te} changes from being exponential without any RMP to linear when RMP is applied. At the plasma edge ($\Psi_N = 0.9 - 1$), the changes are more complex (see Figure 4.12b). The global trends are that the a/L_{Te} profile narrows, and the peak of the inverse scale length does not correlate with the applied I-coil current. It is not clear why discharge 126438, where 5.8 kA is applied, has a significantly higher peak in a/L_{Te} than the other discharges and this warrants further research.

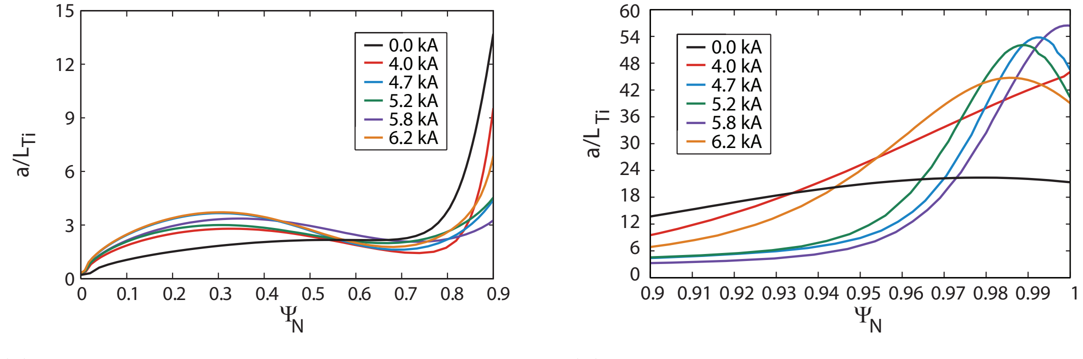

(a) Ion temperature gradient drive term in the core.

(b) Ion temperature gradient drive term at the plasma edge.

Figure 4.13: Changes in **ion temperature** gradient drive term profile as a result of different I-coil currents.

In figure 4.13a, a/L_{Ti} (a being the minor radius and $L_{Ti} = \frac{1}{T_i}\frac{dT_i}{dr}$ with T_i the ion temperature) increases up to $\Psi_N = 0.5$, while decreasing from $\Psi_N = 0.5 - 0.9$. From figure 4.13b, we can see that a/L_{Ti} initially increases close to $\Psi_N = 1$, until a peak is reached. The location and magnitude of this peak moves to lower Ψ_N values and decreases with increasing I-coil current, thus increasing the a/L_{Ti} profile width. Discharge 126435, where 4 kA of I-coil current is applied and ELMs are not yet suppressed does not show the peak of the ELM suppressed discharges. More experimental discharges are needed to understand the different a/L_{Ti} profiles at the plasma edge as a result of RMPs. This will assist in separating out whether changes are the result of ELM suppression or the application of RMPs.

4.3.2 Changes in fluctuations

Previous work on characterizing changes in density fluctuation levels as a result of RMPs in DIII-D H-modes focused on core plasma changes or concentrated on line integrated measurements and not localized measurements [101, 57]. In contrast, in this thesis we will focus on localized measurements at the plasma edge of DIII-D H-mode plasmas.

The localized core measurements are done with the Beam Emission Spectroscopy (BES), a high-sensitivity, good spatial resolution imaging diagnostic system [51]. BES observes collisionally-induced, Doppler-shifted D_α fluorescence ($\lambda = 652 - 655\ nm$) of injected deuterium neutral beam atoms. The diagnostic is capable of long wavelength ($k_\perp \rho_I < 1$) density fluctuations. A recent publication by Yan et al. [101] shows that core turbulence increases dramatically as a direct consequence of RMP application to suppress ELMs. Measurements taken at three radial locations $\rho = 0.68, 0.85$ and 0.96 show a substantial increase in fluctuation power at the inner locations, whereas the outer location mostly shows a change in spectral shape and nearly no increase in fluctuation amplitude. Yan et al. [101] also shows that the response time of fluctuation changes at different radial locations to I-coil current changes in an ELM suppressed plasma. At $r/a = 0.85$ the response is almost instantaneous, essentially tracking the I-coil current. Deeper at $r/a = 0.7$ the response decay time is 20 ms and at the most inner measurement location $r/a = 0.58$ the decay time is 40 ms. Although the density profile changes with $5-10\%$during the changes in I-coil current, the variation is less. The changes in density gradient cannot explain the rapid temporal turbulence response in this paper.

Prior reported non-local measurements with the FIR coherent scattering diagnostic show an increase in density fluctuation, $\tilde{n}$ with poloidal wavenumbers $k_\theta = 1 \pm 1cm^{-1}$ [57]. This increase in density fluctuations is the result of an increase in coherent mode activity as well as increases in broadband fluctuations levels. In Moyer et al. [57], localized measurements at $\Psi_N = 0.98$ show a change in fluctuation character and overall amplitudes. The authors conclude that the changes in $\tilde{n}$ result in an increase in particle convection either due to changes in ion scale drift wave turbulence or convective cells, which leads to the observed changes in particle balance.

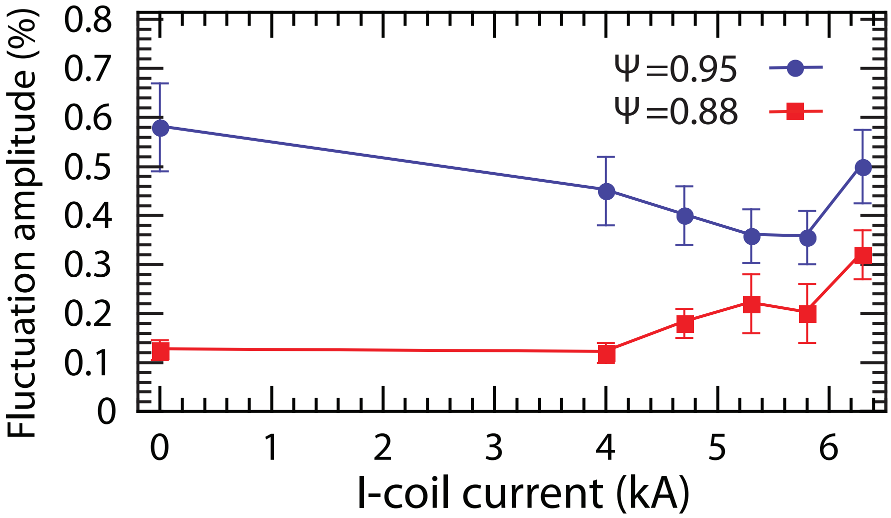

Figure 4.14: Changes in density fluctuations at two radial locations, $\Psi_N = 0.88$, at the top of the pedestal and $\Psi_N = 0.95$, inside the pedestal, as a result varying $n = 3$ I-coil amplitudes.

In this thesis we focus on transport changes in the pedestal area. For the series of discharges in section 4.3 we investigate the changes in long wavelength density fluctuations as measured by BES at $\Psi_N = 0.88$ and 0.95. In contrast to the results deeper in the plasma core, $\tilde{n}/n$ fluctuations increase moderately at $\Psi_N = 0.88$ and decrease at $\Psi_N = 0.95$, see Figure 4.14. At the most outer measurement location, the density fluctuations increase again at 6.3 kA I-coil current, but they are still lower than those for the reference ELMing H-mode.

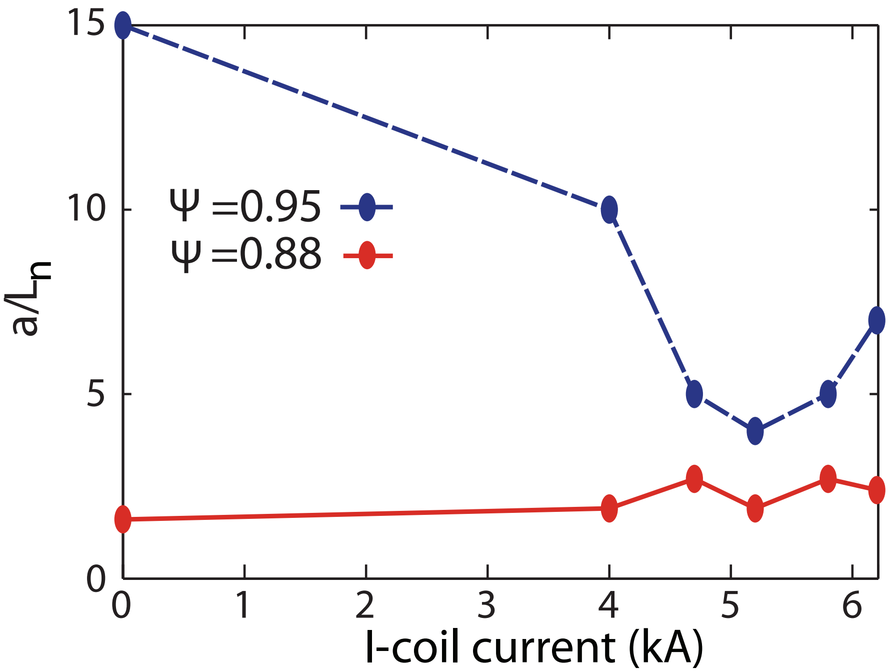

Figure 4.15: Changes in inverse scale length a/L_n at two radial locations, $\Psi_N = 0.88$, at the top of the pedestal and $\Psi_N = 0.95$, inside the pedestal, as a result of varying $n = 3$ I-coil amplitudes.

When we compare the changes in density fluctuations, $\tilde{n}/n$, with the changes in the inverse scale length, a/L_n, at the same $\Psi_N = 0.88$ and 0.95 locations, we observe a similar behavior (see figure 4.14 and 4.15). At $\Psi_N = 0.95$, the density fluctuations and the a/L_n curves follow exactly the same trend. At $\Psi_N = 0.88$, a/L_n does not increase as pronounced as the fluctuations. We can conclude that turbulence levels and the density gradient follow a similar pattern, but to be more conclusive linear growth rates and frequencies need to be calculated and compared to a more extensive set of turbulence diagnostics, which have recently become available.

4.3.3 Changes in $E \times B$ shear

One final aspect of turbulent transport is the influence of the $E \times B$ shear on the suppression of turbulent transport. Research in the formation of transport barriers has shown the importance of the $E \times B$ shear, $\omega_{E\times B}$ to reduce the turbulent particle transport [82, 7, 4]. The changes in drive terms and fluctuations are therefore not enough to address the changes in turbulent transport. In this section we compare the changes in radial profiles of $\omega_{E\times B}$ in function of different applied RMP I-coil currents for the same DIII-D ISS H-modes.

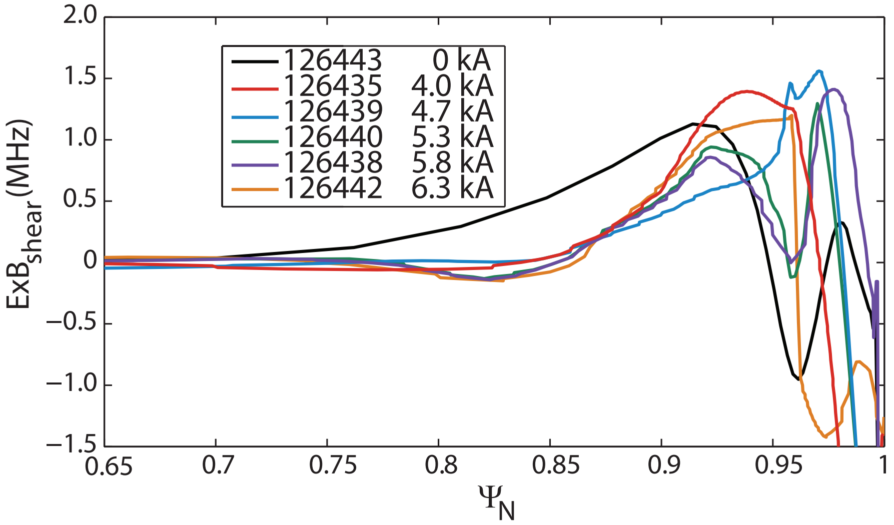

Figure 4.16: Changes in $E \times B$ shear at the plasma edge in DIII-D ISS H-mode discharges with different I-coil current magnitudes.

Figure 4.16 shows the changes in $E \times B$ shear from $\Psi_N = 0.7 - 1$. Independently of the applied I-coil current, the $E \times B$ shear is strongly reduced from $\Psi_N = 0.7 - 0.9$. For $\Psi_N > 0.9$ the results are less clear. In this area, the results depend strongly on the experimental fits to the data. A *tanh* fit to the pedestal is used, based on averaged Thomson scattering and CER data. For ELM suppressed discharges a 100ms time window around 3 seconds is chosen, whereas for ELMing discharges this window is expanded to 500ms. Only the data points that are taken in the $80 - 99\%$ of the ELM cycle are included in determining the best *tanh* fit.

When we compare the changes in $E \times B$ at the same location as the density

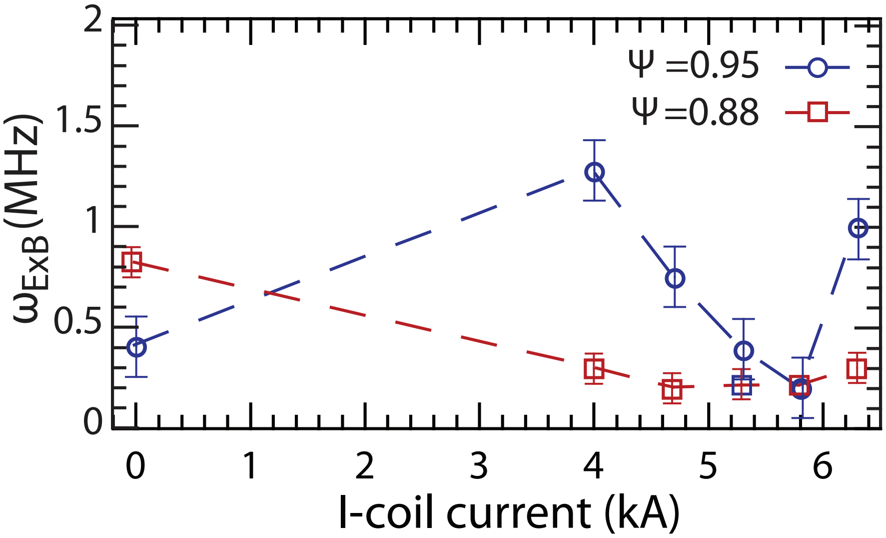

Figure 4.17: Changes in $E \times B$ shear at two radial locations in DIII-D ISS H-mode discharges versus different I-coil current magnitudes.

fluctuations, we find that the changes in $E \times B$ shear do not correlate with the changes in density fluctuations. Where at $\Psi_N = 0.88$ there is a clear reduction in the $\omega_{E\times B}$, nearly independent of the magnitude of the I-coil current (see figure 4.17), the fluctuations increase gradually with increasing I-coil current (see figure 4.14). At $\Psi_N = 0.95$, the fluctuations decrease (see figure 4.14), with increasing I-coil current, however the $\omega_{E\times B}$, does not show this same trend (see figure 4.17).

When comparing the changes in the inverse ion temperature scale length (see Figure 4.13), there is a reduction in a/L_{Ti} from $\Psi_N = 0.7 - 0.9$, which contributes to the reduction in $\omega_{E\times B}$. The other contributions to the $E \times B$ shear are from the poloidal and toroidal plasma rotation. In DIII-D, we can only measure the toroidal and poloidal carbon rotation with CER. This is not a direct representation of the plasma rotation and as a result we need to be careful with the interpretation. The poloidal carbon rotation does not show any variation with variations in I-coil current (see figure 4.18), whereas the toroidal carbon rotation decreases slightly in the plasma core upto $\Psi_N = 0.8$ (see 4.19a). From $\Psi_N = 0.9$, the toroidal carbon rotation increases (see figure 4.19b). We can conclude that the large reduction in $E \times B$ shear from $\Psi = 0.7 - 0.9$ is the mostly result of a

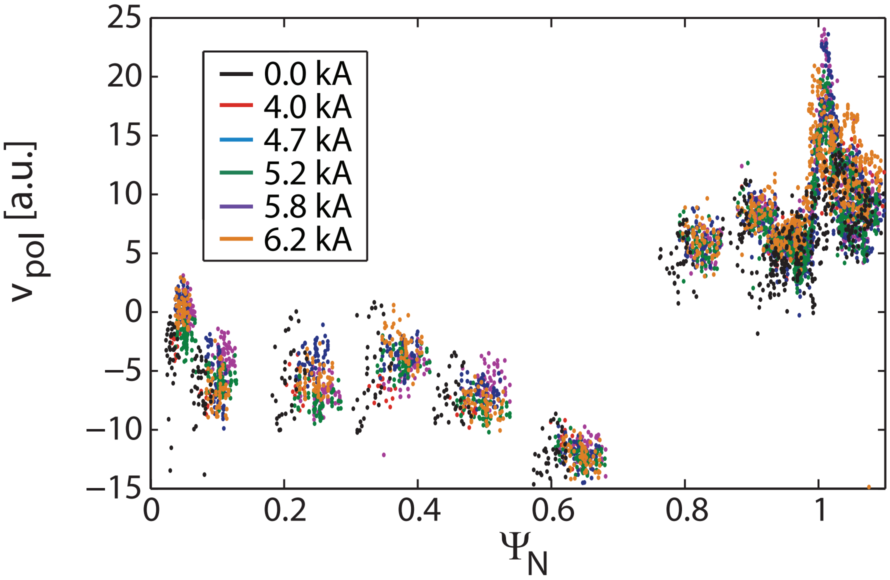

Figure 4.18: Changes in poloidal carbon rotation profiles in DIII-D ISS H-mode discharges due to different I-coil currents.

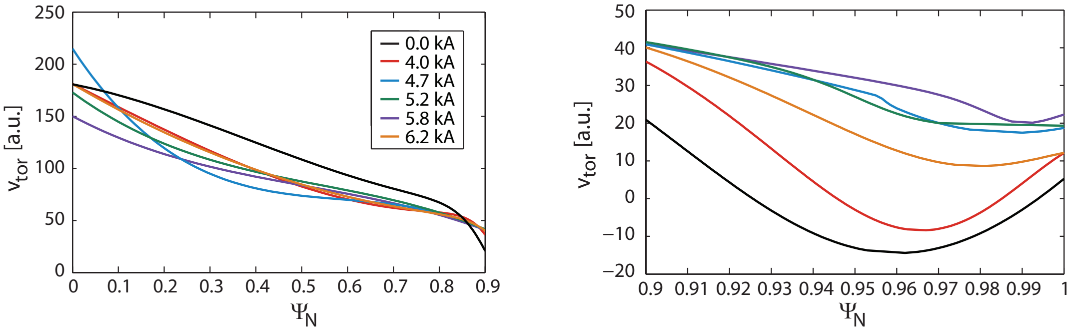

(a) Toroidal carbon rotation from $\Psi_N = 0 - 0.9$ for different magnitudes of the I-coil current.

(b) Toroidal carbon rotation at the plasma edge.

Figure 4.19: Changes in **toroidal carbon rotation** profile as a result of different I-coil currents.

reduction in the ion temperature gradient.

4.3.4 Summary of DIII-D turbulence results

In section 4.3 we discuss the changes in drive terms, long wave-length density fluctuations and $E \times B$ shear for DIII-D ISS H-mode discharges with different $n = 3$ I-coil current magnitudes. We find that the $E \times B$ shear decreases from $\Psi_N = 0.7 - 0.9$, independent of the magnitude of the I-coil current. In this same region, the density fluctuations increase, with increasing I-coil current, whereas changes in a/L_n are minimal. In the pedestal at $\Psi_N = 0.95$, the density fluctuations decrease, with increasing I-coil current, with exception of the discharge at 6.3 kA. The inverse density scale length exhibits the exact same trend. In contrast, the $E \times B$ shear does not change consistently with increasing I-coil current.

4.4 Discussion

These results on the change in turbulent transport characteristics give a first indication as to how RMPs affect turbulent transport. At a first glance (see table 4.1), the changes in turbulent transport are different for MAST L-modes than for DIII-D H-modes.

Table 4.1: Summary of turbulence characteristic for MAST L-mode and DIII-D H-mode as a result of RMPs.

	Core		**Edge**	
	MAST	DIII-D	MAST	DIII-D
a/L_n	no trend	**increases**	no trend	**decreases**
$E \times B$	**no change**	**decreases**	**decreases**	no trend
fluctuations	**increases**	**increases**	**increases**	**decreases**

In MAST L-modes, there is clear increase in the fluctuation levels everywhere inside the seperatrix, whereas in DIII-D H-modes, an increase is only observed deeper in the core (see table 4.1). At $\Psi_N = 0.88$, $\tilde{n}/n$ rises and at $\Psi_N = 0.95$, $\tilde{n}/n$ decreases. Contrary, in MAST L-modes the fluctuation levels increase and are correlated with increasing in RMP levels [80].

Another difference between both experiments is the behavior of the $E \times B$ shear. In DIII-D, the $E \times B$ shear decreases from $\Psi_N = 0.7 - 0.9$ (independently of the I-coil amplitude), whereas in MAST, the $E \times B$ shear deeper inside the plasma does not change (see table 4.1).

In MAST L-modes, the drive terms are similar and do not indicate a clear trend with increasing I-coil current. However, in DIII-D H-modes, the inverse density scale length decreases at the edge and correlates with changes in fluctuation levels at $\Psi_N = 0.95$. We can conclude that even though on MAST previous work shows that the increase in fluctuations is directly correlated to the density pump-out [43, 80], this explanation cannot be extended to the plasma edge in DIII-D H-modes.

In DIII-D, all experimental available data indicates that there is an increase in turbulent transport deeper in the core, but a reduction at the plasma edge [101, 54] is observed. However, turbulent transport does not only depend on long wave-length density fluctuation, but also on potential fluctuations and the cross phase between these two [82, 56]. Moyer et al. [56] showed that while potential fluctuations increase after the H-mode transition, the cross phase between potential and density fluctuations changes. This phase change ends up being more important, due to the strong reduction in particle transport in H-mode. Unfortunately, this measurement is not available inside the pedestal of beam heated type-I ELMing H-mode plasmas, so we can only base our conclusions on the dataset presented in this thesis.

4.5 Conclusion

Experimental measurements show a clear increase in fluctuations and an increase in $E \times B$ shear at the plasma edge in MAST L-mode as a result of a $n = 3$ RMP perturbation. This increase in fluctuations is correlated with the density pump-out [43, 80]. This indicates that RMPs increase the turbulent particle transport in MAST L-mode discharges. Recent fluid modeling confirms that for these L-mode plasmas the anomalous transport coefficients need to increase to explain the density pump-out; the effective stochastic particle transport is too small [69].

For DIII-D, the story is more complicated. Deeper in the core, fluctuation levels increase and there is a drop in the $E \times B$ shear. Also the changes in $\tilde{n}/n$ follow closely the changes in a/L_n. However, the changes in turbulent transport characteristics in the pedestal area are more complex. Due to the limitations of the *tanh* fit to the data, it is not possible to define a clear trend in changes to $E \times B$. Previous results show a decrease of the E_r H-mode well. Fluctuation levels decrease in the pedestal area, with a/L_n following a similar trend at the same radial location. So from the dataset presented in this thesis, we can conclude that turbulent particle transport does not increase in the pedestal area as a result of $n = 3$ RMP application. Therefore, we need to investigate other transport mechanism to explain the changes in density pedestal profile in DIII-D H-mode plasmas.

Chapter 5

Increased convective parallel particle transport due to RMPs

5.1 Introduction

In this chapter, we investigate whether convection parallel to magnetic field due to RMP leads to the experimentally observed density pump-out. This hypothesis is only valid for cases, where the connection length of the open field lines is shorter than the Kolmogorov length (i.e. laminar zone). Previous experimental work on TORE-SUPRA [31], TEXTOR [40] and LHD [44] show that the creation of open field lines with a connection length shorter than the Kolmogorov length (see section 3.1.1) is important to explain the changes in particle and heat fluxes towards the divertor. To simulate this complex effect, we use SOLPS5 [72]: a 2D fluid code B2 [67], coupled to a Monte Carlo neutral code EIRENE [67]. With this code package, we first identify the radial varying effective transport coefficients by matching to the experimental pedestal profiles for a reference ELMing H-mode, without perturbations from the I-coils, similar to the work in chapter 2. Next we calculate the enhanced particle transport resulting from the RMPs. In the vacuum limit, the RMPs create a stochastic field inside the separatrix and open previously closed field lines. These field lines penetrate inside the last closed flux surface (LCFS) and connect to the top of the pedestal allowing electrons to leave as a result of convective parallel particle transport along the magnetic field. TRIP3D [100], a vacuum magnetic field line tracing code, calculates the change in the edge magnetic topology. This new magnetic topology is used to calculate an increase in the radial particle diffusion coefficient. Finally, we add the magnetically induced convective parallel particle transport to the effective transport coefficients from the ELMing H-mode and recalculate the pedestal profiles. The numerical results are compared to experimental RMP H-mode results. Our simulations show that this increase in the free-streaming component of the transport results in midplane density pedestal profiles that are in good agreement with measured profiles during the RMP pulses. Finally, we discuss the results in terms of the physics included in our model and other physics effects that can influence our results but are not yet included in our model.

5.2 Experimental Setup

RMPs successfully suppress ELMs in different plasma scenarios, where several plasma parameters are varied. We are limiting the discussion to low collisionality DIII-D H-mode discharges where $\nu* = q_{95} R \epsilon^{-3/2} \lambda_e^{-1} \approx 0.05$. Here, R is the major radius, $\epsilon(\equiv a/R)$ is the inverse aspect ratio, a is the minor radius and $\lambda_e(= v_{T_e} \tau_e)$, the product of electron thermal velocity v_{T_e} and collision time τ_e) is the mean free path for electron collisions. We consider two distinct sets of experiments, where shape is the major variable, as shown in figure 5.1. First there is discharge 123302, which is a lower single null discharge at low triangularity ($< \delta > \sim 0.25$). In this discharge the outer strike point is close to the pump entrance in the old divertor geometry increasing pumping capability and therefore at low collisionality. The second scenario (discharge 126443) is the ITER similar shape (ISS), which is at higher triangularity, namely $< \delta > \sim 0.53$. Here the ITER shape is modified to allow for better pumping of the outer strike point.

For each of these two scenarios there is a so-called reference ELMing H-mode. This is a normal H-mode with type-I ELMs without any I-coil magnetic perturbations, but with the external C-coils configured for $n = 1$ (toroidal mode

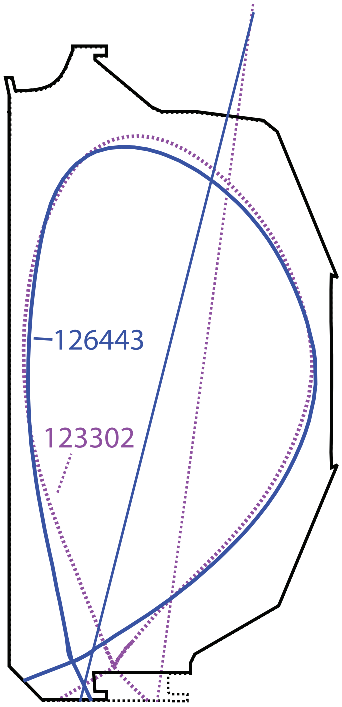

Figure 5.1: Low triangularity and ITER Similar (ISS) experimental shapes.

number) field-error correction. The only difference for the RMP H-mode is that the I-coils are activated in $n = 3$ even parity (upper and lower coils at the same toroidal location have the same currents with a perturbation strength of about $\delta B_r \sim 10^{-4}$Tesla at Ψ_N of 0.95) with a 60 degree phasing configuration [14]. As a result, ELMs are suppressed creating an ELM-suppressed RMP H-mode instead of an ELMing H-mode. In this thesis, for simplicity, we call the one RMP experiment without ELM suppression still an RMP H-mode to distinguish it from the ELMing H-modes without applied $n = 3$ I-coil field. Depending on exact plasma parameters such as shape [15], β_N (normalized plasma pressure) [24], q_{95}[25] (q at the 95% normalized Ψ surface) and the strength and topology of the perturbation [25], ELMs are suppressed.

Three different RMP H-modes are modeled. The first is an RMP H-mode for the low triangularity scenario. In this case, the I-coils have a current of $\sim 3\ kA$ and are initialized 2000 ms into the experiment. Figure 5.2 shows that the size of

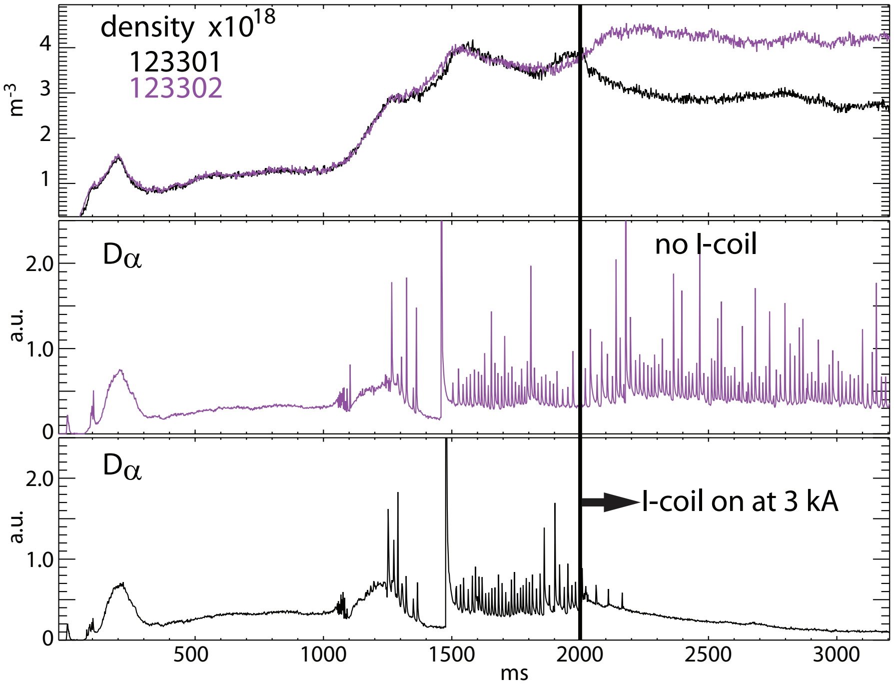

Figure 5.2: Time evolution of two low $< \delta >$ discharges. One reference discharge (without $n = 3$ RMP), 123302, and one $n = 3$ RMP ELM suppressed discharge, 123301.

the ELMs decreases and after 200 *ms* the ELMs are suppressed compared to the reference ELMing H-mode. At the same time, a density pump-out occurs (figure 5.2).

The density pump-out alters the pedestal density profile, shown in figure 5.3. The density drops at the top of the pedestal and over the whole core region. The profile data for the ELMing H-mode, discharge 123302, is obtained by averaging between ELMs over a period of 400 *ms* from 2600 *ms* to 3000 *ms*. Only Thomson scattering data points in the 80%–99% of the ELM cycle are taken into consideration. Next a *tanh* curve is fitted to the experimental data. For the RMP H-mode, the Thomson scattering data is simply taken over a period of 100 *ms* (from 2600 *ms* to 2700 *ms*), since this part of the discharge contains no ELMs that affect the density profile, thus more Thomson scattering points are available. Again, a *tanh* curve is fitted to the experimental data. The slope in the pedestal region for the *tanh* fit of the RMP H-mode is less steep than for the ELMing H-

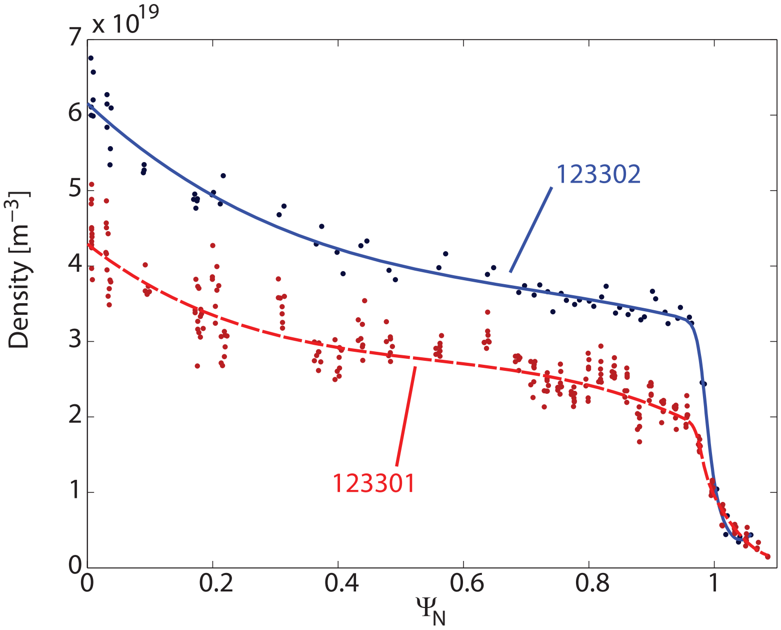

Figure 5.3: Experimental midplane electron density profile in low triangularity discharges. The points are from the Thomson scattering diagnostic and the curves are the *tanh* fits to the data. Discharge 123302 is the reference ELMing H-mode and discharge 123301 is the RMP H-mode.

mode. Chapter 2 shows that this is due to a change in transport and not just a result of a change in particle balance due to altered wall conditions or pumping efficiency [18, 53].

For the ISS shape a similar behavior in the pedestal changes is observed. In this scenario, the I-coil perturbation is initialized at 1800 ms as illustrated in figure 5.4. In this figure, we observe that the density of the reference ELMing H-mode keeps on rising. Whereas, during the RMP pulse (discharge 126435) with 4 kA currents in the I-coils the density curve remains flat. In this case, the ELMs are not fully suppressed, but they are smaller in size and their frequency has increased. This behavior is referred to as ELM mitigation. When the current in the I-coils is increased to 6.3 kA, the line averaged density drops a little further and the ELMs are suppressed. We obtain *tanh* fits similarly as for the low triangularity shape, explained in the previous paragraph (figure 5.5). We again observe that the

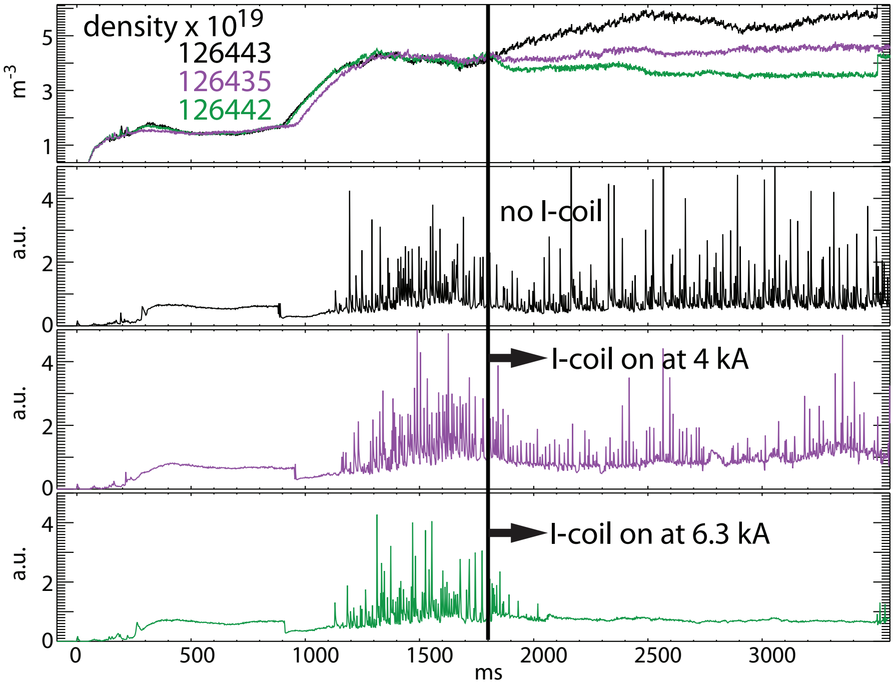

Figure 5.4: Time evolution of three ISS discharges. One reference discharge, 126443, and two RMP discharges, 126435 and 126442. From top to bottom: line averaged density, D_α for a discharge with no I-coil (126443), 4 kA (126435) and 6.3 kA (125443).

density drops over the whole core region and that the pedestal gradient changes.

5.3 Modeling

In this section, we model the background transport for and ELMing H-mode and then add the convective particle transport along the magnetic field for the RMP H-modes and compare the results to experimental RMP density profiles. First we derive the effective radial transport coefficients for the ELMing H-modes by matching midplane experimental data with the modeled SOLPS5 results. Next, we find the increase in particle transport due to topological changes in the magnetic field with TRIP3D. This enhanced particle transport is the result of increased convective transport along newly opened magnetic field lines. This transport is expressed as a radial diffusion coefficient and then added to the effective transport

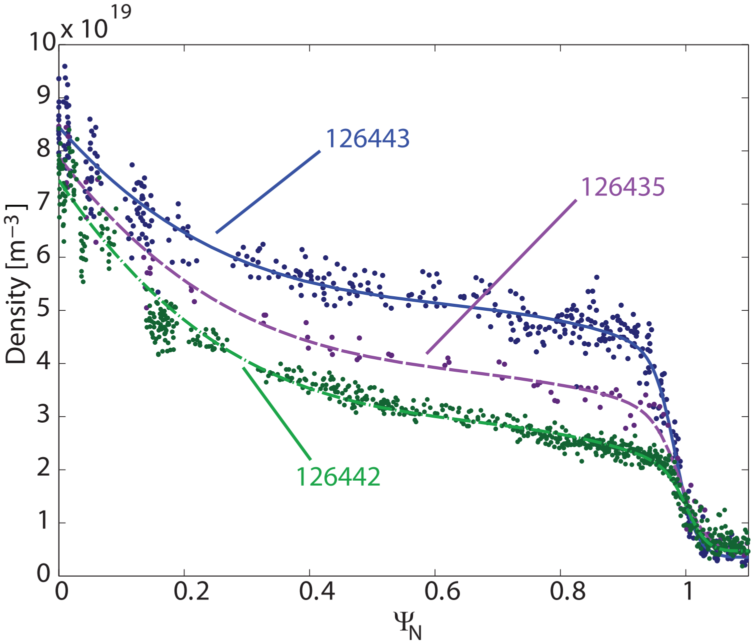

Figure 5.5: Experimental midplane electron density profile in ISS discharges. The points are from the Thomson scattering diagnostic and the curves are the *tanh* fits to the data. Discharge 126443 is the reference ELMing H-mode, discharges 126435 (4 kA) and 126443 (6.3 kA) are RMP H-modes.

coefficients found for the ELMing H-modes. Using the combined radial particle transport coefficients, SOLPS5 calculates the new pedestal density profiles. These are compared to the experimental data.

5.3.1 Effective transport for ELMing H-mode

In this section we compute the radial effective transport (D_{eff}) coefficients to match the midplane density profiles for the ELMing H-modes. To find these coefficients we employ a 2D fluid code, B2, coupled to a Monte Carlo neutral code, EIRENE, combined in the SOLPS5 package. The technique applied to estimate these effective coefficients and initial results for the low triangularity cases can be found in chapter 2. The same technique and setup is then applied to the high triangularity ELMing H-mode. Figure 5.6a shows the obtained density profiles versus the experimental data. The effective radial transport coefficients (D_{eff})

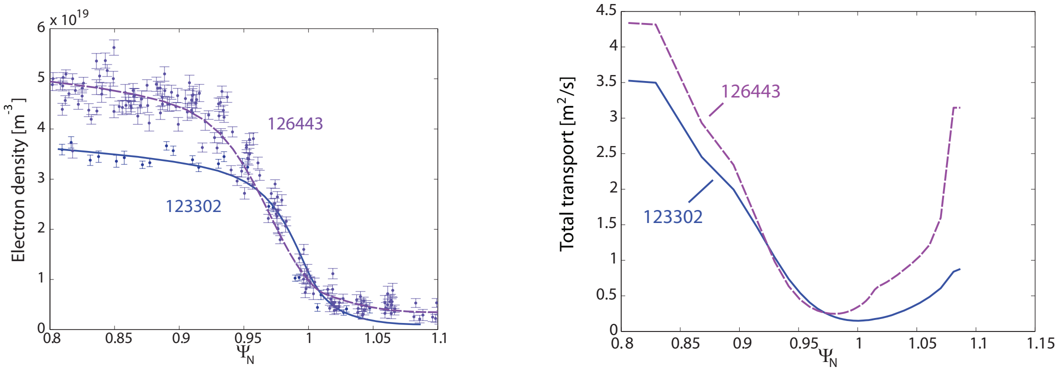

(a) Experimental midplane electron density profile Thomson scattering data with resulting SOLPS5 fit.

(b) Resulting D_{eff} from SOLPS5 computation to fit the experimental density midplane profile.

Figure 5.6: SOLPS5 modeling of experimental ELMing H-mode profiles results in an effective radial diffusion coefficient.

required to obtain these profiles, are shown in figure 5.6b. Note that these transport profiles represent the total radial transport as a diffusion coefficient. However this does not imply that all the transport in the pedestal is purely diffusive.

5.3.2 Enhanced transport due to 3D magnetic topology

TRIP3D [100] is a vacuum magnetic field line tracing code which starts from a reconstructed magnetic equilibrium using the EFIT code. EFIT is a Grad-Shafranov equation solver that gives a 2D axisymmetric equilibrium reconstruction constrained by experimental data. We superimposed on this equilibrium, the magnetic fields created by the different coils and known field-errors. These magnetic fields are calculated using Biot-Savart for existing coils currents and artificial currents to mimic field-errors. To trace field lines, we calculated B-fields at the starting point and subsequently use a fourth order Runge-Kutta integrator to spatially step to the next point on a field line.

To calculate the change in convective particle transport parallel to the magnetic field, we need a dense grid of field lines to average out the extreme effects of X-point and O-points of the created island chains. Therefore, 180 equidistant poloidally distributed field lines on 40 axisymmetric surfaces for $\Psi_N = 0.8 - 1$

are needed to calculate the magnetic topology. We follow each field line for 200 toroidal turns or until it hits the boundary of the vessel, resulting in a very dense grid of points.

Next, for each surface we calculate the transport based on convective particle transport parallel to the magnetic field using the following equation from [100]:

$$D_M = \frac{1}{N}\sum_{i=1}^{N}\frac{(\Delta r_i)^2}{2L_i}[m]. \tag{5.1}$$

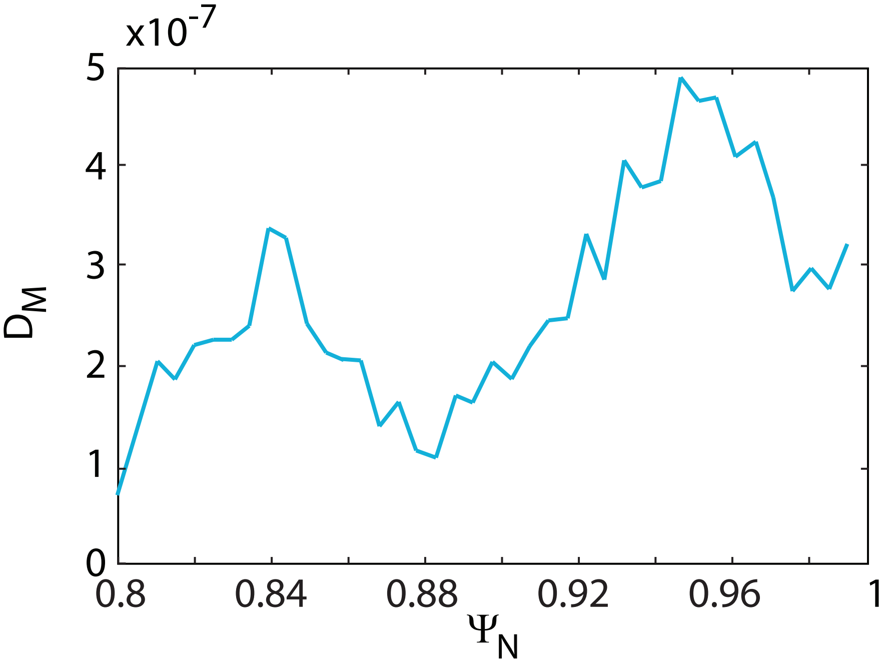

Figure 5.7: Illustration of resulting magnetic diffusion coefficient (D_M with units [m]) profile for low triangularity RMP discharge.

We calculate Δr_i based upon the difference in Ψ_N from the starting point of the field line to the end point. We map these differences in Ψ_N back to values in real space at the midplane, as opposed to using a geometric factor as in [100]. Mapping the Ψ_N at the midplane versus mapping them close to the X-point leads to different results due to flux expansion yielding in an overestimation of the enhanced transport. L_i is the length of each field line and the sum is over all the field lines started on one axisymmetric surface, in this case where $N = 180$ poloidally distributed points. Figure 5.7 plots the resulting curve after application of equation 5.1 to all 40 surfaces.

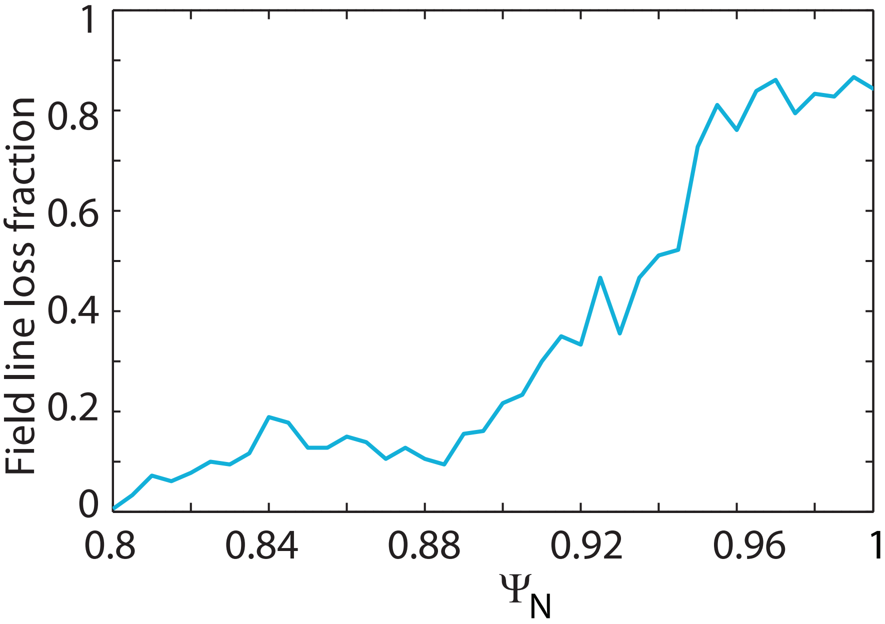

Figure 5.8: Illustration of resulting field line loss fraction profile for low triangularity RMP discharge.

This formula overestimates the influence of field lines that do not leave the plasma. Since particle convection parallel to the magnetic field is dominated by field lines that leave the plasma, we multiply D_M with the field line loss fraction (figure 5.8), which distinguishes between the open field lines for which convection parallel to the magnetic field line actually leads to a density pump-out and the closed perturbed field lines that improve the mixing of field lines, without changing the particle inventory. Finally the weighted D_M is multiplied with the sound speed of the plasma (defined as $c_s = sqrt(T_e/m_i)$), resulting in an artificial radial diffusion coefficient with units m^2/s. This coefficient is used in the 2D axisymmetric fluid code, to mimic the behavior of the 3D topology for particle transport. The difference in the artificial radial diffusion coefficient between the RMP H-mode and the ELMing H-mode is added to the effective transport coefficients obtained from reproducing the upstream density profiles in the ELMing H-mode.

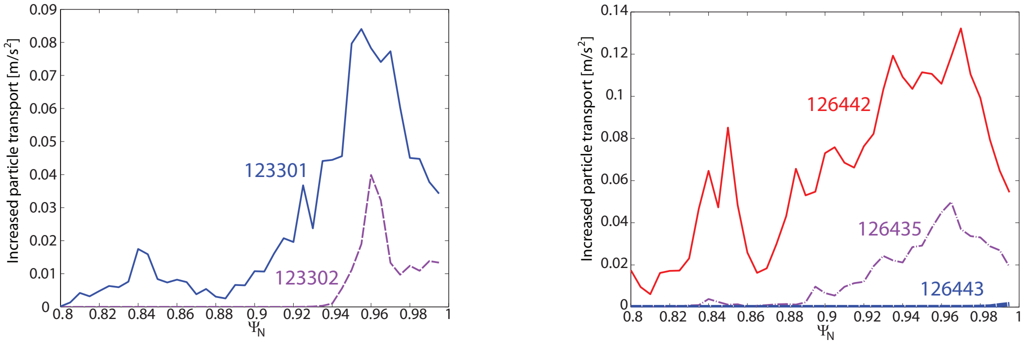

(a) Weighted D_M profile for the low triangularity discharges.

(b) Weighted D_M profile for the ISS discharges.

Figure 5.9: Vacuum predictions of the increase in transport as a result of increased particle convection parallel to the magnetic field .

Figures 5.9a and 5.9b show the calculated radial diffusion coefficients based on the principle of convective particle transport parallel to the magnetic field. The curve for discharge 133302 in figure 5.9a (the low triangularity ELMing H-mode) shows a substantial D_M based on error field correction coils and error fields. The addition of the even parity $n = 3$, 60 degree phasing of the I-coil, increases the transport further as seen for discharge 123301. The curve for discharge 126443 in figure 5.9b (an ELMing H-mode at high triangularity) shows no substantial transport based on the stochastic radial diffusion coefficient. When adding the I-coil perturbation at 4 kA for discharge 126435, we see a substantial increase in the stochastic radial diffusion coefficient (figure 5.9b). However the peak value for discharge 126435 is still lower than the peak value obtained for discharge 123301. Finally, further increasing the current in the I-coils (6.3 kA) results in discharge 126442, which has a higher peak value at the edge than the suppressed discharge for low collisionality (figure 5.9). A secondary peak appears deeper in the core and is separated from the main peak by a valley which correlates with an island chain. This island chain has stochastic X-points acting as channels for field lines to leave the plasma from deeper inside the core.

5.3.3 Predicting RMP H-mode densities with SOLPS5

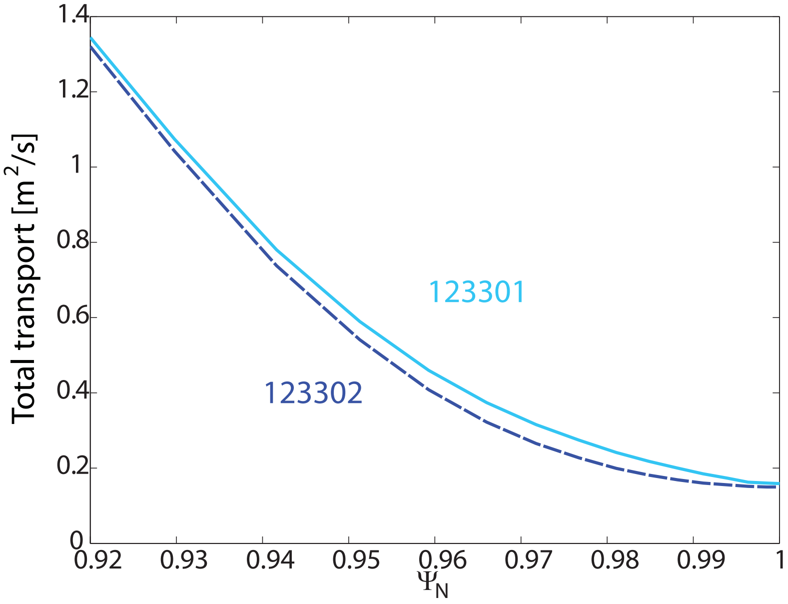

Figure 5.10: Increase in D_{eff} obtained when the particle parallel convection due to the RMP is added to the ELMing H-mode transport model for the reference discharge (123302).

In order to model the RMP H-modes, we start from the effective radial transport coefficients obtained from matching the ELMing H-modes. Next, we add the difference in enhanced particle transport from the RMP H-mode versus the ELMing H-mode, based on the altered magnetic topology from the previous section, to calculate the new total radial transport $[= D_{eff} + (D_{M_{RMP}} - D_{M_{ELM}})]$. The core boundary conditions (fixed density and temperatures) are changed to match the experimentally observed values for the RMP H-modes. The neutrals are treated self-consistently by the EIRENE part in the code package and are determined by recycling coefficients and the pumping at the pump-entrance. As in chapter 2, the recycling is set to 1 at all the walls, except for the divertor target plates, where 0.97 is chosen. Both experiments have active cryopumping and the pumping efficiency is set to 30%. The increased transport, for the low triangularity case (figure 5.10) mostly affects the area of the transport barrier (figure 5.11b).

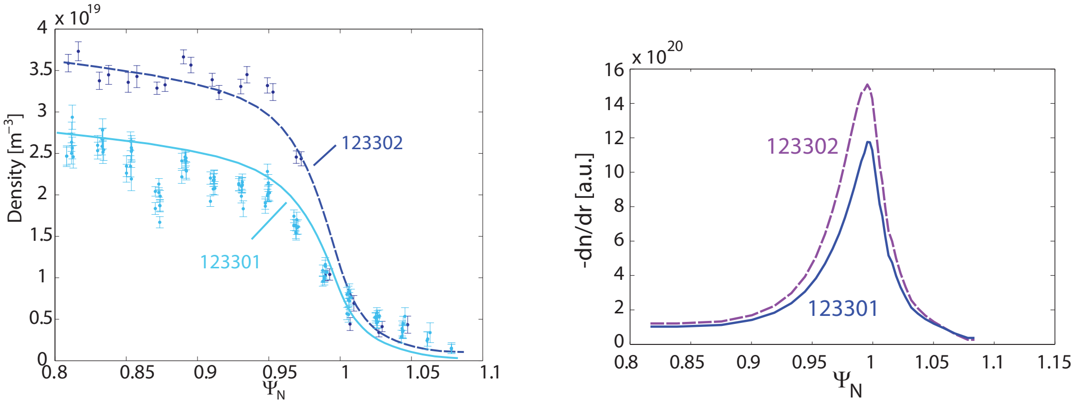

(a) Predicted SOLPS5 density profile as result of increased parallel particle convection when compared to experimental data.

(b) Changes in density profile gradient as a result of increased parallel particle convection.

Figure 5.11: SOLPS5 predicted density profiles and gradients as a result of RMPs in low triangularity discharges.

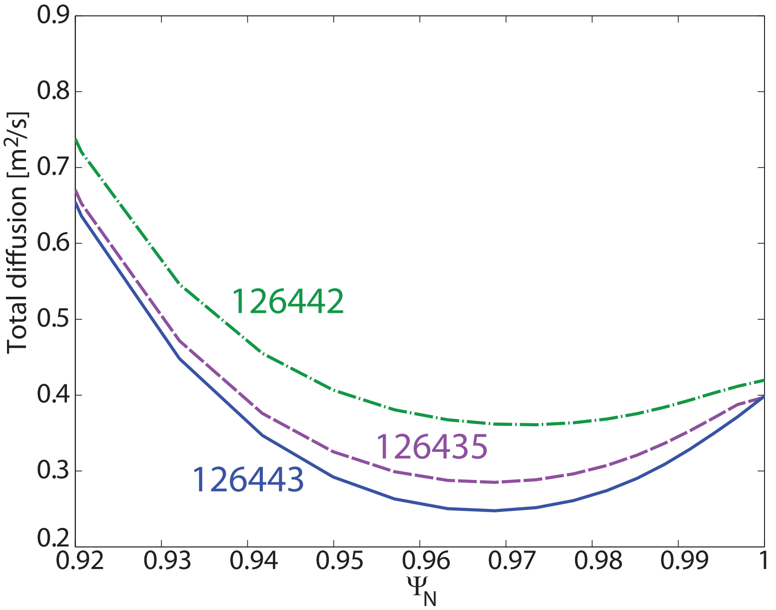

Figure 5.12: Increase in D_{eff} obtained when the particle parallel convection due to the RMP is added to the ELMing H-mode transport model for the reference discharge (126443).

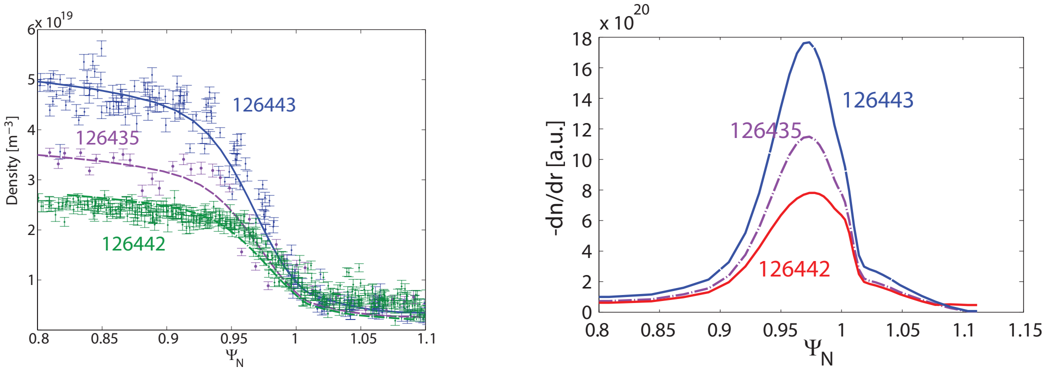

(a) Predicted SOLPS5 density profile as result of convective parallel particle transport when compared to experimental data.

(b) Changes in density profile gradient as a result of convective parallel particle transport.

Figure 5.13: SOLPS5 predicted density profiles and gradients as a result of RMPs in ISS discharges.

This results in an altered midplane density profile, as shown in figure 5.11a, where the SOLPS5 simulation matches the experimental profile for the RMP H-mode. This match is also observed in the high triangularity cases, where the convection parallel to the magnetic field is different from the low triangularity case. Figure 5.13a shows that the enhanced transport from figure 5.12 does not only match the ELM suppressed RMP H-mode, but also the still ELMing RMP H-mode. Again, the largest change in particle transport and, as a result, change in the pedestal density gradient is observed at the steepest part of the pedestal (figure 5.13b). The unperturbed transport coefficients dominate the profile shape and the perturbed coefficients are small in comparison. Chapter 2 shows that only for the steepest part of the pedestal, the change is outside the experimental error-bars. The magnitude and trends in the calculations of the enhanced particle transport are consistent with trends observed in experiments.

5.4 Discussion

The results presented in the previous section indicate that the change in magnetic topology created by the external perturbations from the coils lead to a change in particle transport. The change in particle transport matches the RMP pedestal profiles to within the error bars of the experimental data. This suggests together with the work done on neutral sources in chapter 2, that by controlling the perturbation spectrum, we can control the density pump-out. This would be very beneficial to the operation of ITER. However, it is not yet understood if ELM suppression can be achieved with an altered pattern that leads to less density pump-out. Only the high collisionality experiments ($\nu^* \sim 1$ versus $\nu^* \sim 0.05$), which were performed in the ITER shape (different from the low $< \delta >$ and ISS shapes studied in this work) and with a different I-coil parity, were able to maintain a fixed line averaged density and still achieve ELM suppression [20].

Although there is good agreement between experiments and modeling, our model for the enhanced convection parallel to the magnetic field is not complete. First of all, the model does not include the effects of RMPs to the ambipolar electric field. Including these effects will change the electron thermal heat transport and could limit the particle transport. Next, convection parallel to the magnetic field is based on vacuum calculations. It does not include the plasma response to the applied magnetic perturbation field. There are regions where the field may be screened [89] or amplified [45]. These phenomena can reduce or increase transport in different areas of the plasma. However, we would like to point out that if the magnetic perturbation was fully screened inside of $\Psi_N = 0.9$, this would not alter these results in a significant way, since the additional convective parallel transport is very small due to the lack of open field lines in this area. Moreover, the effective transport coefficients from the ELMing H-mode are already 10 times larger in this region than in the transport barrier region, reducing the impact of added transport. Another possible explanation for the lack of density profile changes in this region of the model, is the influence of the particle source term at the core boundary condition. This effect will be investigated in further modeling. Also, the fraction of trapped particles can change the influence of convection parallel to the magnetic field, since the trapped particles may be turned in the magnetic mirror, retracing on a banana orbit prior to traveling a Kolmogorov length. However, this is mostly dependent on collisionality and since the experiments discussed in this paper have similar collisionalities, it would affect both studied experiments in a similar way. Another aspect of neoclassical transport that is not included in this simple model is the change in perpendicular transport due to collisions.

Additional to different transport mechanism and the effect of plasma response to the RMPs, which are not included in our model, plasma wall interactions are also altered. Chapter 2 shows that some of these effects, like increased pumping and changes in recycling, lead to a density pump-out, but not to a sufficient change in the pedestal shape. So a change in the neutral source does not affect the pedestal profiles enough to obtain a complete agreement with experimental data. Also, experimental data shows that RMPs decrease the amount of impurities in the core plasma and alters the radiation [81].

Another apparent paradox is the difference between the particle flux and the heat flux. Two different 3D fluid codes show that the calculated heat flux is inconsistent with experimental observations [42, 28]. However, [28] shows that the increased particle flux as a result of the RMP and the footprint pattern are in good agreement. Previous work on parallel heat fluxes in the scrape-off layer (SOL) shows that the Spitzer-Harm conductivity, as employed in plasma edge fluid codes, overestimates the parallel heat transport [29]. The deviation from Spitzer-Harm increases with lower collisionality. 2D fluid codes, like SOLPS5, have ad-hoc flux limitations to limit the parallel heat flux, however this is still under development in the 3D fluid codes. Tokar et al. [84] and Schmitz et al. [70] show that a 1D sheath-limited heat flux regime approximation is not in disagreement with an increase in particle flux as a result of free-streaming in low collisionality plasmas. A recent publication by Jakubowski et al. [38] illustrates that the parallel heat flux behaves differently in high collisionality RMP plasmas (i.e. footprint pattern visible in the heat flux), versus low collisionality (i.e. no visible footprint pattern in the heat flux). In this thesis, we refrain from increasing the electron heat conductivity; however, there is an increase in convective heat transport as a result of the increase in particle transport. This is still an active and complicated research topic in SOL physics and the influence of RMPs is not well understood.

Finally, the SOLPS5 code is a 2D axisymmetric fluid code. It does not have the full 3D topology created by the RMPs and does not include kinetic effects. Therefore, these results should be interpreted as a first indication that the pedestal shape changes are related to the changes in magnetic topology and the creation of open magnetic field lines inside the axisymmetric separatrix for DIII-D low collisionality H-mode discharges.

5.5 Conclusion

In this chapter, we discuss the relation between the changes in pedestal density characteristics and changes in radial particle transport due to convection parallel to the magnetic field by RMPs in low collisionality DIII-D H-modes. We find that in low collisionality, for two different plasma shapes, the theoretical calculated changes in particle transport correspond well to the changes observed in pedestal density shapes, modeled with a 2D fluid code. The transport changes calculated by the enhanced particle convection parallel to the magnetic field correspond well to transport changes required in chapter 2 and [18, 53] to match RMP H-modes experiments in the pedestal region. Furthermore, the transport calculations are more detailed than those in [18], which did not allow for varying radial transport coefficients inside the separatrix and include more plasma shapes than those in chapter 2.

Chapter 4 shows that turbulent transport increases in MAST and in the core of DIII-D H-mode discharges. However, in the pedestal area of DIII-D low collisionality H-mode plasmas, where turbulence doesn't appear to be correlated with the increased pedestal transport, calculated vacuum convective particle transport parallel to the magnetic field is in good agreement with experiments density profiles.

Chapter 6

Conclusions

In this final chapter we summarize the work discussed in this thesis and summarize the original contributions. Finally, we conclude this thesis with some directions for future research on the effects of RMPs on particle transport.

6.1 Summary

This thesis contributes to the work on increased particle transport resulting from resonant magnetic perturbations (RMPs). These resonant magnetic perturbations are choosen to be resonant with the edge of the plasma; by choosing an $n = 3$ spectrum and having a $q_{95} = 3.6$. RMPs lead to a changes in density profile, not only in the pedestal area, but also deeper in the plasma core.

In **chapter 2**, we show that the changes in the pedestal density profile are not solely due to changes in plasma-wall interactions. We show that although changes in recycling and cryo-pumping lead to a different level of neutral fueling and therefore can cause a density pump-out, they do not reproduce the changes in density pedestal shape that are experimentally observed. To reproduce the experimentally observed pedestal density changes, the particle transport has to increase at the steepest part of the density pedestal.

In **chapter 3**, we identify whether the experimentally observed density pump-out correlates with the applied RMPs. We introduce the parameter D_{OFL}, which is the magnetic diffusion coefficient D_M weighted with the field line loss fraction. This parameter includes much more experimental details such as plasma equilibrium (e.g., shape, pressure profile, q-profile, etc.) and RMP details (e.g., RMP strenght, spectrum, non-resonant and resonant components) than previous techniques (e.g.: I-coil current and chirikov overlap coefficient, σ_{chir}). By taking these details into account we can compare different experiments in a similar regime, illustrating that there is a correlation. Moreover, it introduces the possibility of machine comparisons. In this thesis we compare low collisionality DIII-D H-mode experiments with MAST L-modes. We find that there is significant difference between both machines and in the following chapter we start to investigate this difference.

Chapter 4 discusses experimental measurements of changes turbulent transport as a result of RMPs for DIII-D H-mode plasmas and MAST L-modes. We find that althought the drive terms for turbulence are not altered in an significant way for MAST, fluctuations increase and the $E \times B$ shear at the plasma edge decreases. Both measurements indicate that anomalous transport increases for MAST L-modes at the plasma edge. In DIII-D H-mode discharges, the drive terms vary depending on radial location and type. There is a positive correlation between the changes in the invariant scale length a/L_n and changes in long wavelength fluctuation measurements, measured by the Beam Emission Spectroscopy (BES) diagnostic. From $\Psi = 0.7 - 0.9$, the $E \times B$ shear decreases, independently of the magnitude of the $n = 3$ applied I-coil current. For the pedestal area, the changes in $E \times B$ are highly dependent on the profile fits and as a result no clear trend is observed. Fluctuation measurements increase in the core, but actually decrease in the pedestal region. As a result, characteristics of turbulent particle transport show an increase in the core and a decrease in the pedestal area. This illustrates, that density pump-out from RMPs can have multiple causes, depending on experimental plasma conditions.

Finally, in **chapter 5** we show that in low collisionality H-mode discharges, an approximation for particle convection parallel to the magnetic field, based on a vacuum calculation agrees well with experimental changes in pedestal density profiles. To make predictions on pedestal density profiles with RMPs, SOLPS5, a

2D fluid code, first deduces the effective radial particle transport for a reference ELMing H-mode. Next, the weighted magnetic diffusion coefficient multiplied with the sound speed, c_s is added to this effective transport coefficient, to predict RMP pedestal density profiles. Good agreement with experimental profiles is found for multiple discharges with different plasma shapes.

6.2 Original contributions

In this section we review my original contributions of this work organized per chapter.

Chapter 2. This chapter explores the effects of altered wall conditions on H-mode discharges in DIII-D. It demonstrates how reduced fueling can lead to a density pump-out and the limitations of altered neutral fueling on the pedestal shape. This chapter concludes that experimental observed density changes from RMPs are the result of increased particle transport. This work as published in [53].

Chapter 3 In this chapter we introduce the correlation coefficient, D_{OFL}, based on a weighted magnetic diffusion coefficient. We show, that D_{OFL} correlates with the experimentally observed density pump-out in DIII-D low collisionality H-modes and MAST L-mode discharges. However, we show that the magnitude of the density pump-out and the slope of the correlation are vastly different for both machines. This correlation presented in this chapter is in review [54].

Chapter 4 This chapter looks in more detail at the differences in turbulent transport for RMP discharges in DIII-D and MAST. We find that in the pedestal are for DIII-D H-mode discharges, the fluctuation levels decrease. Part of this work is in review [54].

Chapter 5 In this chapter, convective parallel particle transport resulting from RMPs is investigated as a possible explanation for the changes in density pedestal. We find good agreement for multiple discharges, using a vacuum 2D representation of free streaming transport in a 2D fluid code. This work is published in [55].

6.3 Directions for future research

Although, in recent years together with contributions in this thesis a large body of work on changes in particle transport as a result of RMPs (see Chapter 3) has emerged, there are still many challenges ahead.

Influence of rotation The work presented in this thesis only includes a vacuum representation of the perturbative magnetic field. Previous work performed on error field penetration and locked modes, shows that the toroidal plasma rotation screens the externally applied RMPs [27], making a high rotating plasma less prone to error field penetration. The DIII-D plasmas in this thesis are all fast co-rotating plasmas and it is therefore a logical extension of this work to include rotational screening as an extension of the vacuum representation of RMPs and to investigate how this would affect the free streaming transport.

Not only can the rotational screening mask the effect of the RMPs, perturbative magnetic fields (e.g. error fields) have shown to brake the plasma rotation [65]. This braking has a resonant component and a non-resonant component, that both reduce the plasma rotation. Reduction in the plasma rotation lowers the $E \times B$ shear and als changes the fluctuation levels. So the braking of rotation by RMPs can lead to indirect changes in turbulent particle transport.

Ideal MHD effects Recent work comparing the plasma response of $n = 1$ externally applied perturbative magnetic fields to ideal MHD calculations shows a very good agreement and a large amplification of the applied field [45]. This amplification is the result of the external magnetic field being enhanced by an internal kink mode. How an amplification or reduction of the applied $n = 3$ RMP affects the transport as a result of free streaming would be a logical extension of this work.

Neo-classical transport Modeling by XGC0 shows that the density pump-out is caused by a change in neo-classical transport of the ions [63]. However, to be able to mimic the observed changes in the first 4ms of the turn of the I-coils, an ad-hoc screening model is employed. The screening is the strongest in the region where the vacuum model predicts a large amount of open field lines with short connection lengths. One of the limitations XGC0 is the assumption that the potential on a flux surface is constant, which is violated in the SOL region (or any region of open field lines). The sheath at the target plates repels electrons, which can result in a similar effect as the employed ad-hoc screening coefficient.

Turbulent transport One of the limitations noted in the conclusions on turbulent transport (chapter 4) in this thesis is the lack of potential fluctuations with the reciprocating probe. To calculate the direct particle flux resulting from turbulence, probe measurements of the potential fluctuations, together with the density fluctuations and the cross-phase between these two [56] are required. In the DIII-D H-mode plasmas discussed in this thesis, it is impossible to plunge a probe inside the separatrix without arcing, therefore it would be benefitial to explore this regime in L-mode discharges and ECH H-mode discharges.

Inward Pinch This thesis only deals with changes in effect transport; it does not seperate out changes to the inward particle pinch V and the diffusive outward particle transport D. Gas modulation experiments can help seperate out the effects on D and V, leading to a better understanding of the influence of RMPs on plasmas. 2D fluid modeling of these discharges can then validate these changes and investigate the influence of increased neutral fueling by the gas puff modulation on the experimental results.

ITER One of the main concerns for ITER is the amount of density pump-out that is needed to obtain ELM suppression. It is therefore crucial to be able to make a correct prediction for the different proposed RMP schemes what the level of density pump-out will be. Therefore, we need to expand the correlation in chapter 3 to include more experimental devices with ITER like conditions.

Bibliography

[1] The ADAS Project. *ADAS Manual 2.6*.

[2] International Atomic Energy Agency. *Issues relating to safety standards on geological disposal of radioactive waste*. International Atomic Energy Agency, 2001.

[3] International Energy Agency. *World Energy Outlook*. International Energy Agency, 2009.

[4] H. Biglari, P.H. Diamond, and P.W. Terry. Influence of sheared poloidal rotation on edge turbulence. *Physics of Fluids B*, 2:1, 1990.

[5] Fatih Birol. *World Energy Outlook*. International Energy Agency, 2008.

[6] S.I. Braginskii. Transport processes in a plasma. *Reviews of Plasma Physics*, 1:205, 1965.

[7] K.H. Burrell. Effects of *exb* velocity shear and magnetic shear on turbulence and transport in magnetic confinement devices. *Physics of Plasmas*, 4:5, 1997.

[8] K.H. Burrell, T.E. Evans, E.J. Doyle, M.E. Fenstermacher, R.J. Groebner, A.W. Leonard, R.A. Moyer, T.H. Osborne, M.J. Schaffer adn P.B. Snyder, P.R. Thomas, W.P West, J.A. Boedo, A.M. Garofalo, P. Gohil, G.L. Jackson, R.J. La Haye, C.J. Lasnier, H. Reimerdes, T.L. Rhodes, J.T. Scoville, W.M. Solomon, D.M. Thomas, G. Wang, J.G. Watkins, and L. Zeng. Elm suppression in low edge collisionality h-mode discharges using n=3 magnetic perturbations. *Plasma Physics and Controlled Fusion*, 47(B37), 2005.

[9] A.J. Cole, C.C. Hegna, and J.D. Callen. Effect of neoclassical toroidal viscosity on error-field penetration thresholds in tokamak plasmas. *Physical Review Letters*, 99:065001, 2007.

[10] J.W. Connor. Edge-localized modes - physics and theory. *Plasma Physics and Controlled Fusion*, 40(531), 1998.

[11] J.A. Crotinger, L. LoDestro, L.D. Pearlstein, A. Tarditi, and T.A. Casper. Corsica: a comprehensive simulation of toroidal magnetic-fusion devices final report to the ldrd program. Technical Report UCRL-ID-126284, Lawrence Livermore National Laboratory, 1997.

[12] P. Devynck, X. Garbet, Ph. Ghendrhi, J. Gunn, C. Honore, B. Pégourié, G. Antar, A. Azeroual, P. Beyer, C. Boucher, V. Budaev, H. Capes, F. Gervais, P. Hennequin, A. Quémeneur, A. Truc, and J.C. Vallet. Edge turbulence during ergodic divertor operation in tore supra. *Nuclear Fusion*, 42:697, 2002.

[13] T.E. Evans. *Chaos, complexity and transport. Theory and Applications*, chapter Implications of topological complexity and hamiltonian chaos in the edge magnetic field of toroidal fusion plasmas. World Scientific, 2008.

[14] T.E. Evans, K.H. Burrell, M.E. Fenstermacher, R.A. Moyer, T.H. Osborne, M.J. Schaffer, W.P West, L.W. Yan, J.A. Boedo, E.J. Doyle, G.L. Jackson, I. Joseph, C.J. Lasnier, A.W. Leonard, T.L. Rhodes, P.R. Thomas, J.G. Watkins, and L. Zeng. The physics of edge resonant magnetic perturbations in hot tokamak plasmas. *Physics of Plasmas*, 13(056121), 2006.

[15] T.E. Evans, M.E. Fenstermacher, R.A. Moyer, T.H. Osborne, J.G. Watkins, P. Gohil, I. Joseph, M.J. Schaffer, L.R. Baylor, M. Bécoulet, J.A. Boedo, K.H. Burrell, J.S. deGrassie, K.H. Finken, T. Jernigan, M.W. Jakubowski, C.J. Lasnier, M. Lehnen, A.W. Leonard, J. Lonroth, E. Nardon, V. Parail, O. Schmitz, B. Unterberg, and W.P. West. Rmp elm suppression in diii-d plasmas with iter similar shapes and collisionalities. *Nuclear Fusion*, 48(024002), 2008.

[16] T.E. Evans, I. Joseph, R.A. Moyer, M.E. Fenstermacher, C.J. Lasnier, and L.W. Yan. Experimental and numerical studies of separatrix splitting and magnetic footprints in diii-d. *Journal of Nuclear Materials*, 363-365:570–574, 2007.

[17] T.E. Evans and R.A. Moyer. Modeling of coupled edge stochastic and core resonant magnetic field effects in diverted tokamaks. *Journal of Nuclear Materials*, 313-316:1282–1286, 2003.

[18] T.E. Evans, R.A. Moyer, K.H. Burrell, M.E. Fenstermacher, I. Joseph, A.W. Leonard, T.H. Osborne, G.D. Porter, M.J. Schaffer, P.B. Snyder, P.R. Thomas, J.G. Watkins, and W.P. West. Edge stability and transport control with resonant magnetic perturbations in collisionless tokamak plasmas. *Nature Physics*, 2:419, 2006.

[19] T.E. Evans, R.A. Moyer, and P. Monat. Modeling of stochastic magnetic flux loss from the edge of a poloidally diverted tokamak. *Physics of Plasmas*, 9:4957, 2002.

[20] T.E. Evans, R.A. Moyer, P.R. Thomas, J.G. Watkins, T.H. Osborne, J.A. Boedo, E.J. Doyle, M.E. Fenstermacher, K.H. Finken, R.J. Groebner, M. Groth, J.H. Harris, R.J. La Haye, C.J. Lasnier, S. Masuzaki, N. Ohyabu, D.G. Pretty, T.L Rhodes, H. Reimerdes, D.L. Rudakov, M.J. Schaffer, G. Wang, and L. Zeng. Suppression of large edge-localized modes in high-confinement diii-d plasmas with a stochastic magnetic boundary. *Physical Review Letters*, 92(235003), 2004.

[21] T.E. Evans, R.A. Moyer, J.G. Watkins, P.R. Thomas, T.H. Osborne, J.A. Boedo, M.E. Fenstermacher, K.H. Finken, R.J. Groebner, M. Groth, J. Harris, G.L. Jackson, R.J. La Haye, C.J. Lasnier, M.J. Schaffer, G. Wang, and L. Zeng. Suppression of large edge loaclized modes in high confinement diii-d plasmas with a stochastic magnetic boundary. *Journal of Nuclear Materials*, 337-339:691–696, 2005.

[22] T.E. Evans, R.K.W. Roeder, J.A. Carter, B.I. Rapoport, M.E. Fenstermacher, and C.J. Lasnier. Experimental signatures of homoclinic tangles in poloidally diverted tokamaks. *Journal of Physics: Conference Series*, 7:174, 2005.

[23] G. Federici, A. Loarte, and G. Strohmayer. Assessment of erosion of the iter divertor targets during type i elms. *Plasma Physics and Controlled Fusion*, 45(1523), 2003.

[24] M.E. Fenstermacher, T.E. Evans, T.H. Osborne, M.J. Schaffer, M.P Aldan, J.S. deGrassie, P. Gohil, I. Joseph, R.A. Moyer, P.B. Snyder, R.J. Groebner, M. Jakubowski, A.W. Leonard, and O. Schmitz. Effect of island overlap on edge localized mode suppression by resonant magnetic perturbations in diii-d. *Physics of Plasmas*, 15(056122), 2008.

[25] M.E. Fenstermacher, T.E. Evans, T.H. Osborne, M.J. Schaffer, J.S. deGrassie, P. Gohil, R.A. Moyer, and the DIII-D team. Suppresion of type-i elms using single toroidal row of magnetic field perturbation coils in diii-d. *Nuclear Fusion*, 48(122001), 2008.

[26] Trevor Findlay. *The future of nuclear energy to 2030 and its implications for safety, security and nonproliferation.* Centre for International Governance Innovation, 201.

[27] R. Fitzpatrick and T.C. Hender. The interaction of resonant magnetic perturbations with rotating plasmas. *Physics of fluids B*, 3:644, 1991.

[28] H. Frerichs, D. Reiter, O. Schmitz, T.E. Evans, and Y. Feng. Three-dimensional edge transport simulations for diii-d plasmas with resonant magnetic perturbations. *Nuclear Fusion*, 50(034004), 2010.

[29] W. Fundamenski. Parallel heat flux limits in the tokamak scrape-off layer. *Plasma Physics and Controlled Fusion*, 47:R163–R208, 2005.

[30] A.M. Garofalo, G.L. Jackson, R.J. La Haye, M. Okabayashi, H. Reimerdes, E.J. Strait, J.R. Ferron, R.J. Groebner, Y. In, M.J. Lanctot, G. Matsunaga, G.A. Navratil, W.M. Solomon, H. Takahashi, M. Takechi, A.D. Turnbull, and the DIII-D Team. Stability and control of resistive wall modes in high beta, low rotation diii-d plasmas. *Nuclear Fusion*, 47:1121–1130, 2007.

[31] P.H. Ghendrih, A. Grosman, and H. Capes. Theoretical and experimental investigations of stochastic boundaries in tokamaks. *Plasma Physics and Controlled Fusion*, 38:1653–1724, 1996.

[32] B. Gulejová, R.A. Pitts, M. Wischmeier, R. Behn, D. Coster, J. Horacek, and J. Marki. Solps5 modelling of the type iii elming h-mode on tcv. *Journal of Nuclear Materials*, 363-365:1037–1043, 2007.

[33] T. Hamacher and A.M. Bradshaw. Fusion as a future power source: recent achievements and prospects. In *18th congress*. World Energy Council, 2001.

[34] M. King Hubbert. Nuclear energy and fossil fuels. *Drilling and Production Practices, American Petroleum Institute and Shell Development Co.*, (95), 1956.

[35] G.T.A. Huysmans. Elms: Mhd instabilities at the transport barrier. *Plasma Physics and Controlled Fusion*, 47(B165), 2005.

[36] V.A. Izzo and I. Joseph. Rmp enhanced transport and rotational screening in simulations of diii-d plasmas. *Nuclear Fusion*, 48:115004, 2008.

[37] M.W. Jakubowski, S.S. Abdullaev, K.H. Finken, M. Lehnen, and the TEXTOR team. Heat deposition patterns on the target plates of the dynamic ergodic divertor. *Journal of Nuclear Materials*, 337-339:176–180, 2005.

[38] M.W. Jakubowski, T.E. Evans, M.E. Fenstermacher, M. Groth, C.J. Lasnier, A.W. Leonard, O. Schmitz, J.G. Watkins, T. Eich, W. Fundamenski, R.A. Moyer, R.C. Wolf, L.B. Baylor, J.A. Boedo, K.H. Burrell, H. Frerichs, J.S. deGrassie, P. Gohil, I. Joseph, S. Mordijck, M. Lehnen, C.C. Petty, R.I. Pinsker, D. Reiter, T.L. Rhodes, U. Samm, M.J. Schaffer, P.B Snyder, H. Stoschus, T. Osborne, B. Unterberg, E. Unterberg, and W.P West. Overview of the results on divertor heat loads in rmp controlled h-mode plasmas on diii-d. *Nuclear Fusion*, 29(095013), 2009.

[39] M.W. Jakubowski, M. Lehnen, K.H. Finken, O. Schmitz, S.S. Abdullaev, B. Unterberg, R.C. Wolf, and the TEXTOR team. Influence of the dynamic ergodic divertor on the heat deposition pattern in textor at different collisionalities. *Plasma Physics and Controlled Fusion*, 49:S109–S121, 2007.

[40] M.W. Jakubowski, O. Schmitz, S.S. Abdullaev, S. Brezinsek, K.H. Finken, A. Kramer-Flecken, M. Lehnen, U. Samm, K.H. Spatschek, B. Unterberg, R.C. Wolf, and TEXTOR Team. Change of the magnetic-field topology by an ergodic divertor and the effect on the plasma structure and transport. *Physical Review Letters*, 96:035004, 2006.

[41] I. Joseph, T.E. Evans, A.M. Runov, M.E. Fenstermacher, M. Groth, S.V. Kasilov, C.J. Lasnier, R.A. Moyer, G.D. Porter, M.J. Schaffer, R. Schneider, and J.G. Watkins. Calculation of stochastic thermal transport due to resonant magnetic perturbations in diii-d. *Nuclear Fusion*, 48(045009), 2008.

[42] I. Joseph, R.A. Moyer, T.E. Evans, M.J. Schaffer, A.M. Runov, R. Schneider, S.V. Kasilov, M. Groth, and M.E. Fenstermacher. Stochastic transport modeling of resonant magnetic perturbations in diii-d. *Journal of Nuclear Materials*, 363-365:591–595, 2007.

[43] A. Kirk, E. Nardon, R. Akers, M. Bécoulet, G. De Temmerman, B. Dudson, B. Hnat, Y.Q. Liu, R. Martin, P. Tamain, D. Taylor, and the MAST team. Resonant magnetic perturbation experiments on mast using external and internal coils for elm control. *Nuclear Fusion*, 50:034008, 2010.

[44] M. Kobayashi, Y. Feng, S. Masuzaki, M. Shoji, J. Miyazawa, T. Morisaki, N. Ohyabu, N. Ashikawa A. Komori, O. Motojima, Y. Igitkhanov The LHD Experimental Group, F. Sardei, and D. Reiter. Divertor transport study in the large helical device. *Journal of Nuclear Materials*, 363-365:294–300, 2007.

[45] M.J. Lanctot, H. Reimerdes, A.M. Garofalo, M.S. Chu, Y.Q. Liu, E.J. Strait, G.L. Jackson, R.J. La Haye, M. Okabayashi, T.H. Osborne, and M.J. Schaffer. Validation of the linear ideal magnetohydrodynamic model of three dimensional tokamak equilibria. *Physics of Plasmas*, 17:030701, 2010.

[46] P.T. Lang, B. Alper, R. Buttery, K. Gal, J. Hobirk, J. Neuhauser, M. Stamp, and JET-EFDA contributors. Elm triggering by local pellet perturbation in type-i elmy h-mode plasma at jet. *Nuclear Fusion*, 47:754–761, 2007.

[47] P.T. Lang, G.D. Conway, T. Eich, L. Fattorini, O. Gruber, S. G´unter, L.D. Horton, S. Kalvin, A. Kallenbach, M. Kaufmann, G. Kocsis, A. Lorenz, M.E. Manso, M. Maraschek, V. Mertens, J. Neuhauser, I. Nunes, W. Schneider, W. Suttrop, H. Urano, and the ASDEX Upgrade Team. Elm pace making and mitigation by pellet injection in asdex upgrade. *Nuclear Fusion*, 44:665–677, 2004.

[48] B. Lipschultz, B. LaBombard, E.S. Marmar, M.M. Pickrell, J.L. Terry, R. Watterson, and S.M. Wolfe. Marfe: An edge plasma phenomenon. *Nuclear Fusion*, 24:977, 1984.

[49] A. Loarte. Effects of divertor geometry on tokamak plasmas. *Plasma Physics and Controlled Fusion*, 43:R183, 2001.

[50] A. Loarte, G. Saibene, R. Sartori, D. Campbell, M. Becoulet, L. Horton, T. Eich, A. Herrmann, G. Matthews, M. Asakura, A. Chankin, A. Leonard, G. Porter, G. Federici, G. Janeschitz, M. Shimada, and M. Sugihara. Characteristics of type i elm energy and particle losses in existing devices and their extrapolation to iter. *Plasma Physics and Controlled Fusion*, 45(1549), 2003.

[51] G.R. McKee, R.J. Fonck, D.K. Gupta, D.J. Schlossberg, M.W. Shafer, R.L. Boivin, and W. Solomon. Plasma turbulence imaging via beam emission spectroscopy in the core of the diii-d tokamak. *Plasma and Fusion Research*, 2:S1025, 2007.

[52] H. Meyer, C. Bunting, P.G. Carolan, M.R. Dunstan, A. Kirk, R. Scannell, D. Temple, M. Walsh, the MAST, and NBI Teams. The structure, evolution and role of the radial edge electric field in h-mode and l-mode on mast. *Journal of Physics: Conference Series*, 194:132028, 2008.

[53] S. Mordijck, R.A. Moyer, T.E. Evans, X. Bonnin, J. Canik, D. Coster, M. Groth, T.H. Osborne, L.W. Owen, T.W. Petrie, D. Reiter, J.G. Watkins, and E.A. Unterberg. Fluid modeling of an elming h-mode and a rmp h-mode. *Journal of Nuclear Materials*, 390-391:299–302, 2009.

[54] S. Mordijck, R.A. Moyer, A. Kirk, P. Tamain, D. Temple, G.R. McKee, and E. Nardon. Comparison of resonant magnetic perturbation induced particle transport changes in diii-d and mast. *Journal of Nuclear Materials*, In review.

[55] S. Mordijck, L.W. Owen, and R.A. Moyer. Increased particle transport due to resonant magnetic perturbations modelled with a vacuum field line tracing code and a 2d fluid code. *Nuclear Fusion*, 50(034006), 2010.

[56] R.A. Moyer, K.H. Burrell, T.N. Carlstrom, S. Coda, R.W. Conn, E.J. Doyle, P. Gohil, R.J. Groebner, J. Kim, R. Lehmer, W.A. Peebles, M. Porkolab, C.L. Rettig, T.L. Rhodes, R.P. Seraydarin, R. Stockdale, D.M. Thomas, G.R. Tynan, and J.G. Watkins. Beyond paradigm: Turbulence, transport, and the origin of the radial electric field in low to high confinement mode transitions in diii-d tokamak. *Physics of Plasmas*, 2:2397, 1995.

[57] R.A. Moyer, K.H. Burrell, T.E. Evans, M.E. Fenstermacher, P. Gohil, I. Joseph, T.H. Osborne, M.J. Schaffer, P.B. Snyder, J.G. Watkins, L.R. Baylor, M. Bécoulet, J.A. Boedo, N.H. Brooks, E.J. Doyle, K.H. Finken, P. Garbet, M. Groth, J. Harris, E.M. Hollmann, G.L. Jackson, M.W. Jakubowski, T.C. Jernigan, S. Kasilov, C.J. Lasnier, A.W. Leonard, M. Lehnen, J. Lonnroth, E. Nardon, V. Parail, G.D. Porter, T.L. Rhodes, D.L. Rudakov,

A. Runov, O. Schmitz, R. Schneider, D.M. Thomas, P. Thomas, G. Wang, W.P West, L. Yan, J.H. Yu, and L. Zeng. Edge localized mode control in diii-d using magnetic perturbation-induced pedestal transport changes. In *Proc. 21st IAEA Fusion Energy Conf. (Chengdu, China, 2006) (Vienna: International Atomic Energy Agency)*, 2006.

[58] R.A. Moyer, T.E. Evans, T.H. Osborne, P.R. Thomas, M. Becoulet, J. Harris, K.-H. Finken, J.A. Boedo, E.J. Doyle, M.E. Fenstermacher, P. Gohil, R.J. Groebner, M. Groth, G.L. Jackson, R.J. La Haye, C.J. Lasnier, A.W. Leonard, G.R. McKee, H. Reimerdes, T.L Rhodes, D.L. Rudakov, M.J. Schaffer, P.B. Snyder, M.R. Wade, G. Wang, J.G. Watkins, W.P. West, and L. Zeng. Edge localized mode control with an edge resonant magnetic perturbation. *Physics of Plasmas*, 12(056119), 2005.

[59] E. Nardon, M. Bécoulet, G. Huysmans, and O. Czarny. Magnetohydrodynamics modelling of h-mode plasma response to external resonant magnetic perturbations. *Physics of Plasmas*, 14:092501, 2007.

[60] Jef Ongena and Guido Van Oost. Energy for future centuries - will fusion be an inexhaustible, safe and clean energy source. Technical report, EFDA, 2001.

[61] Nick A. Owen, Oliver R. Inderwildi, and David A. King. The status of conventional world oil reserves - hype or cause for concern? *Energy Policy*, 38(4743), 2010.

[62] N. Oyama, P. Gohil, L.D. Horton, A.E. Hubbard, J.W. Hughes, Y. Kamada, K. Kamiya, A.W. Leonard, A. Loarte, R. Maingi, G. Saibene, R. Sartori, J.K. Stober, W. Suttrop, H. Urano, W.P. West, and the ITPA Pedestal Topical Group. Pedestal conditions for small elm regimes in tokamaks. *Plasma Physics and Controlled Fusion*, 48:A171–A181, 2006.

[63] G. Park, C.S. Chang, I. Joseph, and R.A. Moyer. Plasma transport in stochastic magnetic field caused by vacuum resonant magnetic perturbations at diverted tokamak edge. *Physics of Plasmas*, 17:1, 2010.

[64] A.B. Rechester and M.N. Rosenbluth. Electron heat transport in a tokamak with destroyed magnetic surfaces. *Physical Review Letters*, 40:38–41, 1978.

[65] H. Reimerdes, A.M. Garofalo, E.J. Strait, R.J. Buttery, M.S. Chu, Y. In, G.L. Jackson, R.J. La Haye, M.J. Lanctot, Y.Q. Liu, M. Okabayashi, J.-K. Park, M.J. Schaffer, and W.M. Solomon. Effect of resonant and non-resonant magnetic braking on error field tolerance in high beta plasmas. *Nuclear Fusion*, 49:11, 2009.

[66] R.K. Pachauri A. Reisinger, editor. *Climate Change 2007: Synthesis Report.* International Panel on Climate Change, 2007.

[67] D. Reiter. Progress in two-dimensional plasma edge modelling. *Journal of Nuclear Materials*, 196-198:80–89, 1992.

[68] V. Rozhansky, E. Kaveeva, P. Molchanov, I. Veselova, S. Voskobynikov, D. Coster, A. Kirk, S. Lisgo, and E. Nardon. Modification of the edge transport barrier by resonant magnetic perturbations. *Nuclear Fusion*, 50:034005, 2010.

[69] V. Rozhansky, P. Molchanov, E. Kaveeva, S. Voskoboynikov, A. Kirk, E. Nardon, D. Coster, and M. Tendler. Modeling of edge plasma of mast in the presence of resonant magnetic perturbations. In *Proc. 23^{st} IAEA Fusion Energy Conf. (Daejon, South Korea, 2010) (Vienna: International Atomic Energy Agency)*, 2010.

[70] O. Schmitz, T.E. Evans, M.E. Fenstermacher, H. Frerichs, M.W. Jakubowski, M.J. Schaffer, A. Wingen, W.P West, N.H. Brooks, K.H. Burrell, J.S. deGrassie, Y. Feng, K.H. Finken, P. Gohil, M. Groth, I. Joseph, C.J. Lasnier, M. Lehnen, A.W. Leonard, S. Mordijck, R.A. Moyer, A. Nicolai, T.H. Osborne, D. Reiter, U. Samm, K.H. Spatschek, H. Stoschus, B. Unterberg, E.A. Unterberg J.G. Watkins, R. Wolf, the DIII-D, and TEXTOR Teams. Aspects of three dimensional transport for elm control experiments in iter-similar shape plasmas at low collisionality in diii-d. *Plasma Physics and Controlled Fusion*, 50(124029), 2008.

[71] O. Schmitz, M.W. Jakubowski, H. Frerichs, D. Harting, M. Lehnen, B. Unterberg, S.S. Abduallaev, S. Brezinsek, I. Classen, T. Evans, Y. Feng, K.H. Finken, M. Kantor, D. Riter, U. Samm, B. Schweer, G. Sergienko, G.W. Spakman, M. Tokar, E. Uzgel, R.C. Wolf, and the TEXTOR Team. Identification and analysis of transport domains in the stochastic boundary of textor-ded for different mode spectra. *Nuclear Fusion*, 48:024009, 2008.

[72] R. Schneider, X. Bonnin, K. Borrass, D.P. Coster, H. Kastelewicz, D. Reiter, V.A. Rozhansky, and B.J. Braams. Plasma edge physics with b2-eirene. *Contributions to plasma physics*, 46:3–191, 2006.

[73] M. Shimada, D.J. Campbell, V. Mukhovatov, M. Fuijwara, N. Kirneva, K. Lackner, M. Nagami, V.D. Pustovitov, N. Uckan, J. Wesley, N. Asakura, A.E. Costley, A.J.H. Donné, E.J. Doyle, A. Fasoli, C. Gormezano, Y. Gribov, O. Gruber, T.C. Hender, W. Houlberg, S. Ide, Y. Kamada, A. Leonard, B. Lipschultz, A. Loarte, K. Miyamoto, V. Mukhovatov, T.H. Osborne, A. Polevoi, and A.C.C. Sips. Chapter 1: Overview and summary. *Nuclear Fusion*, 47(S1), 2007.

[74] P.B. Snyder, K.H. Burrell, H.R. Wilson, M.S. Chu, M.E. Fenstermacher, A.W. Leonard, R.A. Moyer, T.H. Osborne, M. Umansky, and W.P West. Stability and dynamics of the edge pedestal in the low collisionality regime: physics mechanisms for steady-state elm-free operation. *Nuclear Fusion*, 47:961–968, 2007.

[75] P.B. Snyder and H.R. Wilson. Ideal magnetohydrodynamic constraints on the pedestal temperature in tokamaks. *Plasma Physics and Controlled Fusion*, 45(1671), 2003.

[76] P.B. Snyder, H.R. Wilson, J.R. Ferron, L.L. Lao, A.W. Leonard, T.H. Osborne, A.D. Turnbull, D. Mossessian, M. Murakami, and X.Q. Xu. Edge localized modes and the pedestal: A model based on coupled peeling-ballooning modes. *Physics of Plasmas*, 9(2037), 2002.

[77] W.M. Solomon, K.H. Burrell, A.M. Garofalo, A.J. Cole, R.V. Budny, J.S. deGrassie, W.W. Heidbrink, G.L. Jackson, M.J. Lanctot, R. Nazikian, H. Reimerdes, E.J. Strait, M.A. Van Zeeland, and the DIII-D Rotation Physics Task Force. Advances in understanding the generation and evolution of the toroidal rotation profile on diii-d. *Nuclear Fusion*, 49:085005, 2009.

[78] W.M. Stacey and T.E. Evans. Investigation of background edge thermal transport in elming and elm-suppressed h-modes in diii-d. *Physics of Plasmas*, 13:112506, 2006.

[79] P.C. Stangeby. *The plasma boundary of magnetic fusion devices*. Taylor and Francis group, 2002.

[80] P. Tamain, A. Kirk, E. Nardon, B. Dudson, B. Hnat, and the MAST team. Edge turbulence and flows in the presence of resonant magnetic perturbations on mast. *Plasma Physics and Controlled Fusion*, 52:075017, 2010.

[81] G. Telesca, E. Delabie, O. Schmitz, S. Brezinsek, K.H. Finken, M. von Hellermann, M. Jakubowski, M. Lehnen, Y. Liang, A. Pospiesczyk, U. Samm, M. Tokar, B. Unterberg, G. Van Oost, and The TEXTOR Team. Carbon transport in the stochastic magnetic boundary of textor. *Journal of Nuclear Materials*, 390-391:227–231, 2009.

[82] P.W. Terry. Suppression of turbulence and transport by sheared flow. *Reviews of Modern Physics*, 72:1, 2000.

[83] M.Z. Tokar, T.E. Evans, A. Gupta, D. Kalupin, A. Nicolai, R. Singh, and B. Unterberg. Modelling of pedestal transport during elm suppression by external magnetic field perturbations. *Nuclear Fusion*, 48(024006), 2008.

[84] M.Z. Tokar, T.E. Evans, A. Gupta, R. Singh P. Kaw, and R.C. Wolf. Mechanisms of edge-localized-mode mitigation by external-magnetic-field perturbations. *Physical Review Letters*, 98(095001), 2007.

[85] M.Z. Tokar, T.E. Evans, R. Singh, and B. Unterberg. Particle transfer in edge transport barrier with stochastic magnetic field. *Physics of Plasmas*, 15(072515), 2008.

[86] E.A. Unterberg, N.H. Brooks, T.E. Evans, M.E. Fenstermacher, D.L. Hillis, R. Maingi, S. Mordijck, R.A. Moyer, T.H. Osborne, T.W. Petrie, and J.G. Watkins. Experimental comparison of recycling and pumping changes during resonant magnetic perturbation experiments at low and high collisionality in diii-d. *Journal of Nuclear Materials*, 390-391:486–489, 2009.

[87] E.A. Unterberg, T.E. Evans, R. Maingi, N.H. Brooks, M.E. Fenstermacher, S. Mordijck, and R.A. Moyer. Demonstration of particle exhaust control during elm suppression by resonant magnetic perturbations in diii-d. *Nuclear Fusion*, 49(092001), 2009.

[88] E.A. Unterberg, O. Schmitz, T.E. Evans, R. Maingi, N.H. Brooks, M.E. Fenstermacher, S. Mordijck, R.A. Moyer, and D.M Orlov. The effects of an open and closed divertor on particle exhaust during edge-localized mode suppression by resonant magnetic perturbations in diii-d. *Nuclear Fusion*, 50(034011), 2010.

[89] F.L. Waelbroeck. Shielding of resonant magnetic perturbations in the long mean-free path regime. *Physics of plasmas*, 10:4040, 2003.

[90] J.G. Watkins, T.E. Evans, M. Jakubowski, R.A. Moyer, O. Schmitz, A. Wingen, M.E. Fenstermacher, I. Joseph, C.J. Lasnier, and D.L. Rudakov. Particle, heat and sheath power transmission factor profiles during elm suppression experiments on diii-d. *Journal Nuclear Materials*, 390-391:839–842, 2009.

[91] John Wesson. *Tokamaks*. Oxford university press, third edition edition, 2004.

[92] A.E. White, , W.A. Peebles, T.L. Rhodes, C.H. Holland, G. Wang, L. Schmitz, T.A. Carter, J.C. Hillesheim, E.J. Doyle, L. Zeng, G.R. McKee, G.M. Staebler, R.E. Waltz, J.C. DeBoo, C.C. Petty, and K.H. Burrell. Measurements of cross-phase angle between density and electron temperature fluctuations and comparison with gyrokinetic simulations. *Physics of Plasmas*, 17:056103, 2020.

[93] A.E. White, L. Schmitz, G.R. McKee, C. Holland, W.A. Peebles, T.A. Carter, M.W. Shafer, M.E. Austin, K.H. Burrell, J. Candy, J.C. DeBoo, E.J. Doyle, M.A. Makowski, R. Prater, T.L. Rhodes, G.M. Staebler, G.R. Tynan,

R.E. Waltz, and G. Wang. Measurements of core electron temperature and density fluctuations in diii-d and comparison to nonlinear gyrokinetic simulations. *Physics of Plasmas*, 15:056116, 2008.

[94] H.R. Wilson, P.B. Snyder, G.T.A. Huysmans, and R.L. Miller. Numerical studies of edge localized instabilities in tokamaks. *Physics of Plasmas*, 9(1277), 2002.

[95] A. Wingen, T.E. Evans, and K.H. Spatschek. Footprint structures due to resonant magnetic perturbations in diii-d. *Physics of Plasmas*, 16(042504), 2009.

[96] A. Wingen, T.E. Evans, and K.H. Spatschek. High resolution numerical studies of separtrix splitting due to non-axisymmetric perturbation in diii-d. *Nuclear Fusion*, 49(055027), 2009.

[97] Y. Xu, M. Van Schoor, R.R. Weynants, S. Jachmich, M. Vergote, M.W. Jakubowski, P. Beyer, M. Mitri, B. Schweer, D. Reiser, B. Unterberg, K.H. Finken, M. Lehnen, R. Jaspers, and the TEXTOR Team. Edge turbulence during static dynamic ergodic divertor experiments in textor. *Nuclear Fusion*, 47:1696, 2007.

[98] Y. Xu, R.R. Weynants, S. Jachmich, M. Van Schoor, M. Vergote, P. Peleman, M.W. Jakubowski, M. Mitri, D. Reiser, B. Unterberg, and K.H. Finken. Influence of the static dynamic ergodic divertor on edge turbulence properties in textor. *Physical Review Letters*, 97:165003, 2006.

[99] Y. Xu, R.R. Weynants, M. Van Schoor, M. Vergote, S. Jachmich, M.W. Jakubowski, M. Mitri, O. Schmitz, B. Unterberg, P. Beyer, D. Reiser, K.H. Finken, M. Lehnen, and the TEXTOR Team. Reduction of turbulent blob transport in the scrape-off layer by a resonant magnetic perturbation in textor. *Nuclear Fusion*, 49:035005, 2009.

[100] L.W. Yan and T.E. Evans. Stochastic boundary modeling by resonant magnetic perturbations on diii-d. *Journal of Nuclear Materials*, 363-365:723–727, 2007.

[101] Z. Yan, G.R. McKee, R.J. Groebner, P.B. Snyder, T.H. Osborne, M.N.A. Beurskens, K.H. Burrell, T.E. Evans, R.A. Moyer, H. Reimerdes, and X. Xu. Pedestal turbulence dynamics in elming and elm-free h-mode plasmas. In *Proc.* 23^{st} *IAEA Fusion Energy Conf. (Daejon, South Korea, 2010) (Vienna: International Atomic Energy Agency)*, 2010.

[102] Y. Yang, G.F. Counsell, and The MAST team. Observations with a midplane reciprocating probe in mast. *Journal of Nuclear Materials*, 313-316:734–737, 2003.

[103] Hartmut Zohm. The physics of edge localized modes (elms) and their role in power and particle exhaust. *Plasma Physics and Controlled Fusion*, 38:1213–1223, 1996.